JETP Letters, Vol. 79, No. 10, 2004, pp. 451–456. From Pis'ma v Zhurnal Éksperimental'noĭ i Teoreticheskoĭ Fiziki, Vol. 79, No. 10, 2004, pp. 563–568.

Neutrino Oscillations from the Splitting of Fermi Points¶

F. R. Klinkhamer

Institut für Theoretische Physik, Universität Karlsruhe (TH), 76128 Karlsruhe, Germany

e-mail: frans.klinkhamer@physik.uni-karlsruhe.de

Received March 30, 2004; in final form, April 20, 2004

As was shown previously, oscillations of massless neutrinos may be due to the splitting of multiply degenerate Fermi points. In this letter, we give the details and propose a three-flavor model of Fermi point splittings and neutrino mixings with only two free parameters. The model may explain recent experimental results from the K2K and KamLAND collaborations. There is also rough agreement with the data on atmospheric neutrinos (SuperK) and solar neutrinos (SNO), but further analysis is required. Most importantly, the Ansatz allows for relatively strong T-violating (CP-nonconserving) effects in the neutrino sector. © *2004 MAIK "Nauka/Interperiodica"*.

PACS numbers: 14.60.Pq; 11.30.Er

1. INTRODUCTION

Neutrino oscillations are commonly associated with neutrino-mass differences (see, e.g., [1–3] for three reviews). But, the different propagation states might also be distinguished by some other characteristic. Two examples discussed in the literature are connected with violations of the equivalence principle [4, 5] and Lorentz invariance [6].

Lorentz noninvariance and CPT violation as emergent phenomena in a fermionic quantum vacuum have been discussed recently by Volovik and the present author [7]. It was noted that one possible consequence of the splitting of multiply degenerate Fermi points (to be defined later) could be neutrino oscillations. The question is whether or not this particular type of neutrino oscillation is compatible with the experimental data. If so, we may have an entirely new perspective on the neutrino sector.

The aim of this paper, then, is to provide an exploratory analysis of the experimental data on neutrino oscillations from the perspective suggested in [7]. In order to stress the difference with mass oscillations, we keep an eye open to the possibility that the experimental data could, after all, be compatible with relatively strong T (and CP?) violation in the neutrino sector.

The outline of this Letter is as follows. In Section 2, we discuss the case of two-flavor oscillations for massless left-handed neutrinos with Fermi point splitting. (A Fermi point is a point in three-momentum space at which the energy spectrum of the fermion considered has a zero.) In Section 3, we propose a simple three-flavor model of Fermi point splittings and neutrino mixings, which allows for strong T violation. The model has two free parameters, an energy scale B_0, and a phase δ, together with particular fixed values (equal or close to $\pi/4$) for the three mixing angles. In Section 4, we give the resulting expressions for the oscillation probabilities among the three flavors. In Section 5, we compare the results of the model with the experimental data on neutrino oscillations. The combined data from K2K and KamLAND (with input from SuperK) appear to favor T violation ($\sin\delta \neq 0$) over time-reversal invariance ($\sin\delta = 0$), but this remains to be confirmed. In Section 6, we present some concluding remarks.

2. TWO-FLAVOR NEUTRINO OSCILLATIONS

In the limit of vanishing Yukawa couplings, the Standard Model fermions are massless Weyl fermions and have the following dispersion law

$$(E_{a,f}(\mathbf{q}))^2 = \left|c\mathbf{q} + \mathbf{b}_a^{(f)}\right|^2, \qquad (1)$$

for three-momentum $\mathbf{q}$ and with $\mathbf{b}_a^{(f)} = 0$ for the moment. Here, a labels the sixteen types of massless left-handed Weyl fermions in the Standard Model (with a hypothetical left-handed antineutrino included) and f distinguishes the three known fermion families.

The Weyl fermions of the original Standard Model have all $\mathbf{b}_a^{(f)}$ vanishing, which makes for a multiply degenerate Fermi point $\mathbf{q} = 0$. (Fermi points (gap nodes) $\mathbf{q}_n$ are points in three-dimensional momentum space at which the energy spectrum $E(\mathbf{q})$ of the fermionic quasiparticle has a zero, i.e., $E(\mathbf{q}_n) = 0$.) Nonzero parameters $\mathbf{b}_a^{(f)}$ in dispersion law (1) describe the splitting of this multiply degenerate Fermi point. See [7] for a discussion of the physics that could be responsible for Fermi point splitting and [6] (and references therein) for a general discussion of Lorentz noninvariance.

¶ This article was submitted by the author in English.

Now, consider the following pattern of spacelike splittings:

$$\mathbf{b}_a^{(f)} = Y_a \mathbf{b}^{(f)}, \text{ for } a = 1, \ldots, 16, \quad f = 1, 2, 3, \quad (2)$$

as given by Eq. (5.4) of [7], with a minor change of notation. Given the hypercharges Y_a of the Standard Model fermions, this pattern has only three unknowns, the vectors $\mathbf{b}^{(f)}$. The Fermi point splittings (2), for nonvanishing $\mathbf{b}^{(f)}$, violate CPT but the induced electromagnetic CPT-odd Chern-Simons-like term cancels out exactly, consistent with the tight experimental limits. Still, there may be other effects, for example, neutrino oscillations (as long as the neutrinos are not affected too much by the mechanism of mass generation).

We therefore focus on massless left-handed neutrinos (hypercharge $Y_{\nu_L} = -1$) with Fermi point splittings (2). The dispersion law for a left-handed neutrino with three-momentum $\mathbf{q}$ is then given by

$$\left(E_{\nu_L, f}(\mathbf{q})\right)^2 = \left|c\mathbf{q} - \mathbf{b}^{(f)}\right|^2, \quad (3)$$

with $f = 1, 2, 3$, for three neutrinos.

In this section, we restrict our attention to oscillations between two flavors of neutrinos (see, e.g., [8] for further details). The mixing angle between the flavor eigenstates $|A\rangle$, $|B\rangle$ and propagation eigenstates $|1\rangle$, $|2\rangle$ will be denoted by θ_{mix}. These propagation states evolve differently as long as $\mathbf{b}^{(1)} \neq \mathbf{b}^{(2)}$ in dispersion law (3).

For an initial neutrino with large enough momentum $|\mathbf{q}|$, the oscillation probability from flavor A to flavor B over a travel time t (travel distance $L \sim ct$) is readily calculated:

$$P(A \longrightarrow B) \sim \sin^2(2\theta_{\text{mix}}) \sin^2\left(\frac{1}{2}\Delta\mathbf{b}^{(ff')} \cdot \hat{\mathbf{q}} L/\hbar c\right), \quad (4)$$

with $\hat{\mathbf{q}} \equiv \mathbf{q}/|\mathbf{q}|$ and $\Delta\mathbf{b}^{(ff')} \equiv \mathbf{b}^{(f)} - \mathbf{b}^{(f')}$, for $f = 1$ and $f' = 2$. Oscillation probability (4) is anisotropic and energy-independent. The survival probability is given by $P(A \longrightarrow A) = 1 - P(A \longrightarrow B)$. Oscillation probabilities similar to Eq. (4) have been discussed, for example, in Section III B of [6].

Next, consider the following timelike splittings of Fermi points for the massless Standard Model fermions:

$$b_{0a}^{(f)} = Y_a b_0^{(f)}, \text{ for } a = 1, \ldots, 16, \quad f = 1, 2, 3, \quad (5)$$

as given by Eq. (6.5) of [7]. Again, the induced electromagnetic CPT-odd Chern-Simons-like term cancels out exactly. The dispersion law of a massless left-handed neutrino is now given by

$$\left(E_{\nu_L, f}(\mathbf{q})\right)^2 = \left(c|\mathbf{q}| - b_0^{(f)}\right)^2, \quad (6)$$

with $f = 1, 2, 3$, for three neutrinos. In order to stay to the usual neutrino phenomenology as close as possible, it is assumed in this paper (different from [7]) that $b_0^{(f)}$ in Eq. (6) is a CP-even parameter. The results of Section 5 are, however, independent of this assumption.

For a large enough momentum of the initial neutrino, there is again an energy-independent two-flavor oscillation probability,

$$P(A \longrightarrow B) \sim \sin^2(2\theta_{\text{mix}}) \sin^2\left(\frac{1}{2}\Delta b_0^{(ff')} L/\hbar c\right), \quad (7)$$

with $\Delta b_0^{(ff')} \equiv b_0^{(f)} - b_0^{(f')}$, for $f = 1$ and $f' = 2$. The first-peak distance (half of the wavelength λ) occurs at

$$L^{\text{first–peak}} = \pi\hbar c/\left|\Delta b_0^{(ff')}\right| \approx 600 \text{ km} \left(\frac{10^{-12} \text{ eV}}{\left|\Delta b_0^{(ff')}\right|}\right). \quad (8)$$

For completeness, we also mention neutrino-mass oscillations [1–3, 8] which are based on the Lorentz-invariant dispersion law

$$\left(E_{\nu, f}(\mathbf{q})\right)^2 = c^2|\mathbf{q}|^2 + m_f^2 c^4 \sim \left(c|\mathbf{q}| + \frac{m_f^2 c^3}{2|\mathbf{q}|}\right)^2, \quad (9)$$

for $|\mathbf{q}| \gg m_f$ and with $f = 1, 2$, for two neutrinos. The standard result,

$$P_{\text{mass–oscill}}(A \longrightarrow B) \sim \sin^2(2\theta_{\text{mix}}) \sin^2\left(\frac{1}{2}\frac{m_f^2 - m_{f'}^2}{2E_\nu} L c^3/\hbar\right), \quad (10)$$

has, of course, the same basic structure as Eq. (7) but is now energy-dependent. With $\Delta m^2 \equiv m_f^2 - m_{f'}^2$, the corresponding first-peak distance is

$$L_{\text{mass–oscill}}^{\text{first–peak}} = \pi(2E_\nu\hbar c)/(\left|\Delta m^2\right|c^4) \approx 600 \text{ km} \left(\frac{E_\nu}{\text{GeV}}\right)\left(\frac{2 \times 10^{-3} \text{ eV}^2/c^4}{\left|\Delta m^2\right|}\right), \quad (11)$$

for energies typical of "atmospheric neutrinos" (see Section 5.1).

3. THREE-FLAVOR SPLITTING AND TRI-MAXIMAL MIXING

For simplicity, we consider only the timelike splittings (5) in the rest of this letter. Because the neutrino oscillations are energy-independent, the analysis of the experimental data is entirely different from that of the usual mass oscillations.

To illustrate this point, we choose the following regular pattern for the Fermi point splittings of the three left-handed neutrinos with dispersion law (6):

$$b_0^{(f)} = fB_0, \text{ for } f = 1, 2, 3. \tag{12}$$

In addition, we take "tri-maximal" values for the mixing angles which enter the unitary matrix V between flavor and propagation states (see Section 4):

$$\begin{aligned} \theta_{13} &= \arctan\sqrt{1/2} \approx \pi/5, \\ \theta_{21} &= \theta_{32} = \arctan 1 = \pi/4. \end{aligned} \tag{13}$$

This neutrino mixing matrix is parametrized as follows [2, 3]:

$$\begin{aligned} V \equiv &\begin{pmatrix} 1 & 0 & 0 \\ 0 & c_{32} & s_{32} \\ 0 & -s_{32} & c_{32} \end{pmatrix} \cdot \begin{pmatrix} c_{13} & 0 & s_{13}e^{-i\delta} \\ 0 & 1 & 0 \\ -s_{13}e^{i\delta} & 0 & c_{13} \end{pmatrix} \\ &\cdot \begin{pmatrix} c_{21} & s_{21} & 0 \\ -s_{21} & c_{21} & 0 \\ 0 & 0 & 1 \end{pmatrix}, \end{aligned} \tag{14}$$

with two Majorana phases set to zero and the standard notation s_x and c_x for $\sin\theta_x$ and $\cos\theta_x$.

The particular values (13) maximize, for given phase δ, the T-violation (CP-nonconservation) measure [9]

$$J \equiv \frac{1}{8}\cos\theta_{13}\sin 2\theta_{13}\sin 2\theta_{21}\sin 2\theta_{32}\sin\delta. \tag{15}$$

This maximality condition on J is used only as a mathematical prescription to select unambiguously certain "large" values of the mixing angles.

At this moment, we do not want to speculate on possible explanations of relations (12) and (13). There is a certain elegance to the model, with essentially two free parameters (B_0 and δ). In contrast, the standard interpretation of the experimental results on neutrino oscillations [2, 3] has three different neutrino masses, at least two different mixing angles, and one undetermined phase:

$$\begin{aligned} m_2^2 - m_1^2 &\approx 7 \times 10^{-5}\ \text{eV}^2/c^4, \\ \left|m_3^2 - m_2^2\right| &\approx 2 \times 10^{-3}\ \text{eV}^2/c^4, \\ \theta_{13} \approx 0, &\quad \theta_{21} \approx \theta_{32} \approx \pi/4, \quad \delta \in [-\pi, \pi]. \end{aligned} \tag{16}$$

These values would imply that T and CP violation in the neutrino sector are suppressed by a small value of the mixing angle θ_{13} [cf. Eq. (15)], which would not be the case for the *Ansatz* (12)–(14).

4. THREE-FLAVOR NEUTRINO OSCILLATIONS

Now, define three flavor states $|A\rangle$, $|B\rangle$, $|C\rangle$ in terms of the propagation states $|1\rangle$, $|2\rangle$, $|3\rangle$, which have dispersion law (6) with parameters $b_0^{(f)}$, $f = 1, 2, 3$, given by pattern (12). In matrix form, the relation is

$$\begin{pmatrix} |A\rangle \\ |B\rangle \\ |C\rangle \end{pmatrix} = V^* \begin{pmatrix} |1\rangle \\ |2\rangle \\ |3\rangle \end{pmatrix}, \tag{17}$$

where the asterisk indicates complex conjugation. Here, we follow the conventions of [2], with the mixing matrix V defined by Eq. (14) for particular values (13).

For a large enough momentum of the initial neutrino, the energy differences from Eq. (12) give the following oscillation probabilities:

$$\begin{aligned} P(A \longrightarrow B) &= (2/9)\sin^2(\Delta/2) \\ &\times (4 + \sqrt{3}c_\delta + (2 + 2\sqrt{3}c_\delta)\cos\Delta - 2\sqrt{3}s_\delta\sin\Delta), \\ P(A \longrightarrow C) &= (2/9)\sin^2(\Delta/2) \\ &\times (4 - \sqrt{3}c_\delta + (2 - 2\sqrt{3}c_\delta)\cos\Delta + 2\sqrt{3}s_\delta\sin\Delta), \\ P(A \longrightarrow A) &= 1 - P(A \longrightarrow B) - P(A \longrightarrow C), \\ P(B \longrightarrow C) &= (2/9)\sin^2(\Delta/2) \\ &\times (13/4 - (3/4)\cos 2\delta + 2\cos\Delta - 2\sqrt{3}s_\delta\sin\Delta), \\ P(B \longrightarrow A) &= (2/9)\sin^2(\Delta/2) \\ &\times (4 + \sqrt{3}c_\delta + (2 + 2\sqrt{3}c_\delta)\cos\Delta + 2\sqrt{3}s_\delta\sin\Delta), \\ P(B \longrightarrow B) &= 1 - P(B \longrightarrow C) - P(B \longrightarrow A), \\ P(C \longrightarrow A) &= (2/9)\sin^2(\Delta/2) \\ &\times (4 - \sqrt{3}c_\delta + (2 - 2\sqrt{3}c_\delta)\cos\Delta - 2\sqrt{3}s_\delta\sin\Delta), \\ P(C \longrightarrow B) &= (2/9)\sin^2(\Delta/2) \\ &\times (13/4 - (3/4)\cos 2\delta + 2\cos\Delta + 2\sqrt{3}s_\delta\sin\Delta), \\ P(C \longrightarrow C) &= 1 - P(C \longrightarrow A) - P(C \longrightarrow B), \end{aligned} \tag{18}$$

with the further definition

$$\Delta \equiv B_0 t/\hbar \sim B_0 L/(\hbar c) \tag{19}$$

and notation s_δ and c_δ for $\sin\delta$ and $\cos\delta$. For the antiparticle probabilities, replace δ by $-\delta$ (assuming B_0 to be CP-even). The difference of the $P(X \longrightarrow Y)$ and $P(Y \longrightarrow X)$ probabilities in Eq. (18), for $X \neq Y$ and $s_\delta\sin\Delta \neq 0$, implies T violation (cf. [3]).

For later use, we also calculate the average probabilities $\langle P\rangle$, defined by integrating Δ over the interval $[0, 2\pi]$ with normalization factor $1/2\pi$:

$$\begin{aligned}(\langle P(A\longrightarrow B)\rangle, \langle P(A\longrightarrow C)\rangle, \langle P(A\longrightarrow A)\rangle)&\\ = (1/3, 1/3, 1/3),&\\ (\langle P(B\longrightarrow C)\rangle, \langle P(B\longrightarrow A)\rangle, \langle P(B\longrightarrow B)\rangle)&\\ = (1/4 - (\cos 2\delta)/12, 1/3, (5 + \cos 2\delta)/12),&\\ (\langle P(C\longrightarrow A)\rangle, \langle P(C\longrightarrow B)\rangle, \langle P(C\longrightarrow C)\rangle)&\\ = (1/3, 1/4 - (\cos 2\delta)/12, (5 + \cos 2\delta)/12).&\end{aligned} \tag{20}$$

These average probabilities are equal only for $\delta = \pm\pi/2$.

The identification of the states $|A\rangle$, $|B\rangle$, $|C\rangle$ with the usual neutrinos states $|\nu_e\rangle$, $|\nu_\mu\rangle$, $|\nu_\tau\rangle$ is left to experiment, which, after all, observes the electrons and the muons.

5. COMPARISON TO EXPERIMENT

In this section, we compare model predictions (18) with two sets of data on neutrino oscillations: one from the SuperK and K2K experiments and the other from the KamLAND and SNO experiments. The LSND results are left out of consideration, as these have not been confirmed by another experiment. We refer to two recent reviews [2, 3] for further details and an extensive list of references.

5.1. SuperK and K2K. With neutrino energies in the GeV range, SuperK [10] discovered indirect evidence for $\nu_\mu \longrightarrow \nu_x$ oscillations starting from a distance of $L \approx 500$ km (corresponding to a zenith angle of approximately 90°). The same type of neutrino oscillations has also been inferred by K2K [11] at a distance of $L = 250$ km. Both lengths are of the same order of magnitude as Eq. (8).

For a more precise analysis, we turn to the K2K experiment. The crucial result is now that K2K [12] does *not* see $\nu_\mu \longrightarrow \nu_e$ at an appreciable level for the length $L = 250$ km where the ν_μ flux is reduced by approximately 30%. The quoted numbers of neutrino events are

$$(N_{\nu_\mu}, N_{\nu_e}, N_{\nu_\tau})\Big|^{\text{K2K}}_{L\,=\,250\text{ km}} \approx (56, 1, 23?), \tag{21}$$

where the number for N_{ν_τ} has been deduced from the expected number $N_{\nu_\mu} \approx 80 \pm 6$ without neutrino oscillations.

Taking the phase $\delta = \pi/4$, the probabilities calculated in Eq. (18) give a "best fit" for

$$\begin{aligned}80\times(P(C\longrightarrow C), P(C\longrightarrow A), P(\mathrm{C}\longrightarrow B))\Big|^{\delta\,=\,\pi/4}_{l\,=\,0.145}&\\ \sim (56, 2, 22),&\end{aligned} \tag{22}$$

with the dimensionless length l defined by

$$2\pi l \equiv B_0 L/(\hbar c) \sim \Delta. \tag{23}$$

The model numbers (22) compare well with the "observed" numbers (21).

The comparison with the K2K experiment allows for the following tentative identification,

$$(|A\rangle = |\nu_e\rangle, |B\rangle = |\nu_\tau\rangle, |C\rangle = |\nu_\mu\rangle)\Big|^{\delta\,=\,\pi/4}, \tag{24}$$

at least if δ is set to $\pi/4$ (see Section 5.2 for further discussion). With $L = 250$ km, we also have

$$B_0 \approx 0.145(hc)/(250\text{ km}) \approx 7.2\times 10^{-13}\text{ eV} \tag{25}$$

and a wavelength $\lambda \approx 1700$ km ($l = 1$). The statistical error on B_0 is estimated to be of the order of 10%, as obtained by letting the N_{ν_τ} value in Eq. (21) range from 17 to 29 and finding the matching probabilities in the model.

The K2K experiment has also analyzed the spectrum of the reconstructed energies of the μ-type neutrinos. Given the large errors, the data points agree more or less with the shape expected from the Fermi-point-splitting mechanism (box histogram in Fig. 2 of [11]).

The production rates corresponding to Eq. (22) first have a peak for *B*-type neutrinos at $l \approx 0.3$ and then a peak for *A*-type neutrinos at $l \approx 0.6$, with the *C*-type rate reduced to under 20% over the range $0.3 \lesssim l \lesssim 0.7$. For SuperK, the *C*-type (= μ-type?) atmospheric neutrinos would start being depressed at a length $L \approx 500$ km ($l \approx 0.3$), which is roughly what is observed at a zenith angle of 90°. With travel distances averaged over several thousand kilometers (corresponding to large enough zenith-angle intervals), the number of initial *C*-type neutrinos would be reduced significantly. According to Eq. (20) for $\delta = \pi/4$, an initial 2 : 1 ratio of *C*-type to *A*-type neutrinos would be changed as follows:

$$\begin{aligned}(N_{C,\bar C} : N_{A,\bar A} : N_{B,\bar B}) &= (120 : 60 : 0)\\ &\longrightarrow (50 + 20 : 40 + 20 : 30 + 20).\end{aligned} \tag{26}$$

Apparently, these averaged vacuum oscillations would keep the initial number of *A*-type (= *e*-type?) events unchanged and reduce the initial number of *C*-type (= μ-type?) events by 40%, more or less as observed by SuperK [10].

Needless to say, a complete reanalysis of the SuperK data is required if the neutrino energy is given by Eq. (6) instead of the Lorentz-invariant relation (9). The most important task would be to establish unambiguously whether or not the oscillation properties depend on the neutrino energy. (Figure 4 of [10] is not really conclusive, because the data points can also be fitted by a smoothed steplike function, which drops from a constant value 1 for $L/E_\nu \lesssim 100$ km/GeV to a constant value 0.6 for $L/E_\nu \gtrsim 400$ km/GeV.)

5.2. KamLAND and SNO. With antineutrino energies in the MeV range, KamLAND [13] presented indirect evidence for $\bar\nu_e \longrightarrow \bar\nu_x$ oscillations at a distance

$L \approx 180$ km. The experiment quotes the following survival probability:

$$P(\bar{\nu}_e \longrightarrow \bar{\nu}_e)\big|_{L \approx 180\ \mathrm{km}}^{\mathrm{KamLAND}} = 0.611 \pm 0.085(\mathrm{stat}) \pm 0.041(\mathrm{syst}). \quad (27)$$

The distance $L \approx 180$ km corresponds to $l \approx 0.104$, as defined by Eq. (23) for the tentative energy scale (25). From Eq. (18) specialized to $\delta = \pi/4$, the relevant probability for the identification (24) is

$$P(\bar{A} \longrightarrow \bar{A})\big|_{l\,=\,0.104}^{\delta\,=\,\pi/4} \sim 0.74, \quad (28)$$

which is less than two standard deviations away from the experimental result (27); cf. Fig. 4 of [13]. Note that a 10% error on the value of l translates into a 6% error for the probability (28).

The KamLAND experiment has also analyzed the positron energy spectrum from the inverse β decay used to detect the antineutrinos. The spectrum is reported to be consistent at the 53% C.L. with the expectations from the Fermi-point-splitting mechanism (upper histogram in Fig. 5 of [13] multiplied by a factor of 0.6).

Considering oscillation probabilities (18) for only two values of the phase, $\delta = 0$ and $\delta = \pi/4$, the *combined* experiments of K2K, KamLAND, and SuperK appear to favor the nonzero value of δ. As an example of a disfavored identification (actually one of the best for $\delta = 0$), we list the following numbers:

$$80 \times (P(A \longrightarrow A), P(A \longrightarrow C), P(A \longrightarrow B))\big|_{l\,=\,0.115}^{\delta\,=\,0} \sim (56, 2, 22), \quad (29)$$

$$P(\bar{C} \longrightarrow \bar{C})\big|_{l\,=\,0.083}^{\delta\,=\,0} \sim 0.92. \quad (30)$$

The first set of numbers compares well with the K2K data (21), but the second number is rather far from the KamLAND result (27). The SuperK results, which indicate $\nu_\mu \longrightarrow \nu_x$ wavelengths of at least 1000 km, also help to rule out certain other $\delta = 0$ identifications.

The model predictions for $\delta = -\pi/4$ and $\delta = \pm\pi/2$ have also been compared with the experimental data, and "best fits" are found with numbers similar to those of Eqs. (29) and (30) or worse. The $\delta = \pi/4$ identification (24) seems to be preferred among the cases considered, at least for Fermi point splittings (12) and mixing angles (13). Note that the δ range can be restricted to $[-\pi/2, \pi/2]$, since B and C switch roles in probabilities (18) for $\delta \longrightarrow \delta + \pi$.

The preliminary result for the T-violating phase is then

$$\delta \approx -3\pi/4 \text{ or } \pi/4, \quad (31)$$

with identifications $|A\rangle = |\nu_e\rangle$, $|B\rangle = |\nu_\mu\rangle$, $|C\rangle = |\nu_\tau\rangle$ for the case of $\delta = -3\pi/4$ and identifications (24) for $\delta = \pi/4$. A comprehensive statistical analysis remains to be performed in order to determine the error on these values for δ.

In contrast to KamLAND, the experiments of CHOOZ [14] and Palo Verde [15] failed to see evidence for $\bar{\nu}_e \longrightarrow \bar{\nu}_x$ oscillations at $l \approx 1$ km. This would be consistent with probabilities (18),

$$P(\bar{A} \longrightarrow \bar{A}) = 1 - \mathrm{O}(\Delta_l^2), \quad P(\bar{A} \longrightarrow \bar{B}) = \mathrm{O}(\Delta_l^2), \quad P(\bar{A} \longrightarrow \bar{C}) = \mathrm{O}(\Delta_l^2), \quad (32)$$

for $|\bar{A}\rangle = |\bar{\nu}_e\rangle$ and with $\Delta_l \equiv B_0 l/(\hbar c) \approx l/(270\ \mathrm{km}) \ll 1$ for energy scale (25). Remarkably, this general reduction of the off-diagonal oscillation probabilities does not require $\sin 2\theta_{13}$ to be close to zero, as would be the case for mass oscillations (10), (11) with $|m_1^2 - m_3^2| \approx 2 \times 10^{-3}\ \mathrm{eV}^2/c^4$ and $E_\nu \approx 3$ MeV [14, 15].

As to solar neutrinos, SNO [16, 17] has definitely established flavor oscillations, with the initial *e*-type neutrinos distributed over the three flavors and their flux reduced to approximately 30%. Vacuum oscillations of neutrinos with Fermi point splittings (12) and tri-maximal mixing angles (13) have an average *e*-type survival probability of 1/3, according to Eqs. (20) and (24). Matter effects can be expected to play a role because the matter-oscillation length scale $hc/(2\sqrt{2}\,G_F n_e)$ is approximately 100 km in the center of the Sun [3], which is definitely less than our length scale (8). But, in the end, matter effects may be rather unimportant if the vacuum mixing angles are close to $\pi/4$.

It is not clear how well our neutrinos with Fermi point splittings fit all the solar neutrino data from SNO and the other experiments [2, 3]. Obviously, a complete reanalysis of neutrino propagation in the Sun is required if the vacuum dispersion law is given by Eq. (6).

There is also the possibility of further effects from small neutrino masses with their own matrix structure; cf. [6]. These small masses could affect flavor oscillations of solar neutrinos with relatively low energy ($E_\nu \lesssim 1$ MeV for $|\Delta m^2| \approx 10^{-6}\ \mathrm{eV}^2/c^4$), whereas oscillations of neutrinos with higher energy would be primarily determined by the Fermi point splittings (25).

6. CONCLUSIONS

The present letter has shown that energy-independent neutrino oscillations from the timelike splitting of Fermi points [7] need not be in flagrant contradiction with the experimental data [10–17].

For the sake of argument, we have considered a simple model (12)–(14) with two free parameters: the energy scale B_0 and the phase δ. The mixing angles of this model are fixed to values (13) by the condition that they maximize function (15) for a given phase δ. It turns out that the model can more or less explain the results of the K2K and KamLAND experiments, with a

fundamental energy scale B_0 of the order of 10^{-12} eV and a preference for a nonzero T-violating phase, $\sin^2\delta \approx 1/2$. (These numerical values are, of course, to be considered preliminary.) There is also rough agreement with the data on atmospheric neutrinos (SuperK) and solar neutrinos (SNO), but further analysis is needed.

The tentative conclusion is that the simple Ansatz (12), (13) for neutrino dispersion law (6) and mixing matrix (14) may be compatible with experiment. The model considered can, of course, be perturbed by changes in the energy scales and mixing angles and by the addition of small mass terms. More importantly, the Ansatz suggests an entirely new structure of the neutrino sector, with the possibility of relatively strong T (and CP?) violation.

We end this letter with four general remarks. First, the spacelike splitting of Fermi points is a possibility not considered in detail here, as the phenomenology would certainly be more complicated due to the presence of anisotropies; cf. Eq. (4). Second, left-handed antineutrinos (with hypercharge $Y_{\bar{\nu}_L} = 0$) drop out for patterns (2) and (5) but could perhaps play a role in further mass generation. Third, it remains to be seen how the Fermi point splittings of the massless (or nearly massless) neutrinos feed into the charged-lepton sector; cf. [18]. Fourth, theory and experiment need to elucidate the precise role, if any, of CP, T, and CPT violation in the neutrino sector.

The author thanks G.E. Volovik for extensive discussions and M. Jezabek and the referees for useful comments on the manuscript.

REFERENCES

1. S. M. Bilenky and B. Pontecorvo, Phys. Rep. **41**, 225 (1978).
2. V. Barger, D. Marfatia, and K. Whisnant, Int. J. Mod. Phys. E **12**, 569 (2003); hep-ph/0308123.
3. R. D. McKeown and P. Vogel, Phys. Rep. **394**, 315 (2004); hep-ph/0402025.
4. M. Gasperini, Phys. Rev. D **38**, 2635 (1988).
5. A. Halprin, C. N. Leung, and J. Pantaleone, Phys. Rev. D **53**, 5365 (1996); hep-ph/9512220.
6. S. Coleman and S. L. Glashow, Phys. Rev. D **59**, 116008 (1999); hep-ph/9812418.
7. F. R. Klinkhamer and G. E. Volovik, hep-th/0403037.
8. B. Kayser, Phys. Rev. D **24**, 110 (1981).
9. C. Jarlskog, Phys. Rev. Lett. **55**, 1039 (1985).
10. Y. Fukuda *et al.* (Super-Kamiokande Collab.), Phys. Rev. Lett. **81**, 1562 (1998); hep-ex/9807003.
11. M. H. Ahn *et al.* (K2K Collab.), Phys. Rev. Lett. **90**, 041801 (2003); hep-ex/0212007.
12. M. H. Ahn *et al.* (K2K Collab.); hep-ex/0402017.
13. K. Eguchi *et al.* (KamLAND Collab.), Phys. Rev. Lett. **90**, 021802 (2003); hep-ex/0212021.
14. M. Apollonio *et al.*, Eur. Phys. J. C **27**, 331 (2003); hep-ex/0301017.
15. F. Boehm *et al.*, Phys. Rev. D **64**, 112001 (2001); hep-ex/0107009.
16. Q. R. Ahmad *et al.* (SNO Collab.), Phys. Rev. Lett. **89**, 011301 (2002); nucl-ex/0204008.
17. S. N. Ahmed *et al.* (SNO Collab.), Phys. Rev. Lett. **92**, 181301 (2004); nucl-ex/0309004.
18. I. Mocioiu and M. Pospelov, Phys. Lett. B **534**, 114 (2002); hep-ph/0202160.

JETP Letters, Vol. 79, No. 10, 2004, pp. 457–463. From Pis'ma v Zhurnal Éksperimental'noĭ i Teoreticheskoĭ Fiziki, Vol. 79, No. 10, 2004, pp. 569–574.

Vacuum Expectation Values from Fusion of Vertex Operators¶

Y. Pugai

Landau Institute for Theoretical Physics, Russian Academy of Sciences, Moscow, 117940 Russia

e-mail: slava@landau.ac.ru

Received April 6, 2004; in final form, April 15, 2004

The algebra of fused vertex operators for the ABF model is defined and studied in the free fields approach. Vacuum expectation values of local operators in the scaling theory are reproduced from the matrix elements of the fused vertex operators. © *2004 MAIK "Nauka/Interperiodica".*

PACS numbers: 05.50.+q; 05.20.-y

The algebraic approach to the two-dimensional exactly solvable models of the Statistical Mechanics [1, 2] turns out to be a very effective tool for finding integral representations for correlation functions and form factors of local operators. In this approach, a Hamiltonian of a model in the thermodynamic limit is diagonalized exactly by the use of the so-called vertex operators (generators of a quadratic associative algebra). In the present work, we extend the construction of the "Interaction Round a Face" type algebras [3–6] for the case of fused vertex operators and apply it to a description of the local operators in a corresponding massive scaling theory. For definiteness, we elaborate the procedure for the Andrews–Baxter–Forrester (ABF) [7] integrable models of Statistical Mechanics. In what follows, we identify the fused vertex operators with the operators inserting lattice spins. We argue that, in the scaling limit [8, 9], the proposed bosonic operators determine vacuum expectation values of the local operators [10] of the theory. The last quantities, carrying all nonperturbative information on the theory, are of fundamental importance since they define both short- and long-distance asymptotics [11] of the scaling correlation functions.

The fluctuation variables in the ABF models (and their nonunitary generalizations) are associated with sites of a two-dimensional square lattice and take integer values $1 \le k \le p' - 1$. In regime III, there are $p - 1$ ground states $1 \le l \le p - 1$ in the model. The parameterization of the Boltzmann weights is given in terms of the elliptic theta functions $\theta_1(u|\tau)$ with the elliptic nome $e^{2\pi i\tau}$. We use the shorthand notation for the ratios of theta functions

$$[u] := \theta_1\left(\frac{\pi u}{\xi+1}\middle|\frac{i\pi}{(\xi+1)\epsilon}\right)/\theta_1\left(\frac{\pi}{\xi+1}\middle|\frac{i\pi}{(\xi+1)\epsilon}\right).$$

Here, $\xi := p/p' - p$, while $\epsilon > 0$ and $0 < u < 1$ are, respectively, the parameter measuring deviation from criticality and the spectral parameter. A local Boltzmann weight $\mathbf{U}$ is assigned to every configuration (m_a, m_b, m_c, m_d) of heights round a face with the sites (a, b, c, d). The nonvanishing Boltzmann weights satisfying the Yang–Baxter equation (YBE) are given (up to a gauge transform) as follows:

$$\mathbf{U}\begin{bmatrix} m\pm 2 & m\pm 1 \\ m\pm 1 & m \end{bmatrix} = R,$$

$$\mathbf{U}\begin{bmatrix} m & m\pm 1 \\ m\pm 1 & m \end{bmatrix} = R\frac{[m\pm u]}{[1-u][m]}, \qquad (1)$$

$$\mathbf{U}\begin{bmatrix} m & m\pm 1 \\ m\mp 1 & m \end{bmatrix} = R\frac{[\pm 1-m]}{[m]}\frac{[u]}{[1-u]}.$$

It is convenient to choose the factor R here to be such that the partition function per face in the thermodynamic limit equals one

$$R(u) = e^{-\frac{\xi}{\xi+1}u\epsilon} \times \exp\left\{\sum_{m=-\infty}^{\infty}\frac{\sinh m\epsilon\sinh\xi m\epsilon}{m\sinh(\xi+1)m\epsilon\sinh 2m\epsilon}e^{-2u\epsilon m}\right\}. \qquad (2)$$

The vertex operator algebra [2] is a quadratic graded associative algebra with the coefficients satisfying the YBE. The simplest case based on (1) has already been studied in [4, 5]. The solutions of the YBE which appear in the definition of new vertex operator algebras are essentially Boltzmann weights appearing in the construction of the fusion ABF models [12]. (Note that we use an obvious generalization for the case of ratio-

¶ This article was submitted by the author in English.

nal values of the parameter ξ.) For integers $0 < \nu \le \mu < p' - 1$, let $a, b, c, d \in \{1, \ldots, p' - 1\}$ satisfy the conditions $a - b, c - d = -\mu, -\mu + 2, \ldots, \mu$; $a - d, b - c = -\nu, -\nu + 2, \ldots, \nu$. Starting from $\mathbf{U}$ in Eq. (1), we introduce the following notations:

$$\mathbf{U}_{\nu\mu}\left[\begin{array}{cc} a & b \\ d & c \end{array}\middle| u\right] := \sum_{\{a_{i,j}\}} \prod_{i=0}^{\nu-1} \prod_{j=0}^{\mu-1} \mathbf{U}\left[\begin{array}{cc} a_{i+1,j+1} & a_{i+1,j} \\ a_{i,j+1} & a_{i,j} \end{array}\middle| \tilde{u}\right],$$

with $\tilde{u} := u + \frac{\mu - \nu}{2}\xi + (i - j)\xi$. The sum is taken over all values of $a_{i,j}$ allowed due to (1), while the variables $a_{0,j}$, $(0 \le j < \mu)$, $a_{i,\mu}$, $(0 \le i < \nu)$ are fixed. According to [12] the result depends only on the indexes $a = a_{\nu,\mu}$, $b = a_{\mu,0}$, $c = a_{0,0}$, $d = a_{0,\mu}$ and does not depends on $\{a_{0,j}, j = 1, \ldots, \mu - 1\}$ and $\{a_{i,\mu}, i = 1, \ldots, \nu - 1\}$. Though the expressions for the general solution of the YBE are rather complicated, our analysis depends basically on the properties of the $\mathbf{U}_{1\mu}$ fused weights, which can be written out explicitly

$$\mathbf{U}_{1\mu}\left[\begin{array}{cc} m'+1 & m+1 \\ m' & m \end{array}\middle| u\right] = \frac{R_{1\mu}(u)}{[m][\mu - \bar{u}]} \times \left[\frac{m + m' - \mu}{2}\right]\left[\frac{m' - m + \mu}{2} - \bar{u}\right],$$

$$\mathbf{U}_{1\mu}\left[\begin{array}{cc} m'-1 & m+1 \\ m' & m \end{array}\middle| u\right] = \frac{R_{1\mu}(u)}{[m][\mu - \bar{u}]} \times \left[\frac{m' - m + \mu}{2}\right]\left[\frac{m' + m - \mu}{2} + \bar{u}\right],$$

$$\mathbf{U}_{1\mu}\left[\begin{array}{cc} m'+1 & m-1 \\ m' & m \end{array}\middle| u\right] = \frac{R_{1\mu}(u)}{[m][\mu - \bar{u}]} \times \left[\frac{m - m' + \mu}{2}\right]\left[\frac{m' + m + \mu}{2} - \bar{u}\right],$$

$$\mathbf{U}_{1\mu}\left[\begin{array}{cc} m'-1 & m-1 \\ m' & m \end{array}\middle| u\right] = \frac{R_{1\mu}(u)}{[m][\mu - \bar{u}]} \times \left[\frac{m + m' + \mu}{2}\right]\left[\frac{m - m' + \mu}{2} - \bar{u}\right].$$

Here, $\bar{u} := u - \frac{\mu - 1}{2}\xi$ and the factor $R_{1\mu}(u)$ is

$$R_{1\mu}(u) = R\left(u - \frac{\mu - 1}{2}\xi\right)R\left(u - \frac{\mu - 3}{2}\xi\right)\ldots R\left(u + \frac{\mu - 1}{2}\xi\right).$$

We will use symmetric Boltzmann weights obtained from $\mathbf{U}_{\nu\mu}$ by applying the "gauge" transform

$$\mathbf{W}_{\nu\mu}\left[\begin{array}{cc} a & b \\ d & c \end{array}\middle| u\right] = \frac{\epsilon_b}{\epsilon_d}\left(\frac{(ab)_\mu (bc)_\nu}{(cd)_\mu (ad)_\mu}\right)^{\frac{1}{2}} \mathbf{U}_{\nu\mu}\left[\begin{array}{cc} a & b \\ d & c \end{array}\middle| u\right].$$

Here, $\epsilon_a = \pm 1$, $\epsilon_a \epsilon_{a+1} = (-1)^a$ and the symbols $(a, b)_\mu \equiv (b, a)_\mu$ are defined via the theta functions

$$(a, b)_\mu = \left[\begin{array}{c} \mu \\ \frac{a - b + \mu}{2} \end{array}\right]^{-1} \frac{\left[\frac{a + b - \mu}{2}, \frac{a + b + \mu}{2}\right]}{\sqrt{[a][b]}},$$

where $[a, b] := [a][a + 1]\ldots[b]$, $[a, a - 1] = 1$. The set of functions $\mathbf{W}_{\nu\mu}$ satisfy the Yang–Baxter equation

$$\sum \mathbf{W}_{\nu\mu}\left[\begin{array}{cc} a & s \\ e & f \end{array}\middle| u_1\right]\mathbf{W}_{\nu\tau}\left[\begin{array}{cc} s & b \\ f & c \end{array}\middle| u_2\right]\mathbf{W}_{\tau\mu}\left[\begin{array}{cc} e & f \\ c & d \end{array}\middle| u\right]$$

$$= \sum \mathbf{W}_{\nu\tau}\left[\begin{array}{cc} a & f \\ f & e \end{array}\middle| u_2\right]\mathbf{W}_{\nu\mu}\left[\begin{array}{cc} f & b \\ d & c \end{array}\middle| u_1\right]\mathbf{W}_{\tau\mu}\left[\begin{array}{cc} a & s \\ f & b \end{array}\middle| u\right],$$

where $u := u_1 - u_2$ and the sum is taken over all allowed values of the variable f.

We check that the functions $R_{1\mu}(u)$ are subjects of the inversion relations $R_{1\mu}(-u)R_{1\mu}(u) = 1$ and

$$R_{1\mu}(u)R_{1\mu}(u + 1) = \left[u + \frac{\mu - 1}{2}\xi\right]/\left[u + 1 - \frac{\mu - 1}{2}\xi\right]. \quad (3)$$

Using this property and Theorem 2.15 from [12], it is easy to verify that the weights $\mathbf{W}_{1\mu}$ satisfy the symmetry conditions

$$\mathbf{W}_{1\mu}\left[\begin{array}{cc} a & b \\ d & c \end{array}\middle| u\right] = \mathbf{W}_{1\mu}\left[\begin{array}{cc} c & d \\ b & a \end{array}\middle| u\right],$$

$$\mathbf{W}_{\mu 1}\left[\begin{array}{cc} b & c \\ a & d \end{array}\middle| u\right] = (-)^{\mu - 1}\sqrt{\frac{[a][c]}{[b][d]}}\mathbf{W}_{1\mu}\left[\begin{array}{cc} a & b \\ d & c \end{array}\middle| 1 - u\right], \quad (4)$$

as well as the inversion relation

$$\sum_d \mathbf{W}_{\mu 1}\left[\begin{array}{cc} a & d \\ b' & c \end{array}\middle| -u\right]\mathbf{W}_{1\mu}\left[\begin{array}{cc} a & b \\ d & c \end{array}\middle| u\right] = \delta_{b,b'}. \quad (5)$$

Heuristically the (so-called type I) operators in the Vertex Operator Approach [2] to the ABF model are defined as half-infinite products of the Boltzmann weights $\mathbf{W}_{11}$ [2, 5]. It seems natural to generalize the construction for an extended operator algebra by implying the fusion procedure. We introduce the space $\mathcal{L}_{l,k}$

($1 \le l \le p-1$, $1 \le k \le p'-1$) as a set of vectors (a_0, a_1, a_2, …) such that $a_0 \equiv k$, $|a_j - a_{j+1}| = 1$ and the sequence $\{a_j\}$ stabilizes to l, $l+1$, l, $l+1$, … for $j \gg 1$. Let us define half-infinite products of the fused Boltzmann weights $\mathbf{W}_{1\mu}$

$$\Phi^{ab}_{1,\mu+1}(u)^{(a,a_1,a_2,\ldots)}_{(b,b_1,b_2,\ldots)} := \prod_{j=0}^{\infty} W_{1\mu}\left[\begin{array}{cc} b_{j+1} & a_{j+1} \\ b_j & a_j \end{array}\middle| u\right],$$

where $|b_j - b_{j+1}| = |a_j - a_{j+1}| = 1$, $a_0 = a$, $b_0 = b$, and treat it as an element of the half-infinite matrix $\Phi^{ab}_{1,\mu+1}(u)$ sending the vector $(b, b_1, b_2, \ldots) \in \mathcal{L}_{l,b}$ to the vector $(a, a_1, a_2, \ldots) \in \mathcal{L}_{l,a}$

$$\Phi^{(ab)}_{1,\mu+1} : \mathcal{L}_{l,b} \longrightarrow \mathcal{L}_{l,a}. \tag{6}$$

The subtle point which we want to point out is that the matrix element of the "conjugate" operator

$$\Phi^{*ab}_{1,\mu+1}(u)^{(a,a_1,a_2,\ldots)}_{(b,b_1,b_2,\ldots)} := \prod_{j=0}^{\infty} \mathbf{W}_{1\mu}\left[\begin{array}{cc} a_j & b_j \\ a_{j+1} & b_{j+1} \end{array}\middle| u\right]$$

coincides with that for $\Phi^{(ab)}_{1,\mu+1}$ due to Eq. (4). This requirement fixes a freedom in choosing a gauge transform.

The heuristic definition given above allows one to derive the axioms for the vertex operator algebra. First, applying the YBE to a product of two operators, we conclude that $\Phi_{1\mu+1}$ generate a quadratic associative algebra

$$\Phi^{(cb)}_{1,\mu+1}(u_2)\Phi^{(ba)}_{1,\nu+1}(u_1) = \sum_d \mathbf{W}_{\nu\mu}\left[\begin{array}{cc} a & d \\ b & c \end{array}\middle| u_{21}\right]\Phi^{(cd)}_{1,\nu+1}(u_1)\Phi^{(da)}_{1,\mu+1}(u_2). \tag{7}$$

Second, from inversion relations (5), we find that vertex operators have to satisfy the normalization condition

$$\Phi^{(1,\mu+1)}_{1,\mu+1}(u)\Phi^{(\mu+1,1)}_{1,\mu+1}(u+1) = \frac{(-1)^{\mu-1}}{\sqrt{[\mu+1]}}. \tag{8}$$

In addition, it is assumed that the algebra can be extended by the so-called "Corner Hamiltonian" [1, 2, 5] element $H : \mathcal{L}_{lk} \longrightarrow \mathcal{L}_{lk}$ acting diagonally in the space of states. Its action on the vertex operators is defined as

$$e^{-2\epsilon\nu H}\Phi_{1\mu+1}(u)e^{2\epsilon\nu H} = \Phi_{1\mu+1}(u+\nu). \tag{9}$$

The last requirement which we impose is that the spectrum of D is described by the following formula [7]:

$$Tr_{\mathcal{L}_{lk}}[q^H] = \chi_{lk}(q), \tag{10}$$

where $\chi_{lk}(q)$ is the character of the irreducible representation of the Virasoro algebra with the central charge and the highest weight vector being, respectively,

$$c = 1 - \frac{6}{\xi(\xi+1)}, \quad \Delta_{lk} = \frac{((\xi+1)l - \xi k)^2 - 1}{4\xi(\xi+1)}. \tag{11}$$

To describe the matrix elements (and traces) of vertex operators satisfying properties (6)–(10), we use the free field technique originally developed in the CFT context [13–15] and generalized for the elliptic case in the works [3–6, 16]. Here, we formulate main propositions on the properties of the bosonization procedure and add missing proofs.

Let us introduce the free bosonic field

$$\phi(u) = -\sqrt{\frac{\xi}{2(\xi+1)}}(\mathcal{Q} + 2i\epsilon u\mathcal{P}) + i\sum_{m \in Z/\{0\}} \frac{\beta_m}{m} e^{2\epsilon u m},$$

where the nontrivial commutation relations for the zero modes $\mathcal{Q}$, $\mathcal{P}$ and oscillators β_m are given as

$$[\mathcal{P}, \mathcal{Q}] = -i,$$
$$[\beta_m, \beta_n] = m\frac{\sinh m\epsilon \sinh \xi m\epsilon}{\sinh 2m\epsilon \sinh(\xi+1)m\epsilon}\delta_{m+n}.$$

On the Fock module $\mathcal{F}_{lk} = \{\beta_{m_1}, \ldots, \beta_{m_N}|l, k\rangle, m_1 \le \ldots \le m_N < 0\}$ with the highest weight vector $|l, k\rangle$, the zero mode $\mathcal{P}$ acts as a number,

$$\omega|l, k\rangle := \sqrt{2\xi(\xi+1)}\mathcal{P}|l, k\rangle = ((\xi+1)l - \xi k)|l, k\rangle,$$

while $\beta_m|l, k\rangle = 0$, $m > 0$. The grading operator in the Fock space is naturally defined as

$$D = \sum_{m=1}^{\infty} \frac{\sinh(\xi+1)m\epsilon \sinh 2m\epsilon}{\sinh m\epsilon \sinh \xi m\epsilon}\beta_{-m}\beta_m + \frac{\mathcal{P}^2}{2} - \frac{1}{24}.$$

The vertex operators will be expressed in terms of the exponents of the free bosonic field $V_\mu : \mathcal{F}_{l,k} \longrightarrow \mathcal{F}_{l,k+\mu}$ and $\bar{V} : \mathcal{F}_{l,k} \longrightarrow \mathcal{F}_{l,k-2}$

$$V_\mu(u) = \exp\left(i\sum_{j=0}^{\mu-1}\phi\left(u + \frac{\mu - 2j - 1}{2}\xi\right)\right),$$
$$\bar{V}(\nu) = \exp\left(-i\phi\left(\nu + \frac{1}{2}\right) - i\phi\left(\nu - \frac{1}{2}\right)\right). \tag{12}$$

Define Lukyanov's screening operator as an integral operator

$$X_n(u) = \frac{[n]!}{n!}\left(\frac{-\epsilon}{\eta}\right)^n \int \frac{dv_1}{\pi i}\cdots\frac{dv_n}{\pi i}\prod_{i<j}\frac{[v_i - v_j]}{[v_i - v_j - 1]} \times \prod_{s=1}^{n}\frac{[v_s - u - \mu/2 - \omega - n + 1]}{[v_s - u - \mu/2]}\bar{V}(v_1)\ldots\bar{V}(v_n). \quad (13)$$

Here, the integration is from u to $u + i\pi/\epsilon$ and η is a normalization constant which will be specified later. We claim that *acting in the direct sum of the Foci spaces* $\oplus\mathcal{F}_{lk}$, *the following screened vertex operators*

$$V_\mu^{(s)}(u) = X_s(u)V_\mu(u) : \mathcal{F}_{l,a} \longrightarrow \mathcal{F}_{l,a+\mu-2s} \quad (14)$$

satisfy quadratic relations (7) but with the coefficients given by $\mathbf{U}_{v\mu}$.

Knowing the exact formulas for bosonization (12)–(14), it is easy to derive matrix elements of the screened operators and analyze its properties. (It is convenient for us to work with integrals using the multiplicative variables $z = x^{2v}$, $x = e^{-\epsilon}$.) The oscillator modes contributions for the exponential operators

$$\langle V_\mu(0)V_\mu(u)\rangle_{\text{osc}} = \rho_\mu^2 g_\mu(e^{-2u\epsilon}),$$
$$\langle \bar{V}(0)V_\mu(u)\rangle_{\text{osc}} = \rho_\mu\bar{\rho}w_\mu(e^{-2u\epsilon}), \quad (15)$$
$$\langle \bar{V}(0)\bar{V}(v)\rangle_{\text{osc}} = \bar{\rho}^2\bar{w}(e^{-2u\epsilon}),$$

are given as following

$$g_\mu(\zeta) = \frac{\{x^{2\xi+4}\zeta\}_\infty^2\{x^{2\xi+2+2\xi\mu}\zeta\}_\infty\{x^{2\xi+2-2\xi\mu}\zeta\}_\infty}{\{x^{2\xi+2}\zeta\}_\infty^2\{x^{2\xi+4+2\xi\mu}\zeta\}_\infty\{x^{2\xi+4-2\xi\mu}\zeta\}_\infty},$$
$$w_\mu(z) = \frac{(x^{1+(\mu+1)\xi}z)_\infty}{(x^{1-(\mu-1)\xi}z)_\infty}, \quad \bar{w}(z) = (1-z)\frac{(x^2z)_\infty}{(x^{2\xi}z)_\infty}.$$

Here and below, we use the definitions for infinite products

$$(z)_\infty := \prod_{j=0}^{\infty}(1 - zx^{2(\xi+1)j}),$$
$$\{z\}_\infty := \prod_{i,j,m=0}^{\infty}(1 - zx^{2(\xi+2)i}x^{2\xi j}x^{4m}).$$

The constants ρ_μ and $\bar{\rho}$ enter the expression for matrix elements in the combinations ρ_μ^2 and $\eta^{-1}\bar{\rho}$ only. The last ones turn out to be

$$\rho_\mu^2 = g_\mu(1), \quad \eta^{-1}\bar{\rho} = x^{\frac{\xi}{2(\xi+1)}}\frac{(x^{2(\xi+1)})_\infty}{(x^{2\xi})_\infty}.$$

Using these formulas, we find, for instance, that the two points matrix element of the vertex operators V_μ

$$G_\mu(e^{-2\epsilon u}) := \langle 11|V_\mu^{(\mu)}(0)V_\mu^{(0)}(u)|11\rangle$$

defining the normalization of these operators is given in terms of the μ-fold integral

$$G_\mu(\zeta) = \left(\frac{\bar{\rho}x^{-\frac{\xi}{2(\xi+1)}}}{\eta(x^{2(\xi+1)})_\infty^1}\right)^\mu(\zeta x^{-2})^{\Delta_{1\mu+1}}g_\mu(\zeta)\rho_\mu^2 \times\frac{[\mu]!}{\mu!}\oint\ldots\oint\frac{dz_1}{2\pi i z_1}\cdots\frac{dz_\mu}{2\pi i z_\mu}\prod_{i\neq j}\frac{(z_i/z_j)_\infty}{(z_i x^{2\xi}/z_j)_\infty} \times\prod_{s=1}^{\mu}\frac{E(z_s x^{-1+\xi(\mu+1)})}{(z_s x^{1-(\mu-1)\xi})_\infty(x^{1-(\mu-1)\xi}/z_s)_\infty} \times\frac{E(z_s x^{1-\xi(\mu-1)}/\zeta)}{(z_s x^{1-(\mu-1)\xi}/\zeta)_\infty(\zeta x^{1-(\mu-1)\zeta}/z_s)_\infty}, \quad (16)$$

where $E(z) := (x^{2(\xi+1)})_\infty(z)_\infty(x^{2(\xi+1)}z^{-1})_\infty$. The integral can be transformed to the Askey–Roy type integral for which the explicit expression is known [17]. Applying the identity

$$g_\mu(\zeta)g_\mu(\zeta x^{-2}) = \prod_{s=0}^{\mu-1}\frac{(\zeta x^{-2\xi s})_\infty}{(\zeta x^{2\xi(s+1)})_\infty},$$

we arrive finally at the following elegant expression for the matrix element of two screened operators:

$$G_\mu(x^{2u}) = [\mu]!\epsilon_1\epsilon_{\mu+1}\frac{Q_\mu(x^{2u})}{Q_\mu(x^2)},$$
$$Q_\mu(\zeta) = \zeta^{\Delta_{1\mu}}g_\mu(\zeta)\prod_{s=0}^{\mu-1}\frac{(\zeta x^{2\xi(s+1)})_\infty}{(\zeta x^{2-2\xi s})_\infty}. \quad (17)$$

It is obvious now that $G_\mu(x^2) = [\mu]!\epsilon_1\epsilon_{m+1}$.

Until now we concentrated on the operators acting in $\oplus\mathcal{F}_{l,k}(l, k \in Z)$. It is possible to prove that bosonic fields (14), in fact, can be restricted to a smaller space, $\oplus\mathcal{L}_{l,k}(1 \le l \le p-1, 1 \le k \le p'-1)$, the direct sum of irreducible representations of the deformed Virasoro algebra [4, 5, 18]. Let us recall its construction via a BRST reduction generalizing [15]. Consider the sequence of the maps

$$\ldots \xrightarrow{X^{(-1)}} \mathcal{F}_{l,k} \xrightarrow{X^{(0)}} \mathcal{F}_{l,-k} \xrightarrow{X^{(1)}} \mathcal{F}_{m,k-2p'} \xrightarrow{X^{(2)}} \ldots \quad (18)$$

defined by the action of the appropriate screening charges $X_s(0)$, i.e.,

$$X^{(2j)} = X_k : \mathcal{F}_{l,k-2jp'} \longrightarrow \mathcal{F}_{m,-k-2jp'},$$
$$X^{(2j+1)} = X_{p'-k} : \mathcal{F}_{l,-k-2jp'} \longrightarrow \mathcal{F}_{l,k-2(j+1)p'}.$$

It was proposed in [5, 6] that the following statements are true for $\epsilon > 0$.

I. *The chain of maps (18) is a BRST complex, i.e.*,

$$X^{(j)}X^{(j-1)} = 0. \tag{19}$$

II. *The cohomologies of the complex turn out to be nontrivial only for j = 0*

$$\mathrm{Ker}X^{(j)}/\mathrm{Im}X^{(j-1)} = 0, \text{ if } j \neq 0. \tag{20}$$

III. *Bosonic operators act in the spaces of cohomologies* $\mathcal{L}_{lk} \equiv \mathrm{Ker}X^{(0)}/\mathrm{Im}X^{(-1)}$. *(These spaces coincide with the irreducible representations of the Deformed Virasoro algebra [4, 5, 18].)*

Proof. The first statement has already been established in [16], based on the fact that the screening operator X_n can be identified with X_1^n acting on the correspondent space.

To prove the second statement, we follow word by word the line of the proof of [15] but for the deformed $\epsilon > 0$ case. Taking into account the results on the representation structure of the deformed Virasoro algebra [18], the only missing step would be that the screening charge $X^{(j)}$ is nontrivial. This, in turn, follows from the fact that for $1 \le k \le p' - 1$ and $l < 0$ there exists a nonvanishing matrix element of the form

$$J = \langle l, -k|\beta_{n_1}^{s_1}\ldots\beta_{n_j}^{s_j}X^k|l, k\rangle,$$

with $s_i \in N$, $0 < n_1 < n_2 < \ldots < n_j$ and $\sum s_i n_i = -l$. From the commutation relations

$$[\beta_m, \bar{V}(v)] = -\frac{\sinh(\xi m\epsilon)}{\sinh(\xi+1)m\epsilon}z^m,$$

we show that the integrand of J contains the multiples $\sum_{i=1}^{j}\left(\sum_{t=1}^{k} z_t^{n_i}\right)^{s_i}$ which form a basis in the space of symmetric polynomials of degree $|lk|$ in $z_1, \ldots, z_k$. Therefore we can choose an element which would produce $(z_1, \ldots, z_k)^{|l|}$. Using the expression for the couplings of exponential operators (15), we find that the problem is reduced to computation of the q-beta integral:

$$\oint\frac{dz_1}{2\pi i z_1}\cdots\frac{dz_k}{2\pi i z_k}\prod_{s=1}^{k}\frac{E(z_j x^{-1+2\xi(k-2s+1)})}{(z_j x^{-1})_\infty (x^{2\xi+3}z_j^{-1})_\infty}$$

$$\times\prod_{1\le a<b\le k}\left(1-\frac{z_a}{z_b}\right)\frac{(x^2 z_a/z_b)_\infty}{(x^{2\xi}z_a/z_b)_\infty} \tag{21}$$

$$= \prod_{s=1}^{k}\frac{E(x^{2\xi s})}{E(x^{2\xi})}\frac{(x^{2(\xi+1)}x^{2\xi(s-1)})_\infty}{(x^{2\xi s})_\infty},$$

which is nonzero for $1 \le k \le p' - 1$. Repeating the remaining arguments of [15], we verify the proposition.

To show that the vertex operators of the first type act in the cohomologies of the Felder complex, we have to show the commutativity of the following diagram:

$$\begin{array}{ccc} \mathcal{F}_{l,k} & \xrightarrow{V_\mu^{(s)}} & \mathcal{F}_{l,k+\mu-2s} \\ {\scriptstyle X_k}\downarrow & & \downarrow{\scriptstyle X_{k+\mu-2s}} \\ \mathcal{F}_{l,-k} & \xrightarrow{V_\mu^{(\mu-s)}} & \mathcal{F}_{l,-k-\mu+2s} \end{array} \tag{22}$$

This can be proven from the $\mu = 1$ case using the commutation relations between X_k and V_1 derived in [19]

$$X_{k+1-2s}(u_0)V_1^{(s)}(u)|_{\mathcal{F}_{l,k}} = V_1^{(1-s)}(u)X_k(u_0)|_{\mathcal{F}_{l,k}}. \tag{23}$$

This completes the proof of the statements on the BRST complex.

We identify the lattice space of states $\mathcal{L}_{lk}$ with the cohomologies spaces of the Felder resolution. As for operators, we provide the restriction of the following bosonic operators:

$$H|_{\mathcal{L}_{l,a}} = D|_{\mathcal{L}_{l,a}},$$

$$\Phi_{1,\mu+1}^{b,a}\big|_{\mathcal{L}_{l,a}} = \frac{\epsilon_b}{\sqrt{(ab)_\mu}}V_\mu^{(a-b+\mu)/2}\big|_{\mathcal{L}_{l,a}}. \tag{24}$$

Collecting the results described above, we finally are able to extend the statements of [5] to the following proposition for the $1 \le \mu \le p' - 1$ case:

The bosonic operators in Eq. (14, 24) satisfy commutation relations (7) and (9), normalization condition (8), and character property (10).

In the rest of the paper, we would like to emphasize that the proposed bosonization construction for the vertex operators carries important information on the local operators of the scaling theory. Indeed, according to [20], the vacuum expectation values of the primary operators in the scaling $\epsilon \longrightarrow 0$ limit of the ABF model should be defined as $\langle\hat{\Phi}_{1k}\rangle = (-1)^{k-1}\langle 1k|\exp(-\pi^2 H/\epsilon)|1k\rangle$, where $\exp(-\pi^2/2\epsilon)$ is a temperature-like parameter. We propose that the projection on the highest weight vectors $|1k\rangle$ is a result of insertion of two vertex operators $\Phi_{1,k}$ in the matrix element $\langle 11|\ldots|11\rangle$. Let us note here that, in the conformal case [14, 15], two copies of fused vertex operators of different chiralities are glued in a crossing invariant way to reconstruct operators with a trivial braiding, while the conjugation condition is satisfied automatically. In the off-critical case, the local operator is constructed from the product of vertex operator and its conjugate. The commutativity of such pairs follows from the commutativity of fused transfer matrices, while the conjugation condition is provided by choosing the symmetric (4) expressions $W_{1\mu}$. In that way, the normaliza-

tion of Boltzmann weights, as well as the gauge transform, is fixed in the local operators construction. Now, assuming the "conformal" normalization, which is natural in a scaling theory,

$$\lim_{\epsilon\to 0}\langle 11|\Phi_{1k}(0)\Phi_{1k}(u/\epsilon)|11\rangle = \frac{1}{(1-u)^{2\Delta_{1,k}}},$$

rather than the lattice one (8), and using Eq. (17), we find the following vacuum expectation values for scaling fields with the dimension Δ_{1k}:

$$\langle\hat{\Phi}_{1k}\rangle = (-1)^{k-1}(CM)^{2\Delta_{1k}}\lim_{\epsilon\to 0}Q_{k-1}(x^2)\sqrt{[k]}. \quad (25)$$

Here, the k-independent proportionality coefficient C between the mass of kink M [9] and the temperature parameter $\exp(-\pi^2/2\epsilon)$ can be fixed from $k = 3$ case due to [21]. Computing the limit (25), we arrive at the Lukyanov–Zamolodchikov answer for the vacuum expectation values of the scaling fields $\hat{\Phi}_{1k}$ in the conformal normalization [10, 22]

$$\langle\hat{\Phi}_{1k}\rangle = (-1)^{k-1}\left(M\frac{\sqrt{\pi}\Gamma\left(\frac{3}{2}+\frac{\xi}{2}\right)}{2\Gamma\left(\frac{\xi}{2}\right)}\right)^{2\Delta_{1\kappa}} \times Q(1-(k-1)\xi). \quad (26)$$

The meromorphic function $Q(x)$ obtained from (17) can be rewritten as an analytic continuation of

$$Q(x) = \exp\int_0^\infty\frac{dt}{t}\left\{\frac{\cosh 2t\sinh t(x-1)\sinh t(x+1)}{2\cosh t\sinh t\xi\sinh t(1+\xi)} - \frac{x^2-1}{2\xi(\xi+1)}e^{-4t}\right\}. \quad (27)$$

Finally, let us draw some concluding remarks. Our motivation for studying the fused vertex operators was that the integral representations for the correlation functions are rather difficult to analyze in the scaling limit. At the moment, we think that one of the most effective methods of studying correlation functions in the scaling theory [8, 9] is Al. Zamolodchikov's approach of combining results of the conformal perturbation and the form-factor theories. The most important objects in [11] are vacuum expectation values of local operators which determine normalizations of form factors as well as local OPEs. In the present paper, we started studying a lattice origin of the vacuum expectation values by introducing and analyzing algebra of spin operators for the ABF model. Tracing the result (25)–(27) back to Eq. (17), we observe that the essential part of the Lukyanov–Zamolodchikov vacuum expectation values, the function $g_\mu(\zeta)$, appears in the fused vertex operators theory as a part of the normalization multiple of the Boltzmann weight $\mathbf{W}_{\mu\mu}$. The last one, in turn, is related with Baxter's partition function of the eight vertex model [1]. We checked that this phenomenon is of a general nature. It appears, for instance, for vacuum expectation values of local operators of other integrable models, like Z_N models [23] and perturbed W_n models [24, 25]. In that way, the formulated procedure proposes an alternative way for finding vacuum expectation values in scaling models for which the lattice vertex operators are known, e.g., [26, 27]. The nice feature of the construction is that the "reflection equations" [22, 24, 28] are automatically taken into account. It would be very interesting to generalize the construction to descendant operators [18], for which, in general, the reflection equations [28] are difficult to solve, see, e.g., [29, 30].

This work was supported by the Russian Science Foundation, RFBR 02/01/01015, INTAS-03-51-3350. I am very grateful to V.A. Fateev and Al.B. Zamolodchikov for their hospitality at Montpellier University and to M. Kashiwara, T. Miwa, and M. Jimbo for their hospitality at Kyoto University at the "RIMS 2004" project, where part of the work was done. I also would like to thank S. Lukyanov and M. Lashkevich for useful discussions.

REFERENCES

1. R. J. Baxter, *Exactly Solved Models in Statistical Mechanics* (Academic, London, 1982; Mir, Moscow, 1985).
2. M. Jimbo and T. Miwa, *Algebraic Analysis of Solvable Lattice Models* (Am. Math. Soc., Providence, RI, 1994), CBMS Reg. Conf. Ser. Math., Vol. 85.
3. S. Lukyanov, Commun. Math. Phys. **167**, 183 (1995).
4. S. Lukyanov and Y. Pugai, JETP **82**, 1021 (1996).
5. S. Lukyanov and Y. Pugai, Nucl. Phys. B **473**, 631 (1996).
6. A. Kadeishvili, JETP Lett. **63**, 917 (1996).
7. G. Andrews, R. Baxter, and J. Forrester, J. Stat. Phys. **35**, 193 (1984).
8. A. B. Zamolodchikov, Adv. Stud. Pure Math. **19**, 641 (1989).
9. F. A. Smirnov, Nucl. Phys. B **337**, 156 (1990); A. LeClair, Phys. Lett. B **230**, 103 (1989).
10. S. L. Lukyanov and A. B. Zamolodchikov, Nucl. Phys. B **493**, 571 (1997).
11. Al. B. Zamolodchikov, Nucl. Phys. B **348**, 619 (1991).
12. E. Date, M. Jimbo, and M. Okado, Lett. Math. Phys. **12**, 209 (1986).
13. A. B. Belavin, A. M. Polyakov, and A. B. Zamolodchikov, Nucl. Phys. B **241**, 333 (1984).
14. V. Dotsenko and V. Fateev, Nucl. Phys. B **251**, 691 (1985).
15. G. Felder, Nucl. Phys. B **317**, 215 (1989); G. Felder, J. Frohlich, and G. Keller, Commun. Math. Phys. **124**, 647 (1989).
16. M. Jimbo, M. Lashkevich, T. Miwa, and Y. Pugai, Phys. Lett. A **229**, 285 (1997).
17. V. Tarasov and A. Varchenko, q-alg/9703044.

18. J. Shiraishi, H. Kubo, H. Awata, and S. Odake, Lett. Math. Phys. **38**, 33 (1996).
19. M. Lashkevich and Y. Pugai, Nucl. Phys. B **516**, 623 (1998).
20. M. Jimbo, H. Konno, S. Odake, *et al.*, J. Stat. Phys. **102**, 883 (2001).
21. Al. B. Zamolodchikov, Int. J. Mod. Phys. A **10**, 1125 (1995).
22. V. A. Fateev, S. L. Lukyanov, A. B. Zamolodchikov, and Al. B. Zamolodchikov, Nucl. Phys. B **516**, 652 (1998).
23. P. Baseilhac and V. A. Fateev, Nucl. Phys. B **532**, 567 (1998).
24. V. A. Fateev, Mod. Phys. Lett. A **15**, 259 (2000).
25. C. Ahn, V. A. Fateev, C. Kim, *et al.*, Nucl. Phys. B **565**, 611 (2000).
26. H. Konno, Commun. Math. Phys. **161**, 33 (1994).
27. M. Jimbo, H. Konno, S. Odake, and J. Shiraishi, Commun. Math. Phys. **199**, 605 (1999).
28. A. B. Zamolodchikov and Al. B. Zamolodchikov, Nucl. Phys. B **477**, 577 (1996).
29. D. Fradkin, V. Fateev, S. Lukyanov, *et al.*, hep-th/9807236.
30. P. Baseilhac and M. Stanishkov, hep-th/0104220; hep-th/0212342.

JETP Letters, Vol. 79, No. 10, 2004, pp. 464–467. From Pis'ma v Zhurnal Éksperimental'noĭ i Teoreticheskoĭ Fiziki, Vol. 79, No. 10, 2004, pp. 575–578.

Bloch Oscillations in a Homogeneous Nucleotide Chain¶

V. D. Lakhno and N. S. Fialko

Institute of Mathematical Problems of Biology, Russian Academy of Sciences, Pushchino, Moscow region, 142290 Russia
e-mail: lak@impb.psn.ru, fialka@impb.psn.ru

Received March 30, 2004

It is shown that, at zero temperature, a hole placed in a homogeneous synthetic nucleotide chain with applied electric field demonstrates Bloch oscillations. The oscillations of the hole placed initially on one of the base pairs arise in response to disruption of the initial charge distribution caused by nucleotide vibrations. The finite temperature fluctuations result in degradation of coherent oscillations. The maximum permissible temperature for DNA "Bloch oscillator" occurrence is estimated. © *2004 MAIK "Nauka/Interperiodica".*

PACS numbers: 87.14.Gg; 87.15.Aa; 82.39.Pj

In recent years, experiments on the study of the charge migration in DNA placed in external electric field have become feasible [1–3]. Of special interest for future nanotechnology are experiments with synthetic homogeneous nucleotide sequences [1]. The properties of electrons or holes in such nucleotide sequences should be similar to those of band charge carriers in crystals of the solid body.

As is known, in the case of ideal periodic crystal structure, an electron located therein exhibits oscillations [4]. In semiconductors with superlattices, this gives rise to such phenomena as radiation of electromagnetic waves (Bloch oscillator) [5], negative differential conductivity [6, 7], absolute negative conductivity [8], dynamical localization [9–13], and multiphoton absorption [14, 15].

One-dimensional and homogeneous "DNA crystal" differs significantly from its solid analogue, because oscillations of the nucleotide pairs play a great role there. Motion of the charge carriers in DNA is accompanied by considerable displacements of the nucleotide pairs from their equilibrium positions, which, in turn, affect the motion of the charge carriers.

Our purpose here is to report the results of charge transfer modeling: dynamical behavior of a hole in the DNA sequence of the form $(\mathbf{G}–\mathbf{C})_n$ (where **G** is guanine, **C** is cytosine) in electric field applied along the chain.

In such a chain, a hole travels over guanine bases whose oxidation potentials are lower than that of cytosine [16]. The Hamiltonian of the charge transfer along the chain of nucleotide sites has the form [17, 18]

$$H = H_h + T_K + U_P,$$

$$H_h = \sum_n \alpha_n a_n^+ a_n + \sum_{n,m} \nu_{n,m}(a_n^+ a_m + a_m^+ a_n), \quad (1)$$

$$\alpha_n = \alpha_n^0 + \alpha_n' u_n + n\hbar\omega_B,$$

$$T_K = \sum_n M_n \dot{u}_n^2/2, \quad U_P = \sum_n K_n u_n^2/2.$$

Here, H_h is the Hamiltonian of a hole; a_n^+, a_n are the operators of creation and annihilation of the hole at the nth site; and α_n is the energy of a hole at the nth site. $\hbar\omega_B = eEa$, where E is the intensity of the electric field, e is the electron charge, a is the distance between neighboring bases. $\nu_{n,m}$ is the matrix element of the transition from the nth site to the mth one. T_K is the kinetic energy of the sites, U_P is the potential energy of the sites (M_n is the mass of the nth site, u_n is the displacement of the nth site from its equilibrium position, and K_n is the elastic coefficient). α_n' is the hole-site displacement coupling constant, $n = 1, \ldots, N$, and N is the number of sites in the chain.

We choose the wave function of a hole $|\Psi\rangle$ in the form

$$|\Psi\rangle = \sum_{n=1}^{N} b_n |n\rangle,$$

where b_n is the amplitude of the probability of hole localization at the nth site, and then derive from Hamiltonian (1) in the nearest-neighbor approximation the following equations of motion [17, 18]:

$$i\hbar \frac{db_n}{dt} = \alpha_n b_n + \nu_{n,n+1} b_{n+1} + \nu_{n-1,n} b_{n-1}, \quad (2)$$

$$M_n \frac{d^2 u_n}{dt^2} = -K_n u_n - \gamma_n \frac{du_n}{dt} - \alpha_n' |b_n|^2. \quad (3)$$

¶ This article was submitted by the authors in English.

Equations (2) are the Schrödinger equations for the probability amplitudes. To take into account the processes of dissipation, in classical equations of motion (3), we added the term $-\gamma_n \dot{u}_n$ (γ_n are the friction coefficients). System (2), (3) corresponds to the case of the zero temperature $T = 0$.

In the absence of interaction between a hole and the displacements of the chain sites (at $\alpha_n' = 0$ for all n), Eqs. (2) have the solution [19, 20]

$$b_n(t) = \sum_{m=-\infty}^{\infty} b_m(0)(-i)^{n-m} e^{-i(n+m)\omega_B t/2} J_{n-m}(\xi(t)),$$
$$\xi(t) = \frac{4\nu}{\hbar\omega_B}\sin\left(\frac{\omega_B t}{2}\right), \quad (4)$$

where $\nu_{n,n\pm1} = \nu$ in the case of a homogeneous chain and J_n are Bessel functions of the first kind. Solution (4) corresponds to Bloch oscillations of a hole with frequency ω_B and the position expectation value of the hole center mass value $x(t) = \sum |b_n|^2 na$. By the use of (4), it can be expressed as

$$x(t) = x(0) + \frac{2a\nu}{\hbar\omega_B}|S_0|(\cos\Theta_0 - \cos(\omega_B t + \Theta_0)),$$
$$S_0 = \sum_{m=-\infty}^{\infty} b_m^*(0) b_{m-1}(0) = |S_0| e^{i\Theta_0}, \quad (5)$$
$$x(0) = a\sum_{m=-\infty}^{\infty} m|b_m(0)|^2.$$

Expression (5) corresponds exactly to the quasi-classical description of the charge migration in crystal lattice [4–15] if $b_m(0) \approx b_{m-1}(0)$, when $\Theta_0 = 0$ and $S_0 = 1$.

By (5), the amplitude of $x(t)$ oscillations is equal to zero if at the initial moment the charge was localized at just one site. In this case the density of the hole probability at each moment is distributed symmetrically about the initial position $x = 0$. Classically, a hole moves along the field and opposite it with acceleration identical in modulus and contrary in direction, deriving energy from the field when traveling along it and at the same time losing energy when moving in the opposite direction.

In contrast to $x(t)$, the mean square value of hole position $X^2(t) = \sum |b_n|^2 n^2 a^2$ other than zero and is equal to

$$X^2(t) = X^2(0) + \frac{a^2}{2}\left(\frac{4\nu}{\hbar\omega_B}\right)^2 \sin^2\frac{\omega_B t}{2},$$
$$X^2(0) = a^2\sum_{m=-\infty}^{\infty} m^2|b_m(0)|^2. \quad (6)$$

Thus, the motion of the charge density represents coherent oscillations with Bloch period.

In modeling the motion of a hole in the sequence **GG** … **G** with account of the site displacements, we took the same parameter values as in [17]: $\alpha_n^0 = 0$, $\omega^2\tau^2 = 0.0001$ (where $\omega_n^2 = K_n/M_n$), $\omega_n' = \tau\gamma_n/M_n = 0.006$, $\kappa = (\alpha_n')^2\tau/(\hbar K_n) = 4$; $\tau = 10^{-14}$ s, $M_n = 10^{-21}$ g. Matrix elements were taken from [21]: $\nu_{n,n\pm1} = 0.084$ eV.

Corresponding to (1), the dimensionless Cauchy system was numerically solved by the fourth order Runge-Kutta method. In the calculations, the normalizing condition was controlled; it was fulfilled with an accuracy of $|\sum |b_n|^2 - 1| < 0.0001$. The initial conditions for the displacements and site velocities were taken to be zero. At the initial moment, charge was assumed to be localized in the middle of the chain consisting of 499 sites (at the 250th site); i.e., we dealt with the case when, in a rigid lattice with $\alpha_n' = 0$, oscillations of the mass center of a hole are lacking. The initial conditions under discussion are typical since, in charge transfer experiments, a hole arises due to photoexcitation on one nucleotide pair [22–24]. We calculated the system with a number of electric field intensity values $\tilde{E} = eaE\tau/\hbar$.

Figure 1 shows the dependences of $x(t)$ for some values of the electric field intensity which varies from the minimum at which the effects concerned with the finiteness of the chain do not manifest themselves $E_{\min} = 8\nu/eaN$ to the maximum $E_{\max} = 4\nu/ea$, which corresponds to Stark localization of the hole at one site. Thus, taking into account interactions between the hole and the chain displacements u_n leads to the appearance of hole oscillations, the period T of which is quite close to $T_B = 2\pi/\omega_B$ (Fig. 2). Changes in the values of the friction coefficient γ and the constant α_n' influence the amplitude of the oscillations (vanishing at $\alpha_n' = 0$) but not their period. We relate this fact to violation of the initial charge distribution caused by displacements of sites from their equilibrium positions.

To explain the physical mechanism of the studied effect, let us consider an infinite nondeformable chain with $\alpha_n' = 0$. In this chain, a hole initially localized at the site with number $n = 0$ at the subsequent moments will produce symmetrical distributions of the charge density. The reason is that in this case the hole moves in antisymmetric potential α_n where it can transfer to the site n and to the site $-n$ with equal probability. If the interaction $\alpha_n' \neq 0$ takes place, symmetrical distribution of the charge density at the moment $t = 0$ will cause (in view of equation (3)) at the next moment displacements u_n, which are like-sign, and $u_n \approx u_{-n}$. So, the total poten-

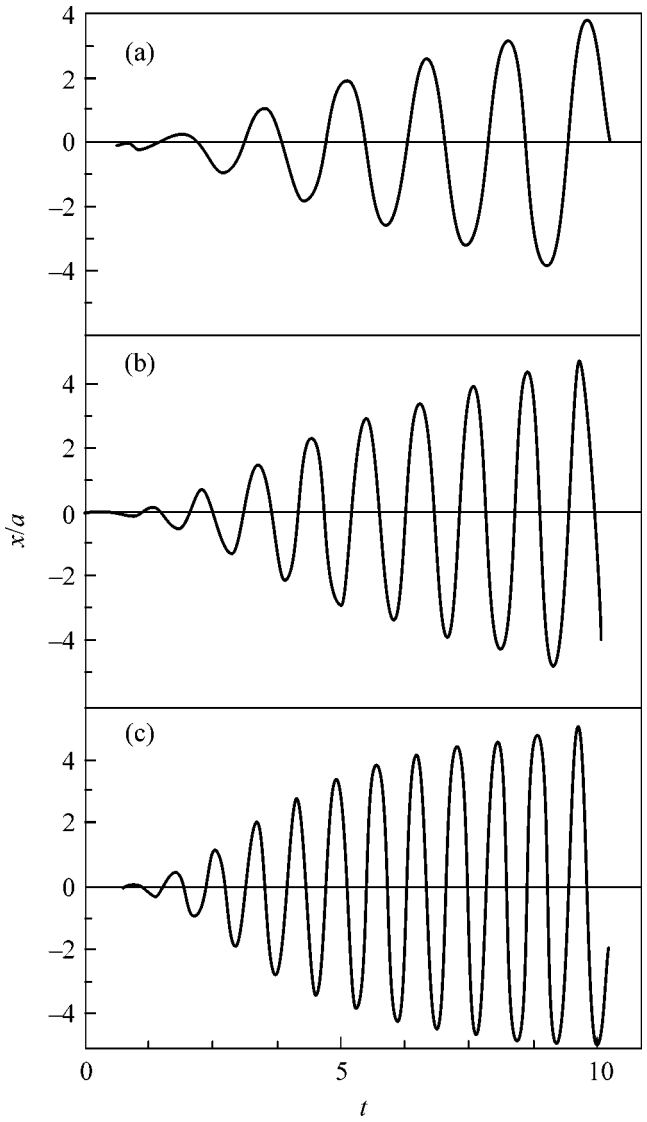

Fig. 1. Graphs of position expectation (normed to a), dependent on t (ps), for the next dimensionless values of the electric field intensity: (a) $\tilde{E}$ = 0.04, (b) $\tilde{E}$ = 0.06, and (c) $\tilde{E}$ = 0.08.

tial energy α_n, associated with the external electric field and site displacements, loses its symmetry. As a result, the probabilities of transitions along the electric field and in the opposite direction become different. This breaks the symmetry in the charge distribution and, consequently, causes nonzero displacement of the hole mass center $x(t)$. Classically, in this case (i.e., at $\alpha_n' \neq 0$), acceleration of the hole along the field is not equal in modulus to that opposite the field, and the energy which the hole derives from the field can radiate in the form of electromagnetic waves and oscillating quanta of the nucleotide chain. Note that the mechanism we deal with is general and is realized at any parameter values, with only quantitative characteristics of the effect varying.

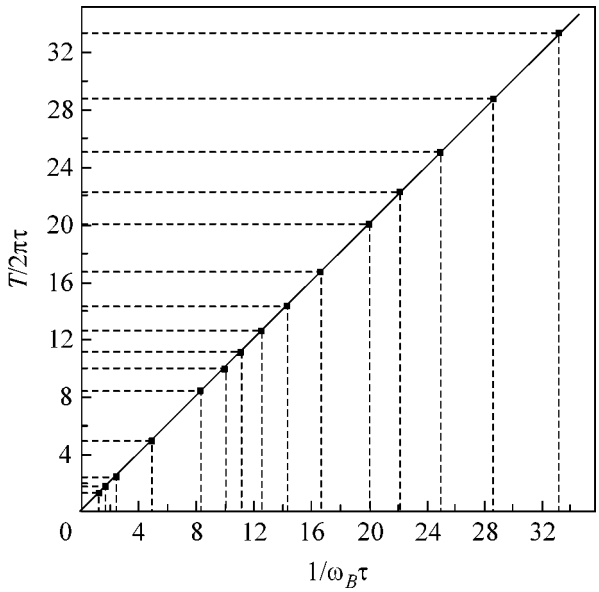

Fig. 2. Continuous line determines the Bloch oscillation T_B dependence on the electric field intensity E ($T_B = 2\pi/\omega_B$, $w_B = eEa/\hbar$ is the Bloch frequency) at $\kappa = 0$ (accordingly $\alpha_n' = 0$). The bold dots show periods calculated at $\kappa = 4$ ($\alpha_n' \sim 1.3 \times 10^{-4}$ eV/Å).

For the parameter values used, the value of the electric field intensity E lies in the range $E_{\min} \approx 4 \times 10^4$ V/cm $< E < 10^7$ V/cm $\approx E_{\max}$. These values of the field correspond to the frequencies of the electromagnetic waves Ω_n multiple of the Bloch frequency: $\Omega_n = n\omega_B$, n = 1, 2, …, with $\min\omega_B = 2 \times 10^{12}$ s^{-1} and $\max\omega_B = 5 \times 10^{14}$ s^{-1}. So, for actually attainable electric field intensities, the radiation frequencies fall in the terahertz range.

Until the present time, no experiments have been carried out on the observation of microwave radiation in nucleotide sequences.

Bloch oscillations are observed at finite temperature on the condition $\omega_B\tau > 1$, where τ is the time of the hole relaxation determined by dissipation on site oscillations. The value of τ can be estimated from the relation $\tau = \mu m^*/e$, where μ is the hole mobility and $m^* = \hbar^2/2va^2$ is the effective mass of hole. For our parameter values, the mass $m^* \approx 3.94m_0$ (m_0 is the electron mass).

In computations of the temperature dependence of the mobility μ, we used the method described in [25]. Classical equations for site motions obtained from (1) were modified so as to add the term $A_n(t)$ for taking into account the temperature fluctuations. So, the site

motions follows the Langevin equations. The mobility was calculated by the Kubo formula

$$\mu = \frac{e}{2T}\lim_{\varepsilon \to 0}\varepsilon^2\int_0^\infty \langle X^2(t)\rangle \exp(-\varepsilon t)dt, \qquad (7)$$

where $\langle X^2(t)\rangle$ is an averaged square of the hole displacement along a chain of sites for the temperature range from 10 to 350 K. For each given temperature, averaging was performed over a large number of realizations; then, the mean square displacement of a hole was found, from which the mobility was calculated by (7). The best approximation of the results obtained is given by the function

$$\mu \approx \mu_0 (T/T_0)^{-2.3}, \qquad (8)$$

where $\mu_0 \approx 2.87$ cm^2/V s (the improved value of [25]) is the mobility at $T = 300$ K.

Increase in the hole mobility with decreasing temperature given by dependence (8) can be explained as follows. As a result of temperature fluctuations, at each moment of time, a hole travels in a random potential field determined by random distribution of the hole energy on the sites α_i (1). Since, in the one-dimensional case considered, in a random field there always exists a localized state, increase in the mobility will always occur with decreasing amplitude of the random field. According to (1), this will take place as the contribution of $\alpha' u_i$ into the energy of a hole on the ith site decreases, i.e., the temperature falls.

With the use of the temperature dependence of the mobility (8) in the chain, one can estimate the temperature T at which Bloch oscillations take place at a frequency of ω_B: $T < (\omega_B \tau_0)^{1/2.3} T_0$, $\tau_0 \sim 6.4 \times 10^{-15}$ s being the relaxation time at $T_0 = 300$ K; e.g., at $\min \omega_B = 2 \times 10^{12}$ s^{-1}, the expression for the temperature value at which Bloch oscillations can be observed is $T < 45$ K.

This work was carried out with the support from the Russian Foundation for Basic Research, grant nos. 03-04-49225 and 04-07-90402.

REFERENCES

1. D. Porath, A. Bezryadin, S. de Vries, and C. Dekker, Nature **403**, 635 (2000).
2. H.-W. Fink and C. Schönenberger, Nature **398**, 407 (1999).
3. P. Tan, B. Alavi, and G. Gruner, Phys. Rev. Lett. **85**, 1564 (2000).
4. N. W. Ashcroft and N. D. Mermin, *Solid State Physics* (Holt-Saunders, Philadelphia, 1981).
5. E. E. Mendez and G. Bastard, Phys. Today **46** (6), 34 (1993).
6. L. Esaki and R. Tsu, IBM J. Res. Dev. **14**, 61 (1970).
7. R. Tsu and G. H. Döhler, Phys. Rev. B **12**, 680 (1975).
8. B. J. Keay, S. Zenner, S. J. Allen, *et al.*, Phys. Rev. Lett. **75**, 4102 (1995).
9. K. Unterrainer, B. J. Keay, M. C. Wanke, *et al.*, Phys. Rev. Lett. **76**, 2973 (1996).
10. D. H. Dunlap and V. M. Kenkre, Phys. Lett. A **127**, 438 (1988).
11. M. H. Shon and H. N. Nazareno, J. Phys.: Condens. Matter **4**, L611 (1992).
12. X. G. Zhao, Phys. Lett. A **167**, 291 (1992).
13. M. Holthaus, G. H. Ristow, and D. W. Hone, Europhys. Lett. **32**, 241 (1995).
14. B. S. Monozon, J. L. Dunn, and C. A. Bates, Phys. Rev. B **50**, 17 097 (1994).
15. B. S. Monozon, J. L. Dunn, and C. A. Bates, J. Phys.: Condens. Matter **8**, 877 (1996).
16. E. D. Lewis and Y. Wu, J. Photochem. Photobiol. **2**, 1 (2001).
17. N. S. Fialko and V. D. Lakhno, Phys. Lett. A **278**, 108 (2000).
18. V. D. Lakhno and N. S. Fialko, Regul. Chaotic Dyn. **7**, 299 (2002).
19. A. M. Bouchard and M. Luban, Phys. Rev. B **52**, 5105 (1995).
20. M. Luban, J. Math. Phys. **26**, 2386 (1985).
21. A. A. Voityuk, N. Rösch, M. Bixon, and J. Jortner, J. Phys. Chem. **104**, 9740 (2000).
22. S. Wessely and B. Giese, J. Biomol. Struct. Dyn., Spec. Issue 2, 293 (2000).
23. E. Meggers, M. E. Michel-Beyerle, and B. Giese, J. Am. Chem. Soc. **120**, 12950 (1998).
24. B. Giese and A. Billand, Chem. Commun. **7**, 667 (2002).
25. V. D. Lakhno and N. S. Fialko, JETP Lett. **78**, 336 (2003).

JETP Letters, Vol. 79, No. 10, 2004, pp. 468–472. Translated from Pis'ma v Zhurnal Éksperimental'noĭ i Teoreticheskoĭ Fiziki, Vol. 79, No. 10, 2004, pp. 579–584.

Short-Range Order and Twins in Ordered Titanium Monoxide

A. A. Valeeva and A. I. Gusev*

Institute of Solid-State Chemistry, Ural Division, Russian Academy of Sciences, ul. Pervomaĭskaya 91, Yekaterinburg, 620219 Russia

**e-mail: gusev@ihim.uran.ru*

Received April 5, 2004

The structure of annealed titanium monoxide $TiO_{1.087}$ containing monoclinic ordered phase Ti_5O_5 was studied by electron diffraction. Along with the set of structural, superstructural, and extra reflections, the diffraction pattern of titanium monoxide shows a set of plane diffuse fringes in the $(112)^*_{B1}$ section of the reciprocal lattice of the basis cubic structure *B*1. It is shown that some of the extra reflections are due to the twinning of the monoclinic superstructure along the (–1–11) plane of the reciprocal lattice of the basis cubic structure. The diffuse contours enclose plane areas of the reciprocal space with the fixed values of wave vectors $\mathbf{K}_{100} \sim \pm(h + 0.07)\mathbf{k}_{100}$, $\mathbf{K}_{010} \sim \pm(k + 0.07)\mathbf{k}_{010}$, and $\mathbf{K}_{001} \sim \pm(l + 0.07)\mathbf{k}_{001}$ of the *B*1 structure. Their appearance is associated with the short-range displacement order. © *2004 MAIK "Nauka/Interperiodica".*

PACS numbers: 61.66.Fn; 61.14.Hg

Titanium monoxide TiO_y ($0.8 < y < 1.25$) belongs to the group of strongly nonstoichiometric interstitial compounds [1] and is characterized by an unusual structure containing a large number of structural vacancies (unoccupied lattice sites) simultaneously in the nonmetallic and metallic sublattices. A disordered TiO_y monoxide has the *B*1 structure and, depending on the oxygen content, behaves either as an electronic conductor or as a narrow-gap semiconductor [2, 3]. The monoclinic (space group *C*2/*m*) Ti_5O_5 phase (or $Ti_5{\blacksquare}O_5{\square}$, where ■ and □ are the structural vacancies in the metallic and nonmetallic sublattices, respectively) is the main ordered phase of titanium monoxide [4]. The structural features of the Ti_5O_5 phase are as yet not completely understood. In this work, the short-range displacement order in this ordered phase was observed and analyzed by electron diffraction, and the twin reflections from the ordered phase were set off from the observed extra reflections and quantitatively identified.

A sample of $TiO_{1.087}$ monoxide was prepared by high-temperature vacuum synthesis from Ti and TiO_2 powders. To obtain disordered distribution of structural vacancies, the synthesized sample was quenched from 1330 to 283 K at a rate of 200 K s^{-1}. The measured density (4.968 g cm^{-3}) proved to be 20% lower than the theoretical density (5.962 g cm^{-3}) calculated on the assumption that the metallic sublattice is defectless. The comparison of the measured and theoretical densities gives the formula $Ti_{0.833}O_{0.906}$. This signifies that 0.167th of all titanium sublattice sites and 0.094th of all oxygen sublattice sites are vacant.

The ordered titanium monoxide was prepared by annealing the quenched sample at 1330 K for 3 h followed by slow cooling to 300 K at a rate of 10 K h^{-1}. The synthesis method and conditions and the procedure of certifying the samples of nonstoichiometric disordered and ordered titanium monoxide over the entire range of existence of the cubic phase are described in detail in [5]. X-ray diffraction of the annealed titanium monoxide suggested that, along with the monoclinic (space group *C*2/*m*) ordered phase of the Ti_5O_5 type, the synthesized sample contained about 30% of a disordered titanium monoxide. In addition, the X-ray diffraction pattern shows in the range of angles $2\theta < 36°$ several lines whose intensities are from two to three times lower than the intensity of the superstructural reflections from the Ti_5O_5 phase. These lines are part of a set of superstructural reflections observed in the X-ray pattern of the annealed $TiO_{1.262}$ monoxide. Although we failed to determine the structure of the ordered phase of annealed $TiO_{1.262}$ monoxide, we established that the observed diffraction reflections did not correspond to the known tetragonal $Ti_4{\blacksquare}O_5$ [6, 7] and rhombic $Ti_5{\blacksquare}O_6$ [6] and $Ti_2{\blacksquare}O_3$ [8] phases of the cubic titanium monoxide.

Electron diffraction and the microstructure of the ordered titanium monoxide were observed using a Philips CM-200 electron microscope with a beam width of 70 nm and wavelength $\lambda = 0.00251$ nm. The procedure of sample preparation was described in [9]. The microdiffraction angle relative to the high-atomic-resolution images was zero. The aperture included structural spots $[111]^*_{B1}$ and $[220]^*_{B1}$. The bright-field image was photographed in the central $[000]^*_{B1}$ spot, and the dark-field image, in the $[111]^*_{B1}$ reflection. The instrument constant was $L\lambda = 2.33 \sim 2.51$ mm nm, where *L* is the chamber length.

0021-3640/04/7910-0468$26.00

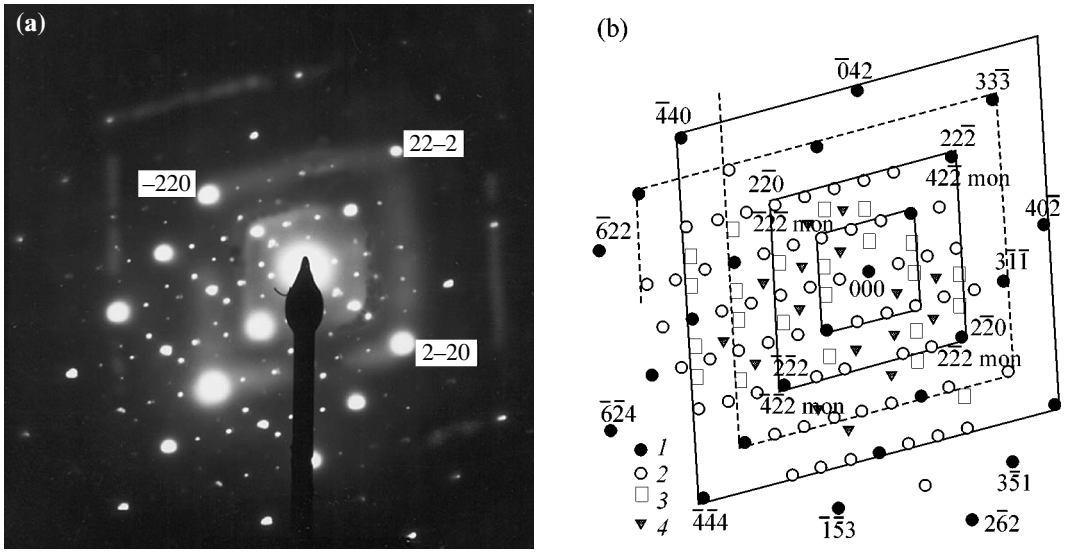

Fig. 1. (a) Experimental diffraction pattern of the ordered monoclinic (space group $C2/m$) titanium monoxide $TiO_{1.087}$ and (b) the scheme of the diffraction pattern: (*1*) structural reflections of the basis cubic lattice $B1$ of a disordered titanium monoxide; (*2*) superstructural reflections of the ordered monoclinic Ti_5O_5 phase; (*3*) twin reflections of the ordered monoclinic Ti_5O_5 phase; (*4*) unidentified reflections possibly belonging to the unknown ordered phase; diffuse fringes parallel to the $[02-1]^*_{B1}$ and $[20-1]^*_{B1}$ directions are shown by the solid lines (weak fringes are shown by dashes). Matrix axis $[112]^*_{B1} \equiv [011]^*_{C2/m}$. For convenience, indices of some structural and superstructural reflections are shown.

In [9–11], apart from the structural and superstructural reflections, extra reflections were observed in the diffraction pattern of the ordered monoclinic (space group $C2/m$) titanium monoxide Ti_5O_5. The authors of [9, 11] assumed that these were the twin reflections but did not identify them. In this work, the observed reflections are identified quantitatively.

Figure 1a displays the electron diffraction pattern of the ordered monoclinic (space group $C2/m$) $TiO_{1.087}$ monoxide, where the extra reflections are seen most clearly. The normal to the figure plane coincides with the matrix axis and corresponds to the $[011]^*_{C2/m} \equiv [112]^*_{B1}$ direction in the reciprocal lattice. The diffraction pattern contains vast and diverse information: in addition to 124 spots of different intensity, it exhibits a system of weak diffuse fringes parallel to the $[02-1]^*_{B1}$ and $[20-1]^*_{B1}$ directions and slightly shifted from the structural sites. None of the fringes passes through the $[000]^*_{B1}$ site. Apart from the structural reflections (28 high-intensity spots), less intense superstructural reflections and extra reflections, which can be associated with the presence of twins in the sample, are seen. In the case of a double diffraction, the secondary twin reflections can be observed in addition to the primary ones. The microphotographs obtained by transmission electron microscopy provide strong evidence for the presence of twins in the sample studied. In particular, five twins in the form of extended rectangles are clearly seen in Fig. 2. Let us first discriminate

Fig. 2. TEM microphotographs of the $TiO_{1.087}$ sample (115000x magnification). The extended rectangles are twins; the angle of the twin with broad extinction contours (on the right and slightly above the middle of the figure) is large (~90°), and the remaining twins with narrow extinction contours belong to the second family.

between the structural, superstructural, and extra reflections. For the convenience of analysis, the observed diffraction pattern is schematically shown in Fig. 1b.

The distances R_{hkl} from the central $[000]^*_{B1}$ spot to the nearest structural $[hkl]^*_{B1}$ spots situated at an angle of 90° with respect to the central spot are equal to 9.75 and 15.90 nm. Note that the ratio of the distances to the nearest structural reflections situated in the perpendicular directions [–110] and [11–1] is equal to ~1.63 ≅ $(2\sqrt{2})/\sqrt{3}$, i.e., corresponds to the ratio typical for the (112) section of the reciprocal FCC lattice. This is an additional evidence that the observed diffraction pattern corresponds to this plane of the reciprocal lattice. The values of 0.238 ± 0.012 and 0.147 ± 0.007 nm calculated for the interplanar spacings $d_{hkl} = L\lambda/R_{hkl}$ using the instrument constant $L\lambda = 2.33 \sim 2.51$ mm nm correspond to the $[11-1]^*_{B1}$ and $[-220]^*_{B1}$ reflections of the basis cubic phase. The calculated positions of the superstructural reflections in the section containing the indicated basis-phase reflections allowed the former to be assigned to the superstructural spots $[21-1]^*_{C2/m}$ and $[-22-2]^*_{C2/m}$, respectively. For a better understanding, the indices of some of the observed structural and superstructural reflections are shown in the diffraction pattern in Fig. 1b. It became clear from our analysis that, in addition to 28 structural reflections, 57 superstructural reflections are present in the diffraction pattern.

Whereas the structural reflections of the basis $B1$ phase were rather easily distinguished from the superstructure reflections of the monoclinic phase, the remaining 39 extra reflections were identified only after special calculations. In so doing, the TEM results were taken into account (Fig. 2). Judging from the extinction contours in the photographs, there are two twin families. The twin situated on the right slightly above the middle of Fig. 2 and fringed with broad contour lines belongs to the first family, and the remaining twins belong to the second family. The twins are turned relative to each other by an angle of ~67°–68°. For the twinning along the (111) planes in the FCC crystals, such an angle (~67.8°) can be observed if the matrix axis is directed along [112] [12]. The most probable reason for the occurrence of the extinction contour is that the twinning plane forms a certain angle with the surface of the sample (foil). The twinning angle φ is defined as the angle between the matrix axis [112] and the normal to the twinning plane: φ ≈ 19.5° for the twinning plane (111), φ ≈ 61.9° for the planes (–111) and (1–11), and φ = 90° for the (–1–11) plane. The extinction contours of a twin belonging to the first family are rather broad, so that the corresponding twinning angle is close to 90°. With this preliminary estimate in mind, one can believe that the twinning most likely occurs along the (–1–11) plane.

It is clear from the diffraction pattern (Fig. 1) that the extra reflections cannot be assigned to the primary twin reflections from the basis cubic phase, because, upon twinning in an FCC crystal along any plane belonging to the (111) family, all twin reflections in the (112) section of reciprocal lattice should coincide with certain structural reflections. Since no such coincidence is observed in our case, the extra twin reflections are associated with the ordered monoclinic phase.

To index the twin reflections, the indices of all reflections were represented in the cubic coordinates. For the twinning along the $(p_1p_2p_3)$ plane, the corresponding twin indices $(h^*_{tw1}\ h^*_{tw2}\ h^*_{tw3})$ are related to the matrix indices $(h_1^*\ h_2^*\ h_3^*)$ by the formula

$$h^*_{twi} = \frac{p_i\left[\left(2\sum_{i=1}^{3} p_i h_i^*\right) - p_i h_i^*\right] - h_i^*\left[\left(\sum_{i=1}^{3} p_i^2\right) - p_i^2\right]}{\sum_{i=1}^{3} p_i^2}, \quad (1)$$

where the notation $h_1^* \equiv h^*_{cub}$, $h_2^* \equiv k^*_{cub}$, and $h_3^* \equiv l^*_{cub}$ is introduced for brevity. Note that Eq. (1) is invariant about the transposition of h^*_{twi} and h_i^* and can be used to determine the twin reflection indices for the given matrix reflections or the matrix reflection indices for the assumed twin reflections. Passing from the found cubic to the monoclinic indices in the reciprocal lattice is described by the following relationships: $h^*_{mon} = h^*_{cub} - l^*_{cub}$, $k^*_{mon} = k^*_{cub}$, and $l^*_{mon} = h^*_{cub} + 2l^*_{cub}$ (similar relationships between the monoclinic and cubic coordinates in the direct lattice of the ordered Ti_5O_5 phase have the form $h_{mon} = (2h_{cub} - l_{cub})/3$, $k_{mon} = k_{cub}$, and $l_{mon} = (h_{cub} + l_{cub})/3$).

In the above calculation, the possibility of twinning along any of the (111), (–111), (1–11), and (–1–11) planes of the reciprocal lattice of a crystal with $B1$ structure was taken into account. The calculation showed that 23 of the 39 observed extra reflections were primary twin reflections of the ordered monoclinic Ti_5O_5 phase, with twinning along the (–1–11) plane; there is no secondary twinning. Sixteen unidentified extra reflections (Fig. 1b) belong, most likely, to the ordered phase that as yet has not been identified on the basis of the available experimental data.

In the diffraction pattern (Fig. 1a), the diffuse scattering is observed in the form of a system of low-intensity plane diffuse fringes parallel to the [02–1] and [20–1] directions and shifted from the structural sites in the ±[–15–2] and ±[5–1–2] directions, respectively. Let us express the displacement δ of the diffuse fringes through the absolute value of the $[100]^*_{B1}$ vector of reciprocal lattice. In the $(112)^*_{B1}$ plane, the diffuse

fringes form a system of geometrically similar and completely or partially closed rhombic contours concentrically arranged about the primary [000] spot. If the fringes passed through the structural sites (including the forbidden sites of the type [–110], [1–10], etc.), the ratio D/d of the major to minor rhombus diagonals would be equal to $\sqrt{3}/\sqrt{2}$ for any rhombus. The same ratio of $(3/2)^{1/2}$ is retained if the displacements in the ±[100], [010], and ±[001] directions of the reciprocal lattice are the same. If the displacement is nonzero only in the ±[001] direction, then $D/d > (3/2)^{1/2}$ and the diagonals of the diffuse contour coincide with the [11–1] and [1–10] directions. If the fringes are shifted only in the ±[100] and ±[010] directions, the ratio $D/d < (3/2)^{1/2}$; if the shifts are identical, the minor diagonal of the diffuse contour coincides with the [1–10] direction. If the diffuse fringes are shifted only in the ±[100] or ±[010] direction, the diagonals of the diffuse contour do not coincide with the [11–1] and [1–10] directions, and $D/d \neq (3/2)^{1/2}$. In the case considered, the ratio of the diagonals of the observed diffuse contours is $\sim(3/2)^{1/2}$, indicating that their diagonals coincide with the [11–1] and [1–10] directions. This signifies that the diffuse contour nearest to the [000] site in a three-dimensional reciprocal lattice is shaped like a cube with faces formed by the diffuse planes and shifted from this site by same value $\delta_{100,\,010,\,001} = \Delta|\mathbf{k}_{100,\,010,\,001}|$ in the ±[100], ±[010], and ±[001] directions ($\mathbf{k}_{100}$ = [100], $\mathbf{k}_{010}$ = [010], $\mathbf{k}_{001}$ = [001], and $|\mathbf{k}_{100}| = |\mathbf{k}_{010}| = |\mathbf{k}_{001}|$). The numerical processing of the diffraction pattern (Fig. 1a) showed that the relative displacement Δ is equal to ~0.07. Therefore, the positions of the plane diffuse areas in the reciprocal space can be specified by the vectors $\mathbf{K}_{100} = \pm(\mathbf{k}_{h00} + \Delta\mathbf{k}_{100}) = \pm(h + \Delta)\mathbf{k}_{100}$, $\mathbf{K}_{010} = \pm(\mathbf{k}_{0k0} + \Delta\mathbf{k}_{010}) = \pm(k + \Delta)\mathbf{k}_{010}$, and $\mathbf{K}_{001} = \pm(\mathbf{k}_{00l} + 0.07\mathbf{k}_{001}) = \pm(l + \Delta)\mathbf{k}_{001}$ normal to the corresponding diffuse planes.

According to [13], the periodic diffuse features bypassing the reciprocal lattice sites of the basis cubic phase can be assigned to the short-range substitution order. However, the observed diffuse scattering is different from the one typical of the majority of nonstoichiometric carbides and nitrides MX_y ($MX_y\square_{1-y}$) with short-range substitution order in the distribution of nonmetallic atoms X and structural vacancies □. For instance, diffuse scattering typical of the short-range substitution order and different from the above diffraction pattern was observed in [14], where the disordered cubic titanium monoxides $TiO_{1.00}$, $TiO_{1.19}$, and $TiO_{1.25}$ were studied by electron diffraction. The only common feature is that plane diffuse fringes parallel to the [110] direction are present in the diffraction pattern corresponding to the (110) section of the reciprocal lattice of the $TiO_{1.00}$ sample. However, these features are local rather than extended; moreover, from the comparison of the analogous diffraction patterns of $TiO_{1.25}$ and $TiO_{1.19}$ it becomes clear that the local plane diffuse features are degenerate spherical effects. The authors of [14] assumed that titanium monoxide has a high electronic conductivity and, by analogy with metallic alloys, explained the diffuse scattering by the appearance of concentration or displacement waves with the wave vectors corresponding to the flat or cylindrical areas of the Fermi surface. However, the assumption about the high electronic conductivity is contradictory to the experiment: the bremsstrahlung spectra [15] and the optical conductivity data [16] suggest that the energy gap in the disordered TiO_y is nonzero. The presence of a gap between the O(2*p*) and Ti(3*d*) bands in the electronic spectrum of TiO_y is confirmed by the calculations in [17]. According to [2, 3], the disordered TiO_y monoxides are narrow-gap semiconductors with a gap up to 0.17 eV at $y > 1.08$ and are poor electronic conductors only at $y < 1.07$.

In nonstoichiometric MX_y compounds with the basis structure *B*1, the diffuse scattering in the presence of short-range substitution order can be described using the approximate cluster transition-state model [18–23]. By the transition state is meant crystal state at a temperature slightly above the order–disorder transition, i.e., the state with short-range order and yet without long-range order in the atomic arrangement. In this model, the diffuse scattering distribution in the reciprocal lattice is described using cubic, octahedral, or tetrahedral clusters (or their combination) with all or part of their cites occupied by the atoms X. In the simplest case, the diffuse-scattering surface for the octahedral cluster is described by the expression [18, 23] $\cos(\pi h) + \cos(\pi k) + \cos(\pi l) = 0$, and the analogous expression in a more accurate model [23] has the form $\cos(\pi h) + \cos(\pi k) + \cos(\pi l) + \gamma\cos(\pi h)\cos(\pi k)\cos(\pi l) = 0$, where γ is a certain constant depending on the composition of the compound. The spatial distribution of the diffuse scattering observed in [14] for the disordered TiO_y was also described using the transition-state model with a tetrahedron-shaped cluster. For the interval $1.05 \le y \le 1.25$ of TiO_y compositions, this was done by the authors of [21]. In the case of the tetrahedral cluster, the diffuse-scattering surface is described by the equation $f(\mathbf{g})f^*(\mathbf{g}) - \mu = 0$, where $f(\mathbf{g}) = 1 + \exp[i\pi(h + k)] + \exp[i\pi(h + l)] + \exp[i\pi(k + l)]$ and μ is a parameter close to unity.

Our calculation showed that none of the three models listed above can provide the diffuse-scattering contours that we observed in the diffraction pattern for the (112) section of the reciprocal FCC lattice. However, diffuse scattering caused by the short-range substitution order is usually observed for the samples of nonstoichiometric compounds quenched from a temperature slightly above the order–disorder transition. In other words, such a diffuse scattering is typical of the transition state [19–22] and, as the transition to the ordered state occurs, the diffuse-scattering intensity is gradually concentrated at the positions corresponding to the superstructural reflections. Since in our case the diffraction pattern was obtained for the ordered titanium

monoxide, the diffuse scattering from the short-range substitution order is absent. In accordance with the theory of diffraction in imperfect crystals [24], the plane diffuse-scattering regions can be caused by the atomic-displacement waves. One can thus assume that the displacement waves in the ordered $TiO_{1.087}$ monoxide enclose plane areas of reciprocal space with the fixed wave vectors $\mathbf{K}_{100} \sim \pm(h + 0.07)\mathbf{k}_{100}$, $\mathbf{K}_{010} \sim \pm(k + 0.07)\mathbf{k}_{010}$, and $\mathbf{K}_{001} \sim \pm(l + 0.07)\mathbf{k}_{001}$. The diffuse scattering caused by the short-range displacement order has maximal intensity just near these vectors. Therefore, the results obtained in this work allow one to assume that the formation of monoclinic Ti_5O_5 superstructure in the nonstoichiometric cubic titanium monoxide $TiO_{1.087}$ is accompanied not only by the rearrangement of atoms and structural vacancies but also by the formation of atomic-displacement waves.

We are grateful to guest Prof. Guoyi Tang (Institut fur Theoretische und Angewandte Physik, Universitat Stuttgart, Germany), Prof. A.A. Rempel (Institute of Solid-State Chemistry, Ural Division, Russian Academy of Sciences, Russia), Dr. F. Phillipp, and Ms. M. Kelsch (Max-Planck-Institut fur Metallforschung, Stuttgart, Germany) for assistance in the experiment. This work was supported by the Russian Foundation for Basic Research (project nos. 03-03-32031a and 03-03-32033a).

REFERENCES

1. A. I. Gusev, A. A. Rempel, and A. A. Magerl, *Disorder and Order in Strongly Non-Stoichiometric Compounds. Transition Metal Carbides, Nitrides and Oxides* (Springer, Berlin, 2001).
2. A. A. Valeeva, A. A. Rempel', and A. I. Gusev, Pis'ma Zh. Éksp. Teor. Fiz. **73**, 702 (2001) [JETP Lett. **73**, 621 (2001)].
3. A. I. Gusev and A. A. Valeeva, Fiz. Tverd. Tela (St. Petersburg) **45**, 1185 (2003) [Phys. Solid State **45**, 1242 (2003)].
4. A. A. Valeeva, A. A. Rempel', and A. I. Gusev, Pis'ma Zh. Éksp. Teor. Fiz. **71**, 675 (2000) [JETP Lett. **71**, 460 (2000)].
5. A. A. Valeeva, A. A. Rempel', and A. I. Gusev, Neorg. Mater. **37**, 716 (2001).
6. E. Hilti, Naturwissenschaften **55**, 130 (1968).
7. D. Watanabe, O. Terasaki, A. Jostsons, and J. R. Castles, in *The Chemistry of Extended Defects in Non-Metallic Solids*, Ed. by L. Eyring and M. O. Keeffe (North-Holland, Amsterdam, 1970), pp. 238–258.
8. A. I. Gusev, Pis'ma Zh. Éksp. Teor. Fiz. **74**, 96 (2001) [JETP Lett. **74**, 91 (2001)].
9. A. A. Valeeva, A. A. Rempel, M. A. Müller, *et al.*, Phys. Status Solidi B **224**, R1 (2001).
10. A. A. Valeeva, G. Tang, A. I. Gusev, and A. A. Rempel', Fiz. Tverd. Tela (St. Petersburg) **45**, 84 (2003) [Phys. Solid State **45**, 87 (2003)].
11. A. A. Valeeva, G. Tang, A. I. Gusev, and A. A. Rempel', Pis'ma Zh. Éksp. Teor. Fiz. **77**, 28 (2003) [JETP Lett. **77**, 25 (2003)].
12. L. M. Utevskiĭ, *Diffraction Electron Microscopy in Physical Metallurgy* (Metallurgiya, Moscow, 1973) [in Russian].
13. J. M. Cowley, *Diffraction Physics*, 3rd ed. (North-Holland, Amsterdam, 1995; Mir, Moscow, 1979).
14. J. R. Castles, J. M. Cowley, and A. E. C. Spargo, Acta Crystallogr. A **27**, 376 (1971).
15. S. R. Barman and D. D. Sarma, Phys. Rev. B **49**, 16141 (1994).
16. S. Gokhale, S. R. Barman, and D. D. Sarma, Phys. Rev. B **52**, 14526 (1995).
17. C. Leung, M. Weinert, P. B. Allen, and R. M. Wentzcovitch, Phys. Rev. B **54**, 7857 (1996).
18. J. Billingham, P. S. Bell, and M. H. Lewis, Acta Crystallogr. A **28**, 602 (1972).
19. R. de Ridder, G. van Tendeloo, and S. Amelinckx, Acta Crystallogr. A **32**, 216 (1977).
20. R. de Ridder, G. van Tendeloo, D. van Dyck, and S. Amelinckx, Phys. Status Solidi A **38**, 663 (1976).
21. R. de Ridder, D. van Dyck, G. van Tendeloo, and S. Amelinckx, Phys. Status Solidi A **40**, 669 (1977).
22. R. de Ridder, in *Diffraction and Imaging Techniques in Material Science*, Ed. by S. Amelinckx, R. Gevers, and J. von Landuyt, 2nd ed. (North-Holland, Amsterdam, 1978), pp. 429–453.
23. M. Sauvage and E. Parthe, Acta Crystallogr. A **28**, 607 (1972).
24. A. Guinier, *X-ray Diffraction in Crystals, Imperfect Crystals, and Amorphous Bodies* (Dover, New York, 1994).

Translated by V. Sakun

JETP Letters, Vol. 79, No. 10, 2004, pp. 473–478. Translated from Pis'ma v Zhurnal Éksperimental'noĭ i Teoreticheskoĭ Fiziki, Vol. 79, No. 10, 2004, pp. 585–591.

Structural Properties of the Condensate in Two-Dimensional Mesoscopic Systems of Strongly Correlated Excitons

Yu. E. Lozovik[1, *], S. Yu. Volkov[1], and M. Willander[2]

[1] *Institute of Spectroscopy, Russian Academy of Sciences, Troitsk, Moscow region, 142092 Russia*

** e-mail: lozovik@isan.troitsk.ru*

[2] *Chalmers Institute of Technology, Göteborg University, Göteborg, Sweden*

Received April 5, 2003

A two-dimensional mesoscopic Bose system of dipoles in a 2D trap is considered using computer simulation by the quantum path-integral Monte Carlo method. The model describes a rarefied system of spatially indirect excitons in a confining potential. Bose condensation in the system and its superfluid and structural properties are studied over a wide range of interparticle spatial correlations, from an almost ideal Bose gas to the regime of a strongly correlated system. It is found that, at strong interparticle spatial correlations, particles in the condensate form a crystal-like structure. In this case, the spatial correlations of particles in the condensate are less pronounced than the correlations of noncondensed particles. The effect of recurrent crystallization is observed in the regime of strong interparticle correlations. © *2004 MAIK "Nauka/Interperiodica".*

PACS numbers: 03.75.Hh; 68.65.-k; 03.75.Kk

1. INTRODUCTION

Bose condensation has long been a subject of only theoretical considerations; however, recent advances in the development of experimental techniques has allowed this phenomenon to be investigated in various systems [1–3]. In particular, of special interest is an examination of the possibility of Bose condensation in systems with reduced dimensionality [4, 5].

Along with atoms in traps, the system of spatially separated electrons and holes residing in coupled quantum wells, whose coherent properties were predicted in [6], is one of the most interesting physical systems for an experimental investigation of the Bose condensation effect. At present, this system is being intensively studied experimentally [4, 5], and the Bose condensation of indirect excitons in coupled quantum wells has recently been detected in [4, 5].

At low temperatures, electrons and holes from different wells form a coupled state representing a spatially indirect (interwell) exciton. In the ground state, this exciton possesses an electric dipole $d_{\mathrm{dip}} = eD$, where D is the distance between the quantum wells and a is the exciton radius along the quantum wells. At moderate exciton concentrations ($na^2 < 1$), the exchange effects are exponentially suppressed because of the barrier associated with the dipole–dipole repulsion, and, with a high accuracy, indirect excitons can be considered Bose particles. If the distance between excitons along the quantum wells is larger than the effective exciton size (characteristic size of the bound state [6]), the exciton can be considered a structureless Bose particle. Thus, the problem of N dipolar Bose particles in a two-dimensional harmonic confining potential with a frequency ω can be taken as a model of the system under consideration [7–9]. The number of excitons in a trap with a size of order 1 μm and an exciton density of 10^{10} cm^{-2} (which corresponds to the conditions of experiments in [4]) equals 100; that is, the system is mesoscopic in some sense.

In this connection, of great interest is the consideration of mesoscopic systems of particles, which demonstrate profound differences in the phase diagram as compared to extended systems [6, 16]. In the mesoscopic system of dipoles considered in this work, the mesoscopic size effect in the system becomes highly important in the region of strong correlations. In this case, the Bose-condensation critical temperature and, hence, the amount of condensate decrease with increasing number of particles, because it is known that the condensate in a system with interparticle interaction is absent in the thermodynamic limit at a nonzero temperature [26, 27]. The influence of interaction on the critical temperature in the region of strong correlations is stronger than the influence of the finite particle-number effect.

Another interesting implementation of the model of dipole particles in a confining potential is a two-dimensional trap for Bose atoms with a dipole moment induced by a static electric field or an electromagnetic field with a frequency resonant with the intraatomic transitions.

Of great interest is the study of the Bose condensation and other properties of such a system of dipole excitons, in particular, in the as yet unstudied region of strong interparticle correlations. Of special interest are the structural properties of the system, in particular, the

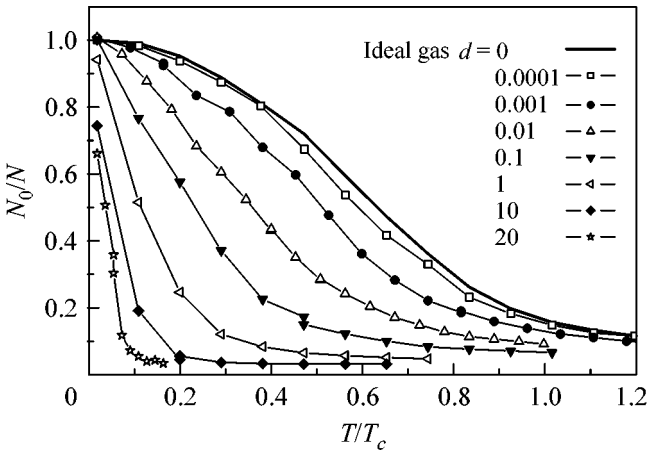

Fig. 1. Fraction of condensate particles as a function of temperature for various values of the dimensionless parameter d.

spatial structure of the Bose condensate. Another interesting challenge is the problem of a supersolid, that is, the possibility for a Bose system to simultaneously have spatial interparticle crystal-like order and superfluid properties.

The structural properties of a Bose system and condensate were considered by a number of authors, although only for a weak interparticle interaction (see, for example, [3, 7, 19–23]). In the cited works, the radial distributions of particles in the system (and in the condensate) remained monotonic functions in the region of parameters under consideration. However, we found in this work (see below) that in mesoscopic clusters these distributions become nonmonotonic in the region of stronger correlations and assume the form typical of crystal-like (shell) order.

We found that the condensate in a trap has a crystal-like structure (mesoscopic supersolid arises). In addition, recurrent crystallization was observed in the system under consideration.

2. MODEL

We consider this problem using the quantum path-integral Monte Carlo method [13].

The Hamiltonian of the model system has the form

$$H = \sum_i^N \left(-\frac{\hbar^2}{2m_{\text{eff}}} \nabla_i^2 + \frac{m_{\text{eff}}\omega^2}{2} r_i^2 \right) + \sum_{i<j}^N \frac{d_{\text{dip}}^2}{r_{ij}^3},$$

where m_{eff} is the effective mass of the indirect exciton. The second term in the Hamiltonian describes the confining potential for excitons. It can be associated with either the confining potential in an artificial semiconductor quantum dot or the nonuniform electric field generated by a metal electrode or the random potential relief in a system of coupled quantum wells.

Passing in the Hamiltonian to the dimensionless length $r_0 = \sqrt{\hbar/m_{\text{eff}}\omega}$ and energy $E_0 = \hbar\omega$, we obtain

$$H = \sum_i^N \left(-\frac{1}{2}\nabla_i^2 + \frac{1}{2} r_i^2 \right) + \sum_{i<j}^N \frac{d}{r_{ij}^3},$$

where we introduced the dimensionless quantum control parameter $d = d_{\text{dip}}^2 / E_0 r_0^3$, which serves as a dimensionless exciton-interaction constant. This parameter can be varied experimentally by changing the boson dipole moment, that is, the distance between the wells in the case of indirect excitons, or by varying the confining potential parameter. The other control parameters are the number of particles N and the dimensionless temperature $T/\hbar\omega$.

We assume that the condition for the applicability of our model is fulfilled, i.e., that the mean interparticle distance is considerably larger than the exciton size $n^{-1/2} \gg a_{\text{exc}}$.

3. RESULTS OF SIMULATION AND DISCUSSION

The mesoscopic system of quantum dipoles in a harmonic confining potential is studied using the quantum path-integral Monte Carlo method [13]. The study is carried out over a wide range of the values of dimensionless control parameter d, temperatures, and the number of particles in the system. Of special interest is the study of the Bose condensation and superfluidity phenomena in the given system in the regime of strong spatial correlations and the determination of the critical phase-transition temperatures as functions of the control parameters of the problem. We consider the temperature dependences of the energy and the fractions of the condensate and superfluid component for various values of d. The structural properties of the system and its structural transformations are studied by considering the total radial and shell-by-shell angular distributions of particles in the system, as well as the total and angular shell-by-shell pair distributions determining interparticle correlations. The condensate structure is studied using the same distribution functions for the condensate particles. Of special interest is the study of these functions in the region of strong interparticle correlations. Another quantity that reveals structural transformations is the Lindemann parameter (see, for example, [16]).

At small values of the parameter d, the system is close to an ideal gas in a trap, and the calculated values only slightly differ from the corresponding values for the ideal gas (see Figs. 1, 2) and agree well with the results of works devoted to a weakly nonideal Bose gas (see, for example, [3] and references therein).

To study the mechanism of washing-out condensate through the interparticle interactions, we examined the temperature dependences of the fractions of condensate

particles and superfluid component for different values of the interaction parameter d. For small values of the parameter d, these dependences have the same form as in an ideal gas (for the fraction of condensate $N_0/N = 1 - (T/T^0_{\text{bec}})^2$); however, the interaction gives a small correction to the critical temperature (Figs. 1, 3). At large values of the control parameter d, not only the value of the critical temperature changes but also the temperature dependence of the fraction of condensate changes, and now this fraction rapidly drops with increasing temperature.

At large values of the parameter d, strong interparticle correlations are observed in the system; they show up in the specific shell structure of the particle distribution in the system (Figs. 2, 4, 5). As a result of these correlations, the properties of the system in this regime strongly differ from the properties of a nonideal gas in the trap. In particular, a number of interesting new effects arise: the formation of crystal-like (shell) structure in the condensate and in the entire system, the recurrent crystallization, and the presence of a boundary around the particle cloud.

It is known that the dipolar systems of classical particles have a distinct shell structure at low temperatures [8]. However, quantum systems undergo quantum melting at a sufficiently low temperature, so that the crystal-like structure is smeared because of quantum fluctuations [8, 16]. On the other hand, a quantum system at high temperatures is close in its properties to a classical one. Hence, the crystal structure, if any, must undergo "classical" melting and smear with an increase in the number of equilibrium phonons. We found that, starting at certain values of d (see Fig. 6), a crystal-like structure exists in an intermediate temperature region; that is, recurrent crystallization occurs (this phenomenon was not observed for an extended two-dimensional system; see [12]). To analyze this problem, we considered a system of 40 particles with $d = 50$ (the fraction of condensate $n_0 = 0.24$ at $T = 0.1$) (Fig. 4). At the temperature $T = 0.1$, the structure is slightly smeared. However, as the temperature increases, the angular and radial distributions become more distinct (a process inverse to quantum melting—recurrent crystallization—occurs). As the temperature further increases, this structure is smeared again. The behavior of the Lindemann parameter U_r as a function of temperature reveals this effect rather distinctly (Fig. 7). Starting at a certain value of d, U_r varies nonmonotonically with temperature; namely, a minimum occurs (see Fig. 7), and it may be stated that the system is best ordered at the minimum of this parameter (only in a limited region of d values). This effect is also evident in the total distribution of particles in the system; it is observed only for sufficiently large values of the parameter d, i.e., in the regime of very strong interparticle correlations. It is worthy of note that the fractions of condensate and superfluid component are not equal to zero even in a system with clearly defined shell structure (Fig. 5).

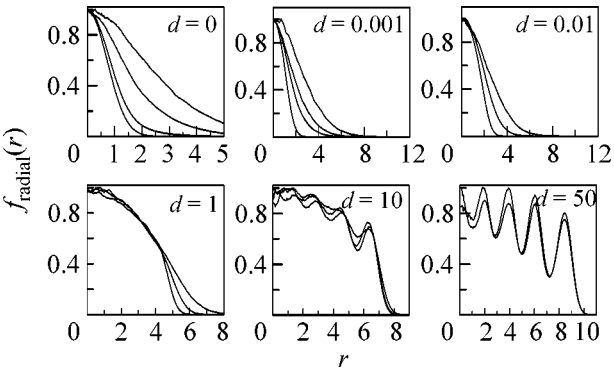

Fig. 2. Evolution of the total radial distributions with temperature for various values of d.

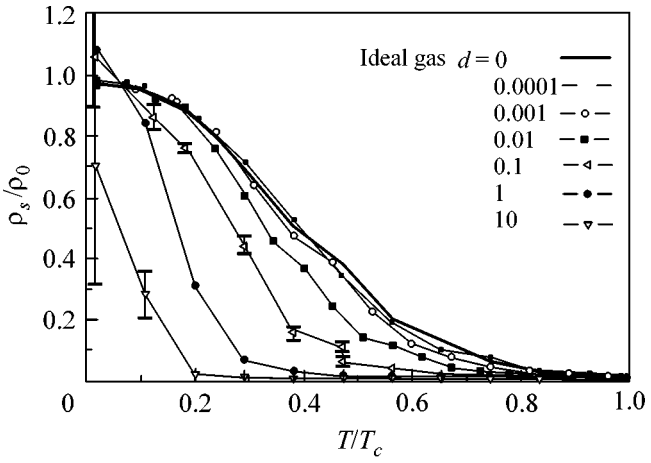

Fig. 3. Fraction of superfluid component as a function of temperature for various values of the dimensionless parameter d.

In connection with the study of the system structure, of interest is the following question: how is the condensate structured spatially? To examine this problem, we calculated the particle radial distributions in the condensate (Figs. 8, 9). Interestingly, this distribution becomes narrower with increasing temperature, and its maximum is located at the center of the system. In addition, the radial distribution of the condensate shows an extended tail. The point is that the condensate particles are mainly located at the center of the system. The temperature excitations begin to wash out the condensate, starting at its surface. Thus, it proves that the system as a whole has the following structure: a condensate core is at the center, and a shell of noncondensed particles is on the outside. The core decreases in size as the temperature increases.

For an ideal Bose gas, the shape of the condensate wave function does not depend on temperature. For a weakly nonideal gas, the condensate wave function in the trap is modified due to the interaction: it broadens

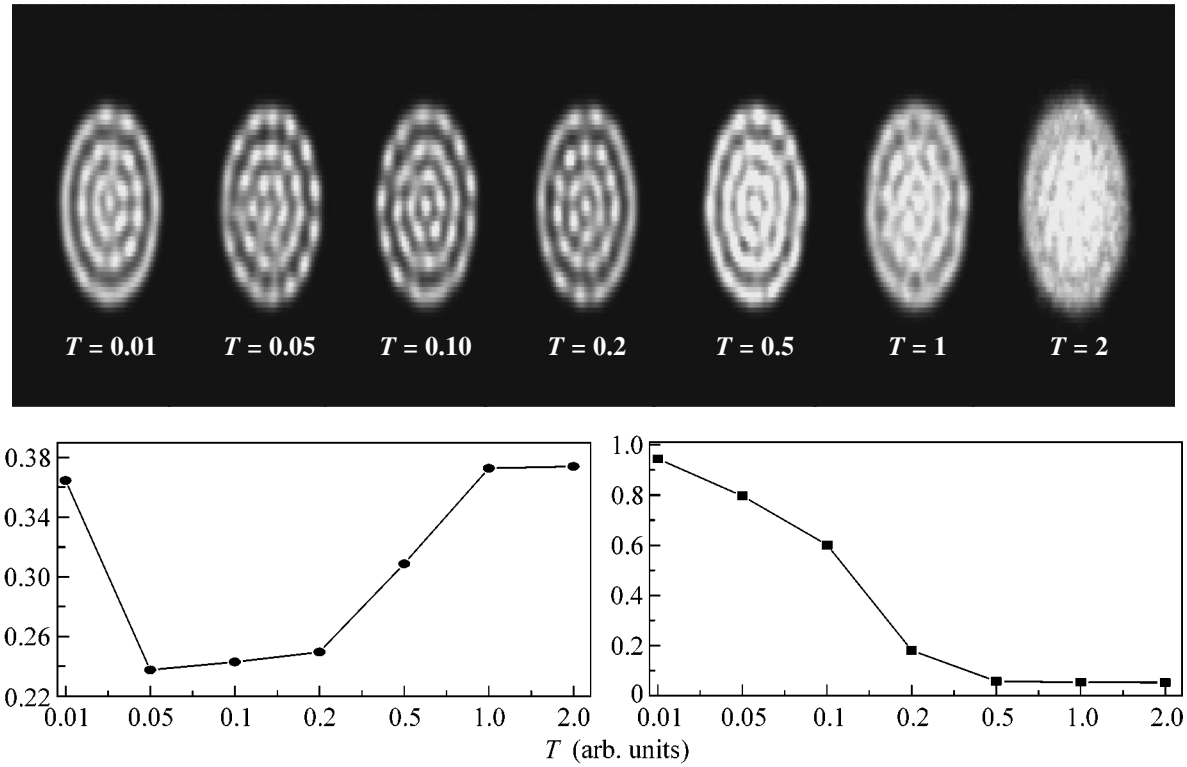

Fig. 4. Distributions of particles in the system, the Lindemann parameter, and the fraction of condensate at various temperatures.

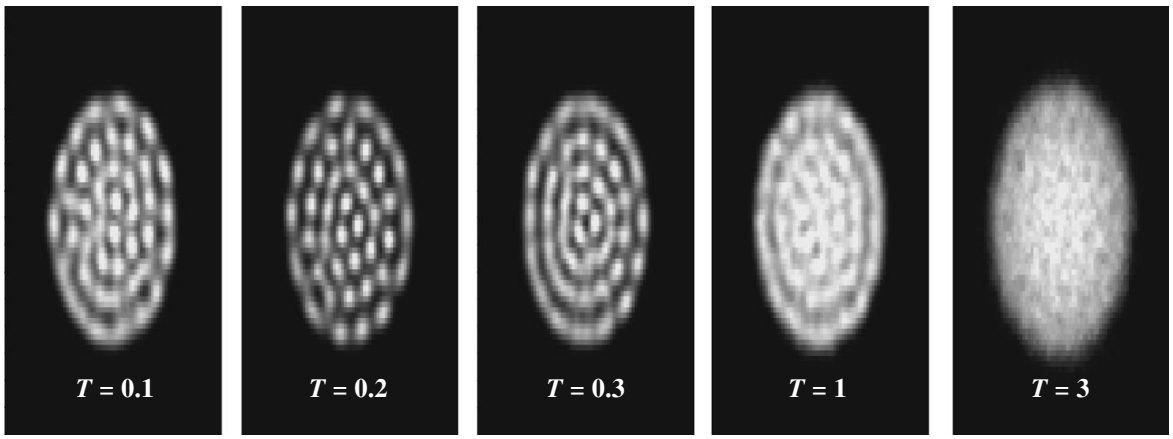

Fig. 5. Distributions of particles in the system.

(retaining the form ~exp(–$(r/\sigma)^2$)), in good agreement with the results reported in [3]. In this case, the wave function does not depend on temperature. As the magnitude of correlations (parameter *d)* increases, the function changes from Gaussian to ~$A - (r/\sigma')^2$ (Thomas–Fermi regime; see [3]). We found that, as the parameter *d* further increases, the distribution of condensate particles in the region of strong spatial correlations (though sufficiently weak for the condensate to appear in the system) displaces an interesting phenomenon: a nonmonotonic distribution is seen against the background of the dependence ~$A - (r/\sigma')^2$. Hence, it turns out that the distribution, on the whole, nonmonotonically depends on the radius (see Figs. 8, 9) and has a shell structure that repeats (at a low temperature) the distribution of all particles of the system but is less pro-

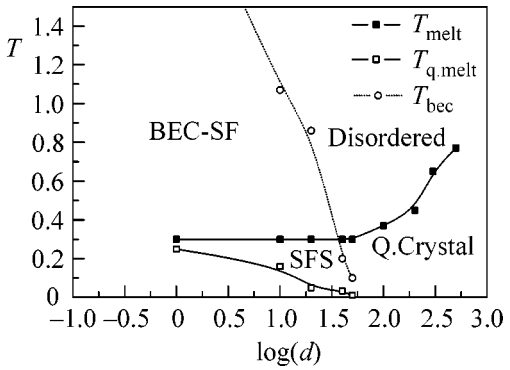

Fig. 6. Phase diagram of the system. Region Q.Crystal is the domain of existence of quantum crystal, $T_{melt}(d)$ is the melting curve of the quantum crystal upon an increase in temperature, $T_{q.melt}(d)$ is the melting curve of the quantum crystal due to zero-point quantum vibrations, and the BEC-SF region is the domain of existence of the Bose condensate and the superfluid component in the system.

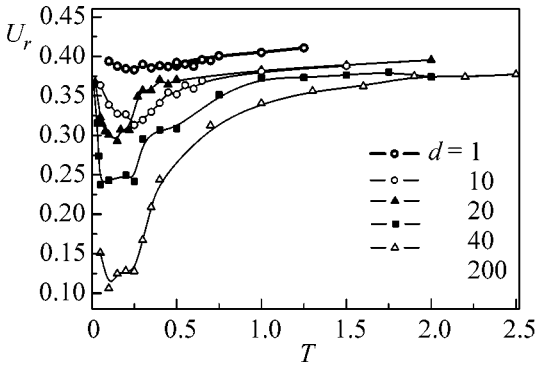

Fig. 7. Lindemann parameter as a function of temperature. The sharp growth of the parameter points to melting in the system.

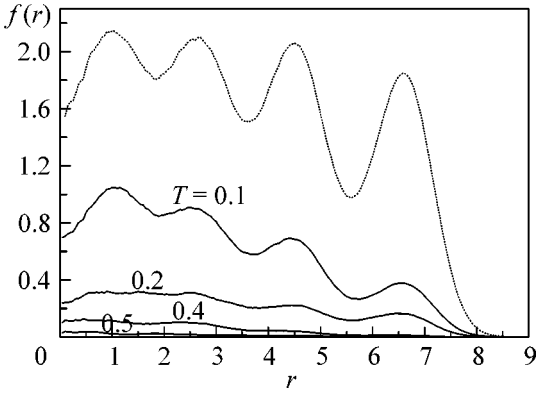

Fig. 8. Radial distributions of particles in the condensate at various temperatures. Dotted line designates the total radial distribution in the system. From top to bottom: radial distributions of condensate particles with decreasing temperature.

nounced than in the case of noncondensed particles (see Fig. 9). As the condensate is washed out with increasing temperature, the spatial correlations in the condensate become weaker (see Fig. 8). Of special interest is the fact that the spatial interparticle correlations of condensate particles are less pronounced than the correlations of the noncondensed particles.

Thus, the system exhibits simultaneously both diagonal and nondiagonal order; i.e., this state can be considered a mesoscopic supersolid. This is a mesoscopic effect, because our calculations show that, as the total number of particles in the system increases (for fixed temperature and interaction strength), the fraction of condensate decreases (in the thermodynamic limit, a two-dimensional system with interparticle interaction does not have condensate at a nonzero temperature; see [26]).

The distributions of the condensate particles in systems of 40 and 30 particles are shown in Figs. 4 and 5, respectively, for the values $d = 50$ and 40, respectively. At the temperature $T = 0.1$, the structure formed by the condensate particles is slightly smeared as compared to the total structure of the system. As the temperature increases, the condensate is depleted and the condensate structure smears (melts).

Let us discuss the phase diagram of the system; see Fig. 6. In a certain region (Q.Crystal in Fig. 6), spatial ordering of particles (quantum crystal) occurs in the system. In this case, $T_{melt}(d)$ is the classical melting curve of the system upon an increase in the temperature and $T_{q.melt}(d)$ is the quantum melting curve of the crystal (e.g., due to zero-point quantum vibrations). In the region *BEC-SF*, the system contains the Bose condensate and the superfluid component. Let us summarize the main results of this work. (1) In the region of strong spatial correlations, the condensate particles in a mesoscopic system form a crystal-like structure. In this case, the particle correlations in the condensate are less pronounced than the correlations of all particles. As the temperature increases, the decay of this structure occurs earlier than the complete melting of the entire system. The spatial shell structure of the distribution might reveal itself in the ring pattern of the interwell exciton photoluminescence. (2) At certain intermediate values of the dimensionless control quantum parameter

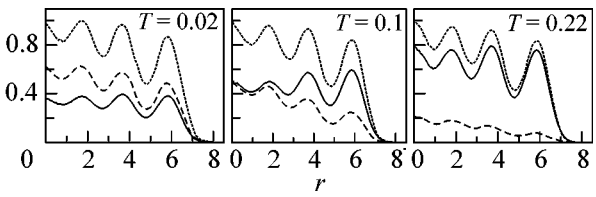

Fig. 9. Radial distributions of particles in the condensate at various temperatures for $N = 30$ and $d = 20$; dashed line corresponds to particles in the condensate, solid line corresponds to noncondensed particles, and dotted line corresponds to all particles.

d, the recurrent-crystallization effect is observed: at low temperatures, the crystal order is absent in the system because of quantum fluctuations; next, with increasing temperature, a crystal-like structure forms in the system. This structure melts in a classical way as the temperature further increases.

This work was supported by the Russian Foundation for Basic Research, INTAS, and the Ministry of Education. S.Yu. Volkov is grateful for support to the Dinastiya foundation and the International Center for Fundamental Physics in Moscow (ICFPM).

Yu.E.L. is grateful to L.V. Keldysh, V.D. Kulakovskiĭ, and V.B. Timofeev for useful discussions of the results.

REFERENCES

1. M. H. Anderson and J. R. Ensher, Science **269**, 198 (1995); J. R. Ensher, D. S. Jin, M. R. Matthews, *et al.*, Phys. Rev. Lett. **77**, 4984 (1996).
2. W. Ketterle and N. J. Druten, Phys. Rev. A **54**, 656 (1996).
3. F. Dalfovo, S. Giorgini, and L. P. Pitaevskii, Rev. Mod. Phys. **71**, 463 (1999).
4. A. V. Larionov, V. B. Timofeev, P. A. Ni, *et al.*, Pis'ma Zh. Éksp. Teor. Fiz. **75**, 699 (2002) [JETP Lett. **75**, 570 (2002)]; A. V. Larionov, V. B. Timofeev, J. M. Hvam, *et al.*, JETP Lett. **75**, 200 (2002); JETP **90**, 1093 (2000).
5. L. V. Butov, Solid State Commun. **127**, 89 (2003).
6. Yu. E. Lozovik and O. L. Berman, JETP Lett. **64**, 573 (1996); Yu. E. Lozovik and V. I. Yudson, Sov. Phys. JETP **44**, 389 (1976); Yu. E. Lozovik and V. A. Mandelshtam, Phys. Lett. A **165**, 469 (1992).
7. W. Krauth, Phys. Rev. Lett. **77**, 3695 (1996).
8. Yu. E. Lozovik, S. A. Verzakov, and M. Willander, Phys. Lett. A **260**, 400 (1999); A. I. Belousov and Yu. E. Lozovik, JETP Lett. **68**, 858 (1998).
9. L. Santos, G. V. Shlyapnikov, P. Zoller, *et al.*, Phys. Rev. Lett. **85**, 1791 (2000); V. V. Konotop and V. M. Prez-Garcia, cond-mat/0106488 (2001); S. Giovanazzi, A. Gorlitz, and T. Pfau, cond-mat/0204352 (2002); K. Bernardet, G. G. Batrouni, J.-L. Meunier, *et al.*, cond-mat/0110314 (2001).
10. S. De Palo, F. Rapisarda, and G. Senatore, cond-mat/0201414 (2002).
11. S. A. Moskalenko and D. W. Snoke, *Bose–Einstein Condensation of Excitons and Biexcitons and Coherent Nonlinear Optics with Excitons* (Cambridge Univ. Press, New York, 2000); V. V. Krivolapchuk, E. S. Moskalenko, and A. L. Zhmodikov, Phys. Rev. B **64**, 045313 (2001).
12. Yu. E. Lozovik and V. M. Farztdinov, Solid State Commun. **54**, 725 (1985).
13. D. M. Ceperley and E. L. Pollock, Phys. Rev. B **39**, 2084 (1989).
14. D. M. Ceperley, Rev. Mod. Phys. **67**, 279 (1995).
15. S. Heinrichs and W. J. Mullin, cond-mat/9807331 (1998).
16. A. V. Filinov, M. Bonitz, and Yu. E. Lozovik, Phys. Rev. Lett. **86**, 3851 (2001).
17. M. Bayindir and B. Tanatar, Phys. Rev. A **58**, 3134 (1998).
18. G. Schmid, S. Todo, M. Troyer, and A. Dorneich, cond-mat/0110024 (2001).
19. G. E. Astrakharchik and S. Giorgini, cond-mat/0212512 (2002).
20. M. Holzmann and Y. Castin, physics/9812029 (1998).
21. T. D. Lee, K. Huang, and C. N. Yang, Phys. Rev. **106**, 1135 (1957).
22. F. Dalfovo and S. Stringari, Phys. Rev. A **53**, 2477 (1996).
23. K. Goral and L. Santos, Phys. Rev. A **66**, 023613 (2002); K. Goral, K. Rzazewski, and T. Pfau, Phys. Rev. A **61**, 051601 (2000).
24. Yu. Kagan, V. A. Kashurnikov, A. V. Krasavin, *et al.*, cond-mat/9811090 (1998).
25. D. S. Fisher and P. C. Hohenberg, Phys. Rev. B **37**, 4936 (1988).
26. W. J. Mullin, J. Low Temp. Phys. **106**, 615 (1997); Phys. Rev. B **33**, 4632 (1986).
27. W. J. Mullin, cond-mat/9610005 (1996); W. J. Mullin, cond-mat/9709077 (1996).
28. J. Shumway and D. M. Ceperley, cond-mat/9909434 (1999).
29. W. Deng and P. M. Hui, cond-mat/9704095 (1997).
30. S. Grossmann and M. Holthaus, Phys. Lett. A **208**, 188 (1995).

Translated by A. Bagatur'yants

JETP Letters, Vol. 79, No. 10, 2004, pp. 479–483. Translated from Pis'ma v Zhurnal Éksperimental'noĭ i Teoreticheskoĭ Fiziki, Vol. 79, No. 10, 2004, pp. 592–596.

Energy Distributions of Photoelectrons Emitted from *p*-GaN(Cs, O) with Effective Negative Electron Affinity

A. A. Pakhnevich[1, 2], V. V. Bakin[1], A. V. Yaz'kov[2], G. É. Shaĭbler[1], S. V. Shevelev[1], O. E. Tereshchenko[1, 2], A. S. Yaroshevich[1], and A. S. Terekhov[1, 2]

[1] *Institute of Semiconductor Physics, Siberian Division, Russian Academy of Sciences, pr. Akademika Lavrent'eva 13, Novosibirsk, 630090 Russia*

[2] *Novosibirsk State University, ul. Pirogova 2, Novosibirsk, 630090 Russia*

Received April 5, 2004

Energy distributions of photoelectrons emitted into vacuum from the valence band and the localized states in the energy gap of *p*-GaN(Cs, O) with effective negative electron affinity were studied. It is shown that the photothermal electron excitation from the localized states lying below the Fermi level in the energy gap of *p*-GaN(Cs, O) is the dominant photoemission mechanism at the low-energy photoemission threshold. © *2004 MAIK "Nauka/Interperiodica".*

PACS numbers: 79.60.Bm

Interest in high-energy-gap Group III nitrides is due to their successful use in the fabrication of light sources emitting in the blue–green and ultraviolet (UV) spectral regions, high-power high-temperature microwave devices, and UV photodetectors. Vacuum photomultipliers and electrooptical converters possess the highest detection ability and operation speed and allow the detection of single photons. The fabrication of perfect GaN-based photocathodes with effective negative electron affinity (ENEA) and their use in UV photodetectors would be helpful in solving important scientific and practical problems. The basic possibility of devising ENEA emitters on the basis of *p*-GaN(Cs, O) was demonstrated in [1]. The study is underway on the atomic and electronic structures of atomically pure GaN surfaces and their modification upon cesium and oxygen adsorption [2, 3]. Nevertheless, the energy distributions of electrons emitted from *p*-GaN(Cs, O) have not been studied so far. These distributions carry important information about the types of optical transitions responsible for photoemission, about the kinetic phenomena involving the thermalized and hot nonequilibrium electrons, and about the electron–phonon interaction in semiconductors. In particular, the electron-distribution energy width measured for the phonon energy $\hbar\omega \simeq \varepsilon_g$ coincides, to a high accuracy, with the ENEA. The latter is commonly symbolized by χ^* and is one of the most important characteristics of the *p*-GaN(Cs, O) surface. The values of χ^* measured to date by different authors [3, 4] differ from each other within a factor of 3, and the reasons for this disagreement remain to be understood.

In this work, the energy distributions measured for the *p*- GaN(Cs, O) surface with ENEA were used to discriminate between the photoemission transitions from the valence band and the energy-gap localized states, with the aim of revealing the photothermal photoemission mechanism at the long-wavelength photoemission threshold and establishing the possible reason for the scatter of the χ^* values obtained by different authors.

Magnesium-doped *p*-GaN layers grown from MOS hydride epitaxy on a (0001)-oriented leucosapphire substrate were used in the experiments. The free-hole concentration measured using the Hall effect at room temperature was 1×10^{17} cm^{-3}. The atomically pure *p*-GaN surface was prepared by the technique that was successfully used in the operation with GaAs [5]. It included the following steps: gallium oxides were chemically removed from the GaN surface by processing it with a solution of HCl in isopropyl alcohol in a pure nitrogen atmosphere [6]; after processing, the heterostructure was mounted on a vacuum-degassed molybdenum holder, placed in a hermetic transport container with the N_2 atmosphere, and carried either into a vacuum chamber of an ADES-500 electron spectrometer for determining the chemical composition and atomic structure of the surface by the methods of X-ray photoelectron spectroscopy (XPS) and low-energy electron diffraction or into a three-chamber ultravacuum setup for heat cleaning, applying cesium and oxygen, and installing into vacuum photodiodes. The photodiodes were used for measuring the quantum-efficiency spectra $QE(\hbar\omega)$ of the *p*-GaN(Cs, O) photocathodes and the $N_e(\varepsilon_\parallel)$ distributions of the emitted electrons in the longitudinal energy $\varepsilon_\parallel$.

0021-3640/04/7910-0479$26.00 © 2004 MAIK "Nauka/Interperiodica"

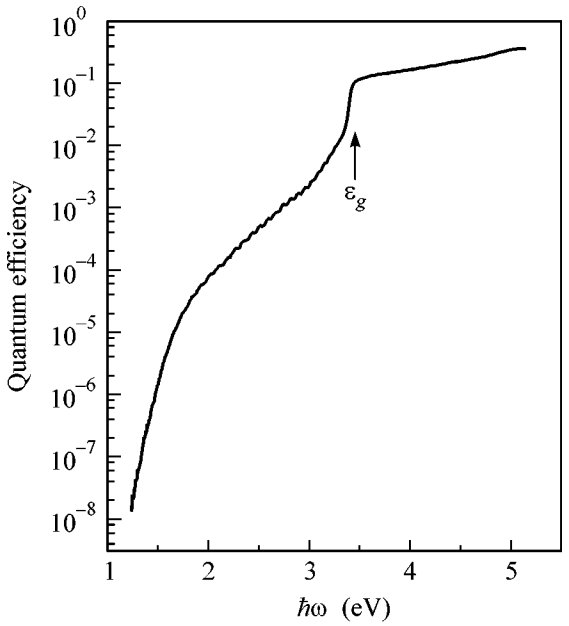

Fig. 1. Spectral dependence of the quantum efficiency of *p*-GaN(Cs, O) photoemitter.

The photodiode consisted of a cylindrical frame made from alumina-based ceramics and having a leucosapphire window and a *p*-GaN(Cs, O) photocathode of diameter 18 mm on a molybdenum holder, both hermetically fixed at the opposite ends of the cylinder. A planar copper grating with a diameter of 18 mm, mesh size of 15 × 15 μm, and effective transparency of 0.44 was placed between the window and the photocathode. The separation between the grating and the photocathode was ~1 mm to eliminate the edge effects and provide the desired electric-field uniformity in the central part of the photocathode. The copper grating was used for applying either accelerating or decelerating electric field when measuring $QE(\hbar\omega)$ or $N_e(\varepsilon_\parallel)$, respectively. The final heat cleaning of the photodiode units, the application of a (Cs, O) layer to the atomically pure *p*-GaN surface for obtaining ENEA, and the hermetic attachment of the photocathode holder to the frame edge through a deformable indium gasket were performed in a ~10^{-9} Pa vacuum. The atomically pure and structurally ordered GaN surface was obtained by heat cleaning of the photodiode for 30 min at a temperature of 450–500°C. After the semiconductor was cooled to room temperature, the activator (Cs, O) coating was applied to the surface to ensure the ENEA state. The maximal photocathode quantum efficiency was achieved for 0.7 cesium monolayers and ~0.01 oxygen monolayers.

The $QE(\hbar\omega)$ and $N_e(\varepsilon_\parallel)$ dependences were measured on the setup described in [7]. A deuterium DDS-30 lamp was used as a light source at $\hbar\omega \geq 3.6$ eV, and a halogen KGM-24-150 lamp was used at $\hbar\omega < 3.6$ eV. The light spectral decomposition was accomplished using an MDR-23 monochromator. To suppress the influence of the scattered short-wavelength radiation on the measurement accuracy at $\hbar\omega \leq 3.6$ eV, a set of light filters was used. All measurements were made at room temperature.

The preliminary measurements with the ADES-500 electron spectrometer had shown that the use of the pure N_2 atmosphere in chemical processing, mounting the GaN samples on the holder, and carrying them into the high-vacuum chamber afforded an atomically pure and ordered GaN surface after heating at $T \geq 450$°C [6]. The XPS-measured residual carbon and oxygen concentrations did not exceed 3–5% of a monolayer. The electron diffraction with energy 70–100 eV suggested that the surface was ordered and had the (1 × 1) structure.

To determine the types of optical transitions responsible for the photoemission, the quantum-efficiency spectrum of the *p*-GaN(Cs, O) photocathode was measured. The corresponding results are shown in Fig. 1. One can see that the long-wavelength photoemission threshold occurs at $\hbar\omega_{th} \simeq 1.3$ eV. At $\hbar\omega > \hbar\omega_{th}$, the quantum efficiency rapidly increases. The increase in $QE(\hbar\omega)$ is decelerated at $\hbar\omega \simeq 2$ eV, after which it is again accelerated at $\hbar\omega \simeq \hbar\omega_g = 3.4$ eV, where the interband transitions from the valence subbands come into play. At $\hbar\omega > 3.6$ eV, the quantum efficiency increases by a factor of ~3, mainly due to the increase in the efficiency of photoelectron "gathering" by the emitter surface as a result of a decrease in the light-absorption depth and increase in the fraction of hot (nonthermalized) photoelectrons that did not lose the photon-endowed kinetic energy before escaping into vacuum. The maximal value QE = 27% was achieved at $\hbar\omega$ = 5.2 eV.

At $\hbar\omega < \hbar\omega_g$, the photoemission from the semiconductors with ENEA can be caused by the emission from the occupied surface states. However, in the leucosapphire-grown GaN it is mainly due to the electron photoexcitation from the bulk in-gap defect levels. The point is that the gallium nitride grown on leucosapphire has many structural defects that create the in-gap electronic states. The optical transitions from the occupied states lying below the Fermi level to the unoccupied states manifest themselves in the GaN absorption spectra [8]. The length of the tail in the $QE(\hbar\omega)$ curve at $\hbar\omega < \hbar\omega_g$ coincides approximately with the length of absorption tails.

To gain information about the photoemission mechanism at $\hbar\omega < \hbar\omega_g$, we measured the energy distributions of emitted electrons. The results are presented in Fig. 2. To improve the signal-to-noise ratio, measurements with $\hbar\omega$ = 1.17, 1.27, and 1.58 eV were carried out using lasers with a power of ~10^{-2} W. One can see from the figure that the $N_e(\varepsilon_\parallel)$ distributions measured for $\hbar\omega$ = 1.17 and 1.27 eV coincide and have the form of a narrow peak with a FWHM of ~60 meV. We assumed that the position of the low-energy wing of

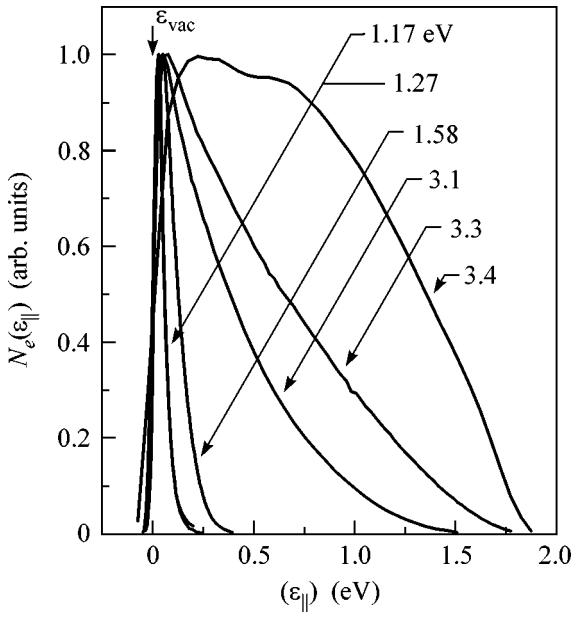

Fig. 2. Distributions of emitted electrons in longitudinal energy upon the excitation with light $\hbar\omega < \hbar\omega_g$.

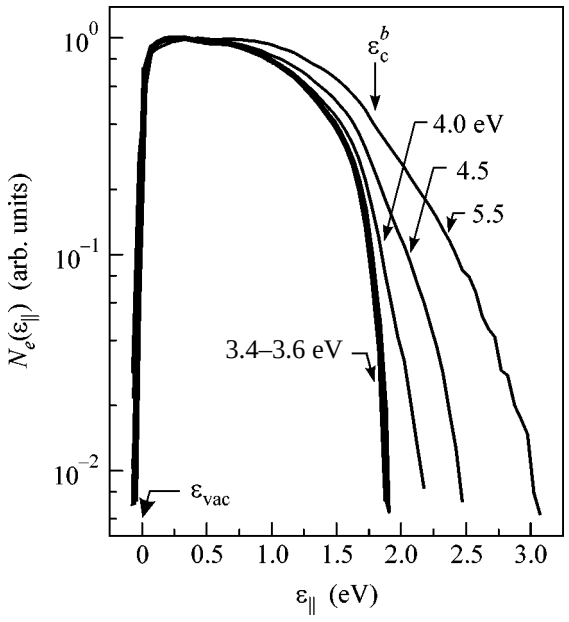

Fig. 3. Distributions of emitted electrons in longitudinal energy upon the excitation with light $\hbar\omega \geq \hbar\omega_g$.

this peak (determined from the condition that the derivative $\partial N_e(\varepsilon_\parallel)/\partial\varepsilon_\parallel$ is maximal) coincides with the vacuum level ε_{vac}. The shape of the $N_e(\varepsilon_\parallel)$ curve is independent of $\hbar\omega$ at $\hbar\omega \leq 1.27$ eV, because electrons are photoexcited to the states lying below the vacuum level. The additional energy necessary for the escape into vacuum electrons acquire through the phonon absorption; i.e., a two-step photothermal photoemission mechanism is dominant at the low-energy threshold of the photoeffect in *p*-GaN(Cs, O) with ENEA. As $\hbar\omega$ increases to 1.58 eV, the high-energy wing of $N_e(\varepsilon_\parallel)$ undergoes a shift of ~0.15 eV to higher energies. This signifies that the initial energy of photoelectrons for this $\hbar\omega$ exceeds the vacuum level by ~0.15 eV, so that hot electrons appear in the distribution of emitted electrons. As the photon energy increases to 3.30 eV, the length of high-energy wing in the $N_e(\varepsilon_\parallel)$ distribution increases without any qualitative change in its shape.

Upon a further increase in $\hbar\omega$ of only 0.1 eV, the shape of $N_e(\varepsilon_\parallel)$ qualitatively changes because the interband transitions start to contribute to the photoemission. Therefore, the lowest photon energy corresponding to the appearance of photoemission from the interband transitions coincides with ε_g, which proves the existence of the ENEA states at the *p*-GaN(Cs, O) surface. Note that, although the valence band of the hexagonal GaN consists of three subbands split by ~20 meV [9], we failed to discriminate between the transitions from these subbands. The shape of $N_e(\varepsilon_\parallel)$ at $\hbar\omega \geq \varepsilon_g$ is shown in Fig. 3. One can see that three distributions measured for $\hbar\omega$ = 3.40, 3.50, and 3.60 eV coincide with each other within the experimental error. The fact that $N_e(\varepsilon_\parallel)$ is independent of $\hbar\omega$ at $\hbar\omega \simeq \varepsilon_g$ is further proof of the existence of a surface ENEA state, for which small changes (caused by small changes in $\hbar\omega$) in the initial energy of photoelectrons excited in the semiconductor bulk are leveled off as a result of the thermalization before the escape into vacuum. For this reason, the shape of a high-energy wing of the $N_e(\varepsilon_\parallel)$ distribution is determined, to a large measure, by the Maxwellian distribution of the thermalized electrons in the quasi-neutral semiconductor bulk. The $N_e(\varepsilon_\parallel)$ wing took the exponential form with a slope of ~40 meV starting at $\varepsilon_\parallel \simeq 1.7$ eV. This energy was taken to be equal to the energy ε_c^b of conduction-band bottom in the semiconductor bulk. We attribute the fact that the slope of the $N_e(\varepsilon_\parallel)$ wing differs from kT = 26 meV to the wing broadening mainly caused by small variations in the initial position of vacuum level over the emitter surface. Inasmuch as the ε_c^b energy measured from ε_{vac} coincides, by definition, with $|\chi^*|$, measurement of $N_e(\varepsilon_\parallel)$ is the most direct and reliable method of measuring this value.

It follows from Fig. 3 that the length of high-energy wing of $N_e(\varepsilon_\parallel)$ increases with increasing $\hbar\omega$ to 4.00 eV and achieves ~1.25 eV at $\hbar\omega$ = 5.5 eV. The increase in the wing length is caused by the increase in the fraction of hot electrons that did not lose completely the excess kinetic energy before the escape into vacuum.

The results obtained in this work can be used to refine the parameters in the energy diagram of the *p*-GaN(Cs, O)–vacuum interface (Fig. 4). The diagram was constructed in the following way. A change in the work function φ_{th} upon coating with 0.5 ML Cs up to the maximal *QE* value was measured by the Anderson

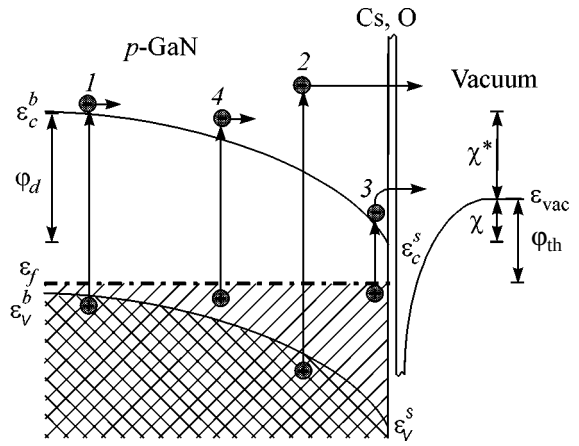

Fig. 4. Energy diagram of the *p*-GaN(Cs, O)–vacuum interface: ε_v is the valence-band top; ε_c is the conduction-band bottom; ε_f is the Fermi level; ε_{vac} is the vacuum level; (*1*) electrons excited by the light with $\hbar\omega \simeq \hbar\omega_g$; (*2*) hot photoelectrons excited by the light with $\hbar\omega > \hbar\omega_g$; (*3*) electrons excited by the light with $\hbar\omega \simeq \varphi_{th}$; and (*4*) hot electrons excited from the states with $\varepsilon_v < \varepsilon < \varepsilon_f$.

method in ADES-500 to give $\Delta\varphi_{th} = 2.5$ eV. Simultaneously, XPS measurements suggested that the GaN ground states did not change their energy position, indicating that the band bending did not change. Consequently, the measured $\Delta\varphi_{th}$ value was caused by a change only in the electron affinity χ^0 of the pure GaN surface. The use of a thicker coating consisting of 0.7 ML cesium and 0.01 ML oxygen for the activation of the photocathode to the maximal value of *QE* resulted in a decrease, by estimate, of 2.6 eV in χ^0. By taking the literature value $\chi^0 = 3.3$ eV [3, 4], we find that, after applying (Cs, O), the true electron affinity χ of the activated *p*-GaN surface is positive in our case and equal to 0.7 eV. The work function φ_{th} of the *p*-GaN (Cs, O) surface was determined by the photoelectric method using the data given in Fig. 2. The fact that the shape of the $N_e(\varepsilon_\parallel)$ curve is independent of $\hbar\omega$ at $\hbar\omega \leq 1.27$ eV is evidence that $\varphi_{th} \geq 1.27$ eV. At the same time, hot electrons with the energy ~0.15 eV higher than the electron energy in the Maxwellian tail appear in the $N_e(\varepsilon_\parallel)$ distribution at $\hbar\omega = 1.58$ eV. Consequently, the value of φ_{th} is higher than 1.27 eV but lower than 1.58 eV by approximately 0.15 eV; i.e., it is equal to ~1.4 eV. By subtracting the value of χ from φ_{th}, we find that the conduction-band bottom ε_c^s at the surface differs from the Fermi energy ε_f by 0.7 eV. The near-surface band bending φ_d can be determined in two ways. It follows from Fig. 4 that $\varphi_d = \chi + |\chi^*|$. By substituting $|\chi^*| = 1.7$ eV into this expression, we find $\varphi_d = 2.4$ eV. On the other hand, φ_d can be determined from the relation $\varphi_d = \varepsilon_g - \varepsilon_c^s - \varepsilon_f$, where ε_f is measured from the valence-band top in the quasi-neutral semiconductor bulk. By inserting into this expression the values $\varepsilon_g = 3.4$ eV [9] and $\varepsilon_f = 0.3$ eV [1] corresponding to GaN doped with Mg to the concentration $p \simeq 10^{17}$ cm^{-3}, one finds $\varphi_d = 2.4$ eV.

Of interest is to compare our data with the results obtained in [3, 4] by different methods. For the sake of convenience, the results are compiled in the table.

One can see from the table that the disparity between the χ^* values obtained by different authors is large and exceeds the possible experimental errors. A certain contribution to the scatter of the χ^* values comes from $\Delta\chi$ values that can be different in different experiments because of the difference in the composition of activating coating and the methods and temperature of its preparation. Nevertheless, the scatter in the near-surface band bending is the main reason for the scatter in χ^*. Note also that in [4], as in our experiments, the band bending did not change upon cesium adsorption, whereas in [3] it increased upon cesium adsorption and decreased upon oxygen adsorption. The fact that φ_d does not depend on the adsorbed cesium is strong evidence that the original surface charge is much larger than the additional charge carried by cesium to the GaN surface. At the same time, the small value of φ_d and its "proper" variation upon the adsorption of electropositive cesium are evidence of an appreciably lower charge density at the original surface of a GaN sample studied in [3]. In that work, the atomically pure surface was prepared by ion bombardment followed by vacuum annealing at 900°C to obtain a high density of surface states. In our experiments, as in [4], more "subtle" methods were used for the preparation of clean

Parameters of the energy diagram of the *p*-GaN(Cs, O)–vacuum interface

χ^0, eV	$\Delta\chi$, eV	χ, eV	$\lvert\chi^*\rvert$, eV	$\Delta\varphi_d$, eV	φ_d, eV	Coating	Temperature	Ref.
3.35	2.3	1.0	2.1	0 (Cs)	3.1	Cs	150 K	[4]
3.3	2.8	0.5	0.7	+0.2 (Cs) −0.4 (O_2)	1.2	O + Cs	RT	[3]
3.3	2.6	0.7	1.7	0 (Cs)	2.4	Cs + (Cs, O)	RT	This work

Note: χ^0 is the electron affinity of a clean GaN surface; $\Delta\chi$ is the decrease in affinity upon activation; χ is the electron affinity of the activated surface; χ^* is the effective electron affinity of the activated surface; $\Delta\varphi_d$ is the change in band bending upon activation; and φ_d is the band bending of the activated surface.

GaN surface. It is thus improbable that the high density of charged surface defects is responsible for the band bending stronger than in [3] and for its independence of the adsorption of electropositive cesium. It would be natural to assume that the strong band bending in [4] and in our experiments is caused by a high electric-field strength due to the piezoelectric effect in the strained GaN layers grown on Al_2O_3. In the gallium nitride grown on SiC [3], the residual stress and the piezofield are substantially weaker, because the matching of the lattice parameters and the thermal expansion coefficients in the GaN/SiC structure is better than in our system. As a result, the piezofield likely has no effect on the φ_d and the value of φ_d is smaller and depends on the sign and magnitude of the charge on the surface and adsorption states.

In summary, the energy distributions of photoelectrons emitted from the localized defect states and the band states of *p*-GaN(Cs, O) with effective negative electron affinity have been measured, the main photoemission characteristics and mechanisms have been revealed for different spectral regions, and data indicative of a strong influence of the piezoeffect on the band bending and the effective negative electron affinity in the strained GaN have been obtained.

We are grateful to V.V. Lundin, E.E. Zavarin, and A.I. Besyul'kin (Ioffe Physicotechnical Institute, Russian Academy of Sciences) for providing the GaN layers. This work was supported in part by the Russian Foundation for Basic Research (project no. 04-02-16639).

REFERENCES

1. F. Machuca, Y. Sub, Z. Liu, *et al.*, J. Vac. Sci. Technol. B **18**, 3042 (2000).
2. R. W. Hunt, L. Vanzetti, T. Castro, *et al.*, Physica B (Amsterdam) **185**, 415 (1993).
3. C. I. Wu and A. Kahn, J. Appl. Phys. **86**, 3209 (1999).
4. M. Eyckeler, W. Mönch, T. U. Kampen, *et al.*, J. Vac. Sci. Technol. B **16**, 2224 (1998).
5. O. E. Tereshchenko, S. I. Chikichev, A. S. Terekhov, *et al.*, J. Vac. Sci. Technol. A **17**, 2655 (1999).
6. O. E. Tereshchenko, G. É. Shaĭbler, A. S. Yaroshevich, *et al.*, Fiz. Tverd. Tela (St. Petersburg) (in press).
7. V. V. Bakin, A. A. Pakhnevich, S. N. Kosolobov, *et al.*, Pis'ma Zh. Éksp. Teor. Fiz. **77**, 197 (2003) [JETP Lett. **77**, 167 (2003)].
8. O. Ambacher, W. Rieger, P. Ansmann, *et al.*, Solid State Commun. **97**, 365 (1996).
9. B. Monemar, in *Optical Properties of GaN, Semiconductors and Semimetals* (Academic, New York, 1998), p. 50.

Translated by V. Sakun

JETP Letters, Vol. 79, No. 10, 2004, pp. 484–488. Translated from Pis'ma v Zhurnal Éksperimental'noĭ i Teoreticheskoĭ Fiziki, Vol. 79, No. 10, 2004, pp. 597–601.

Investigation of a Superconducting $Mg_{1-x}Al_xB_2$ System by Tunneling and Microjunction (Andreev) Spectroscopies

Ya. G. Ponomarev[1], S. A. Kuzmichev[1], N. M. Kadomtseva[1], M. G. Mikheev[1], M. V. Sudakova[1], S. N. Chesnokov[1], E. G. Maksimov[2], S. I. Krasnosvobodtsev[2], L. G. Sevast'yanova[3], K. P. Burdina[3], and B. M. Bulychev[3]

[1] *Faculty of Physics, Moscow State University, Vorob'evy gory, Moscow, 119899 Russia*

[2] *Lebedev Physical Institute, Russian Academy of Sciences, Leninskiĭ pr. 53, Moscow, 117924 Russia*

[3] *Department of Chemistry, Moscow State University, Vorob'evy gory, Moscow, 119899 Russia*

Received April 7, 2004

A detailed investigation of multiband superconductivity in the $Mg_{1-x}Al_xB_2$ system was carried out by the methods of tunneling and Andreev spectroscopy. Temperature dependences of the superconducting gaps and their variation upon an increase in the degree of disorder and the Al concentration were studied. It is shown that the experimentally observed dependences cannot be explained in detail within the framework of the presently available microscopic theories. © *2004 MAIK "Nauka/Interperiodica".*

PACS numbers: 74.70.Dd; 74.50.+r; 74.45.+c

Since the superconductivity with a relatively high critical temperature $T_c = 40$ K was discovered in MgB_2 several years ago [1], it has persisted in attracting the attention of researchers. Interest in MgB_2 is caused by the fact that at least two superconducting gaps were observed in two different regions of the Fermi surface of this material. The properties of such multiband superconductors were studied in many theoretical works after the publication of pioneer works [2, 3] in the mid-20th century. The most interesting prediction was made by Leggett [4] in 1966. He has shown that multiband superconductors can possess specific collective excitations due to the fluctuations of the relative order-parameter phases of different superconducting condensates.

The multiband superconductivity phenomenon is akin, in some sense, to the anisotropy phenomenon, which is inherent in almost all superconductors. It is well known that the anisotropy of superconducting gap can easily be broken by impurities. Even from the early works [3, 4], it has become clear that the multiband character of superconducting gaps must disappear in the dirty limit. A surprising property of multiband superconductivity in the MgB_2 system is that it does not disappear even if the residual resistance increases by two or more orders of magnitude. A possible reason for this phenomenon was formulated in [5], where it was attributed to the specific features of the electron bands in MgB_2.

The *ab initio* calculations of the electronic structure of MgB_2 [6–8] showed that the Fermi surface of magnesium diboride contains two slightly corrugated coaxial cylindrical surfaces belonging to two 2D σ bands and two complex tubular structures formed by two 2D π bands. Two-dimensional (2D) charge carriers—holes localized in the boron planes—correspond to the σ bands. Three-dimensional (3D) electrons and holes are delocalized over the entire crystal and correspond to the π bands. The multiband superconductivity in MgB_2 is stable because the scattering potentials between the σ and π bands are small [5]. It is worth noting that the real four-band spectrum of MgB_2 [8] is usually modeled by a two-band spectrum [5–7], while the number of superconducting gaps is reduced to two: Δ_σ (σ band; large gap) and Δ_π (π band; small gap). In a number of works [9–15], the Δ_σ and Δ_π gaps in MgB_2 at $T \longrightarrow 0$ and their temperature dependences $\Delta_\sigma(T)$ and $\Delta_\pi(T)$ were determined using tunneling and microjunction spectroscopies (see also reviews [16, 17]).

The two-band behavior of polycrystalline MgB_2 samples differing in the degree of defectness was studied in our work [18]. It was shown that the temperature dependences of the larger gap $\Delta_\sigma(T)$ was close to the BCS type. At the same time, the $\Delta_\pi(T)$ dependences showed a deviation from the standard BCS function. The critical temperatures of the samples studied in [18] showed a sizable scatter due to the technological regime of their preparation and fell within the 25 K $\leq T_c \leq$ 40.5 K interval. The value of Δ_σ in different samples decreased linearly with decreasing temperature T_c, whereas the small Δ_π gap had virtually the same value $\Delta_\pi \approx 2$ meV over the entire interval of T_c values.

The purpose of this work was the systematic study of the $Mg_{1-x}Al_xB_2$ system. According to the data in [19–21], the critical temperature T_c of the $Mg_{1-x}Al_xB_2$

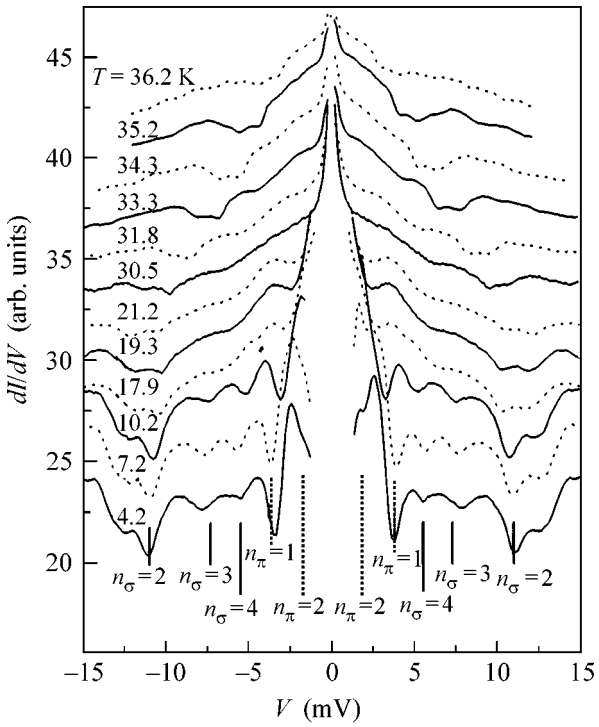

Fig. 1. Subharmonic gap structure on the *dI*/*dV* characteristics of the SnS junction at different temperatures for a polycrystalline MgB_2 sample with T_c = 39 K. Dashes indicate the biases *V* corresponding to the dynamic-conductivity dips labelled n_σ (σ band; solid lines) and n_π (π band; dotted lines); *T* = 4.2 K.

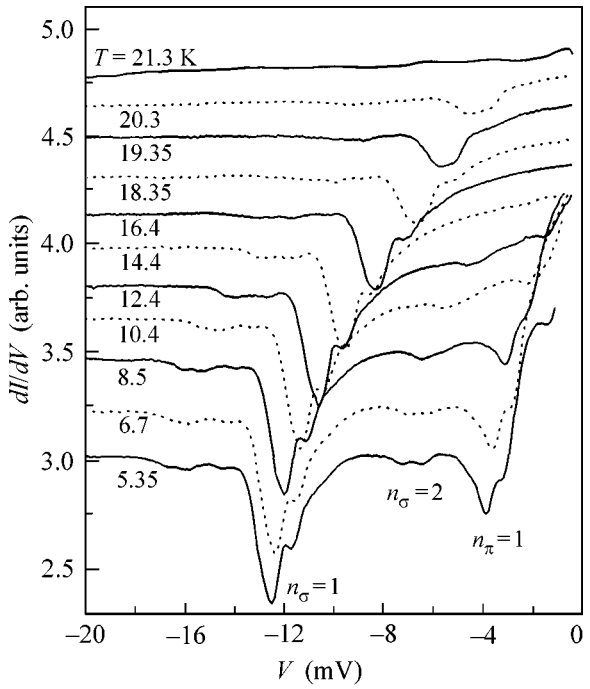

Fig. 2. Influence of temperature on the subharmonic gap structure on the *dI*/*dV* characteristic of the Andreev junction in a polycrystalline $Mg_{1-x}Al_xB_2$ sample with T_c = 21.5 K. The dynamic-conductivity dips labelled n_σ (σ band) and n_π (π band) are indicated in the figure.

system decreases with increasing aluminum concentration *x* and turns to zero at $x \approx 0.5$. There is only one experimental work [22] where the $\Delta_\sigma(x)$ and $\Delta_\pi(x)$ dependences were determined for a limited number of $Mg_{1-x}Al_xB_2$ samples.

We studied polycrystalline $Mg_{1-x}Al_xB_2$ samples with concentrations of $0.32 \le x \le 0.45$ and, correspondingly, critical temperatures of 21.5 K $\ge T_c \ge$ 6.5 K. Microjunction (Andreev) and tunneling spectroscopies were used as experimental methods. Both methods were implemented by the use of break junctions. Due to the high surface quality of a cryogenic cleavage, the experimental results are well reproducible, making break junctions more suitable than the other tunneling structures. The unique advantage of a break junction is that it can be adjusted in the course of a low-temperature experiment and carried from the tunneling regime (tunneling spectroscopy; SIS junction) to the microjunction regime (Andreev spectroscopy; SnS junction, where n stands for normal metal) with relative ease.

In this work (as in [18]), the gap structure on the *dI*/*dV* characteristics of the junctions in the tunneling regime at *T* = 4.2 K (differential conductivity peaks corresponding to the biases $V_{\sigma,\pi} = 2\Delta_{\sigma,\pi}/e$) is compared with the subharmonic gap structure for the same junctions in the microjunction regime (two series of differential conductivity dips corresponding to the biases $V_{n,\sigma,\pi} = 2\Delta_{\sigma,\pi}/ne$, where *n* is an integer). The reliability of determining the superconducting gaps is substantially enhanced if the $\Delta_{\sigma,\pi}$ values obtained by the two aforementioned methods coincide.

It should be noted that the measurement of the temperature dependences $\Delta_\sigma(T)$ and $\Delta_\pi(T)$ by Andreev spectroscopy is more preferable, because the subharmonic gap structure remains rather pronounced virtually up to the critical temperature T_c. This allows the estimation of the local critical temperature in the microjunction region. Hereafter, by the critical temperature is meant the local T_c. A good coincidence of the local T_c with the critical temperature derived from the resistive transition of the whole sample (prior to the formation of a break junction) is observed only in the cleanest MgB_2 samples.

The subharmonic gap structure on the *dI*/*dV* characteristics of the SnS junction in a MgB_2 sample with T_c = 39 K is shown in Fig. 1 for different temperatures.

The influence of temperature on the subharmonic gap structure on the *dI*/*dV* characteristic of the Andreev junction in a $Mg_{1-x}Al_xB_2$ sample with T_c = 21.5 K is shown in Fig. 2. The features at the *V* biases corresponding to two gaps (Δ_σ and Δ_π) are clearly seen in the figures. The doublet character of the subharmonic gap

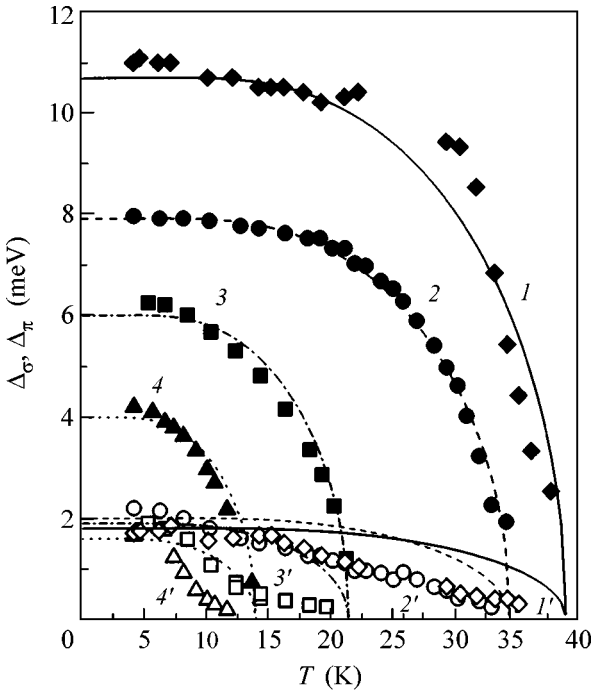

Fig. 3. Temperature dependences of the (*1–4*; dark symbols) large Δ_σ and (*1'–4'*; open symbols) small Δ_π gaps in the polycrystalline samples: (*1*, *1'*) MgB_2 with T_c = 39 K, (*2*, *2'*) defective MgB_2 with T_c = 34.5 K, (*3*, *3'*) $Mg_{1-x}Al_xB_2$ with T_c = 21.5 K, and (*4*, *4'*) $Mg_{1-x}Al_xB_2$ with T_c = 14 K. The solid, dashed, and dot-and-dash lines correspond to the BCS model.

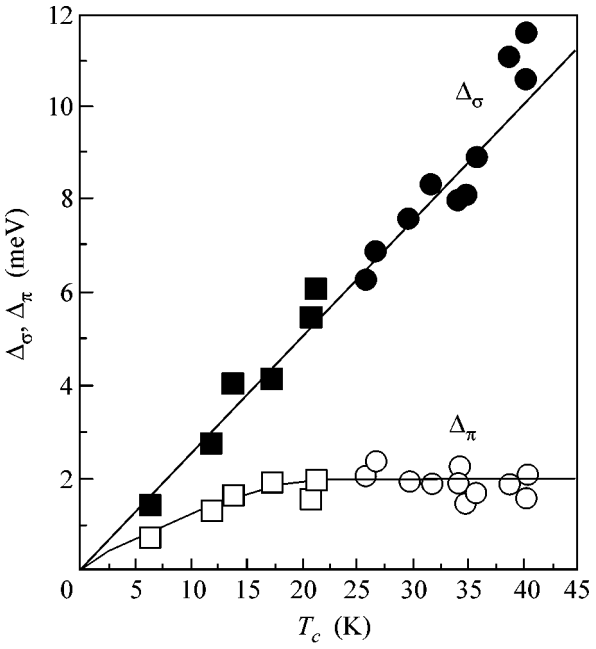

Fig. 4. The (dark symbols) Δ_σ and (open symbols) Δ_π gaps at $T \longrightarrow 0$ as functions of critical temperature T_c. Circles correspond to the results obtained for the MgB_2 samples differing in the degree of defectness, and squares correspond to the results obtained for the $Mg_{1-x}Al_xB_2$ samples. The solid lines are drawn for convenience sake.

structure, particularly pronounced in Fig. 2, is noteworthy. It is not improbable that the doublets often observed by us in the high-quality characteristics are due to the presence of the closely spaced Δ_σ gap and two Δ_π gaps in magnesium diboride, as was predicted in the theoretical work of Choi *et al.* [8].

The temperature dependences of the gaps in the two aforementioned samples and in two another samples, one of which is free of Al impurity and has the critical temperature T_c = 34.5 K, are presented in Fig. 3. One can see in Fig. 3 that the temperature dependences $\Delta_\sigma(T)$ and $\Delta_\pi(T)$ in the $Mg_{1-x}Al_xB_2$ system are qualitatively different. The $\Delta_\sigma(T)$ dependences are close to the BCS type (dark symbols in Fig. 3). However, the $\Delta_\pi(T)$ gap behaves in a cardinally different way. The appearance of a tail in the $\Delta_\pi(T)$ curve is evidence of the influence of the σ condensate on the π condensate as a result of the internal proximity effect. The curves in Fig. 3 more closely resemble the corresponding graphs for the standard proximity effect between two weakly coupled superconductors with sizably different T_c values. One can thus assume that the MgB_2 π band possesses intrinsic superconductivity with $T_c \approx 13$ K, while the interband coupling constant $\lambda_{\sigma\pi}$ is appreciably smaller than the value of 0.23 obtained in [7, 23]. This becomes clear after the comparison of the $\Delta_\pi(T)$ dependences obtained in this work (Fig. 3) with the corresponding dependence obtained in [23] and virtually coinciding with the BCS type.

The dependences of the Δ_σ and Δ_π gaps on the critical temperature T_c at $T \longrightarrow 0$ are shown in Fig. 4. The circles are the results obtained for the MgB_2 samples differing in the degree of defectness, and the squares are the results obtained for the $Mg_{1-x}Al_xB_2$ samples. It follows from Fig. 4 that the interband coupling shows appreciable strengthening neither upon an increase in the disorder in MgB_2 nor upon an increase in the Al concentration.

Several reasons for a possible decrease in T_c and, correspondingly, in Δ_σ upon substituting Al for Mg were proposed in the literature. First, the hole σ band in this case is filled with extra electrons from aluminum, resulting in an appreciable decrease in the electron density of states and eventually in the gap collapse at $x >$ 0.5 [21, 25]. The second reason is that the interband scattering strengthens with an increase in the impurity concentration. It is well known that the anisotropy of superconducting gap in conventional single-band superconductors is suppressed due to the scattering from nonmagnetic impurities [25]. Accordingly, the T_c of such a superconductor also decreases. It was shown by Golubov and Mazin [26] that an analogous phenom-

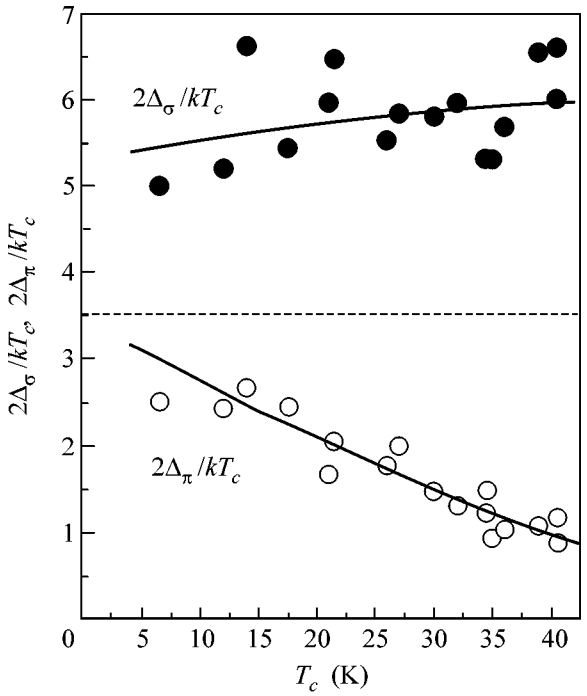

Fig. 5. The (dark symbols) $2\Delta_\sigma/kT_c$ and (open symbols) $2\Delta_\pi/kT$ ratios as functions of critical temperature T_c for the studied polycrystalline MgB_2 samples differing in the degree of defectness and the $Mg_{1-x}Al_xB_2$ samples. The solid lines are drawn for the sake of convenience, and the dashed line corresponds to the BCS limit.

enon should also be observed in multiband superconductors. The calculations carried out in [27–29] on the basis of both these ideas are in sharp contrast to our results. We did not observe the predicted increase in the smaller Δ_π gap upon a decrease in T_c. Moreover, we did not observe the transition to the dirty single-gap limit down to $T_c \approx 6$ K, where both Δ_σ and Δ_π gaps must coincide.

We would also like to call attention to the fact that the decrease in Δ_σ upon disordering and addition of Al is accompanied by a very small change in the $2\Delta_\sigma/kT_c$ ratio. Moreover, one can see from Fig. 5 that this ratio sizably exceeds the value typical of the BCS limit. It also exceeds the value $2\Delta_\sigma/kT_c = 4.1$ calculated in [5–7, 23]. It should be noted that $2\Delta_\pi/kT_c$ values exceeding 3.52 were also obtained in a number of other experimental works on MgB_2 [30–32]. At the same time, the $2\Delta_\pi/kT_c$ ratio tends to 3.52 at $T_c \longrightarrow 0$ (Fig. 5). This fact indicates that the intrinsic superconductivity of the π bands corresponds to the BCS limit.

There can be no doubt to us that the strong electron–phonon interaction is the main mechanism responsible for high T_c values in MgB_2. Unfortunately, the available calculations [5–8, 23] cannot describe in detail the results obtained in this work. The experimental value of $2\Delta_\sigma/kT_c$ proves to be appreciably larger than its theoretical value. In addition, our data indicate that the values of interband electron–phonon coupling constants are overestimated in [5–8, 33]. This fact was discussed in our previous work [18], where plasma-type collective excitations (Leggett modes) were observed in MgB_2. It was also pointed out in [18] that these modes could not be observed in MgB_2 if the interband constants were as large as those obtained in the theoretical works.

We are grateful to V.F. Gantmakher, L.M. Fisher, and M.R. Trunin for helpful discussions. This work was supported by the Russian Foundation for Basic Research (project nos. 02-02-16658, 02-02-17915, 02-02-17353), INTAS-2001-0617, and the scientific programs of the Russian Academy of Sciences and the Ministry of Industry, Science, and Technology.

REFERENCES

1. J. Nagamatsu, N. Nakagawa, T. Muranaka, *et al.*, Nature **410**, 63 (2001).
2. H. Suhl, B. T. Mattias, and L. R. Walker, Phys. Rev. Lett. **3**, 552 (1959).
3. V. A. Moskalenko, Fiz. Met. Metalloved. **4**, 503 (1959).
4. A. J. Leggett, Prog. Theor. Phys. **36**, 901 (1966).
5. I. I. Mazin, O. K. Andersen, O. Jepsen, *et al.*, Phys. Rev. Lett. **89**, 107002 (2002).
6. A. Y. Liu, I. I. Mazin, and J. Kortus, Phys. Rev. Lett. **87**, 087005 (2001).
7. Y. Kong, O. V. Dolgov, O. Jepsen, and O. K. Andersen, Phys. Rev. B **64**, 020501 (2001).
8. H. J. Choi, D. Roundy, H. Sun, *et al.*, Nature **418**, 758 (2002).
9. F. Giubileo, D. Roditchev, W. Sacks, *et al.*, cond-mat/0105592 v2 (2001).
10. H. Schmidt, J. F. Zasadzinski, K. E. Gray, *et al.*, Physica C (Amsterdam) **385**, 221 (2003).
11. P. Martinez-Samper, J. G. Rodrigo, G. Rubio-Bollinger, *et al.*, cond-mat/0209387 (2002).
12. P. Szabó, P. Samuely, J. Kačmarčík, *et al.*, cond-mat/0105598 v3 (2001).
13. M. Iavarone, G. Karapetrov, A. E. Koshelev, *et al.*, Phys. Rev. Lett. **89**, 187002 (2002).
14. R. S. Gonnelli, D. Daghero, G. A. Ummarino, *et al.*, cond-mat/0208060 v1 (2002).
15. Y. Bugoslavsky, Y. Miyoshi, G. K. Perkins, *et al.*, Supercond. Sci. Technol. **15**, 526 (2002).
16. I. K. Yanson and Yu. G. Naidyuk, cond-mat/0402095 v1 (2004).
17. C. Buzea and T. Yamashita, Supercond. Sci. Technol. **14**, R115 (2001).
18. Ya. G. Ponomarev, S. A. Kuzmichev, M. G. Mikheev, *et al.*, Solid State Commun. **129**, 85 (2004).
19. J. S. Slusky, N. Rogato, K. A. Began, *et al.*, Nature **410**, 343 (2001).
20. A. Bianconi, S. Agrestini, D. Di Castro, *et al.*, Phys. Rev. B **65**, 174515 (2002).
21. D. Di Castro, S. Agrestini, G. Campi, *et al.*, Europhys. Lett. **58**, 278 (2002).

22. M. Putti, E. Galleani, I. Pallecchi, *et al.*, cond-mat/0306137 (2003).
23. A. A. Golubov, J. Kortus, O. V. Dolgov, *et al.*, J. Phys.: Condens. Matter **14**, 1353 (2002).
24. O. de la Pena, A. Aguayo, and R. de Coss, Phys. Rev. B **66**, 012511 (2002).
25. D. Markowitz and L. P. Kadanov, Phys. Rev. **131**, 563 (1963).
26. A. A. Golubov and I. I. Mazin, Phys. Rev. B **55**, 15146 (1997).
27. A. Bussman-Holder and A. Bianconi, Phys. Rev. B **67**, 132509 (2003).
28. G. A. Ummarino, R. S. Gonnelli, S. Massida, *et al.*, cond-mat/0310284 (2003).
29. K. Watanabe and T. Kite, cond-mat/0401410 (2004).
30. T. Takasaki, T. Ekino, T. Muranaka, *et al.*, Physica C (Amsterdam) **378–381**, 229 (2002).
31. Z.-Z. Li, H.-J. Tao, Y. Xuan, *et al.*, Phys. Rev. B **66**, 064513 (2002).
32. H. Kotegawa, K. Ishida, Y. Kitaoka, *et al.*, cond-mat/0201578 (2002).
33. A. Brinkman, A. A. Golubov, H. Rogalla, *et al.*, Phys. Rev. B **65**, 180517(R) (2002).

Translated by V. Sakun

JETP Letters, Vol. 79, No. 10, 2004, pp. 489–494. From Pis'ma v Zhurnal Éksperimental'noĭ i Teoreticheskoĭ Fiziki, Vol. 79, No. 10, 2004, pp. 602–607.

Coulomb Effects in a Nanoscale SINIS Junction¶

P. M. Ostrovsky* and M. V. Feigel'man

Landau Institute for Theoretical Physics, Russian Academy of Sciences, Moscow, 119334 Russia

**e-mail: ostrov@itp.ac.ru*

Received April 12, 2004

We study a system of two superconductors connected by a small normal grain. We consider the modification of the Josephson effect by the Coulomb interaction on the grain. Coherent charge transport through the junction is suppressed by Coulomb repulsion. An optional gate electrode may relax the charge blocking and enhance the current leading to the single Cooper pair transistor effect. Temperature dependences of critical current and of the minigap induced in the normal grain by the proximity to superconductor are studied. Both temperature and Coulomb interaction suppress critical current and minigap, but their interplay may lead to the nonmonotonic and even reentrant temperature dependence. © *2004 MAIK "Nauka/Interperiodica".*

PACS numbers: 73.21.–b; 74.45.+c; 74.50.+r

Nanoscale SINIS junction consists of a small normal metallic grain connected to two superconductive leads by tunnel junctions. The Josephson effect in this system is provided by the Andreev reflection processes at the contacts: Cooper pairs enter the normal part of the junction and propagate as Cooperons. This allows the transport of Cooper pairs from one lead to another establishing a supercurrent. Another manifestation of the Andreev mechanism is the appearance of a minigap in the spectrum of the normal grain: the proximity effect. This minigap is a result of a nonzero Cooper pairs density come from superconductors. The mentioned effects rely on the phase conservation in the grain. Charging effects lead to fluctuations of the phase and break the coherent electron transport as well as the induced minigap. The interplay between proximity and charging effects in a normal grain connected to one superconductor was recently studied in [1]. Here, we apply the same formalism to the system with two leads and consider the Josephson effect. We also study temperature dependence of the minigap and Josephson current and find some unexpected reentrant behavior in a certain range of parameters.

We consider tunnel junctions between normal grain and left (L) and right (R) superconductors characterized by large [in units of $e^2/\hbar$] normal-state conductances $G_{L,R} \gg 1$ and (geometric) capacitances $G_{L,R}$. The gate electrode is coupled to the grain by the capacitance C_g. Mean level spacing in the grain δ is the smallest energy scale of the system, while the superconductive gap Δ in the leads and Thouless energy E_{Th} of the grain are largest ones. We assume that Andreev conductances of both contacts are small, $G^A_{L,R} \leq 1$ (together with conditions $G_{L,R} \gg 1$, it means that our junctions contain many weakly transparent channels, quantitative estimates will be provided below). The proximity and charging effects in the grain are characterized by the bare minigap width $E_{g0} = (G_L + G_R)\delta/4$ and Coulomb energy $E_C = e^2/2C$, with $C = C_L + C_R + C_g + \Delta C$ being the total capacitance of the grain. Here, $\Delta C = \dfrac{e^2}{2\Delta}(G_L + G_R)$ is the contribution to capacitance coming from virtual quasiparticle tunnelling [2]. We assume that $\delta \ll (E_{g0}, E_C) \ll (\Delta, E_{\mathrm{Th}})$. With the help of the dynamical (in imaginary time) sigma model in replica space [3], and the adiabatic approximation for charging effects developed in [1], we study the current-phase relation of SINIS junction as well as the dependence of the critical current on temperature and gate voltage V_g.

Electronic properties of the normal grain are characterized by its Green function. To capture proximity induced correlations, one uses the matrix Green function in Nambu–Gor'kov representation. The sigma-model operates with the matrix field Q which apart from Nambu–Gor'kov structure carries two Matsubara energies and two replica indices. The standard Green function can be extracted from the diagonal in energies element of matrix Q by replica averaging. Charging effects are described by the fluctuating scalar field ϕ corresponding to the electric potential and also carrying the replica index in the sigma-model formalism. The action for the two variables Q and ϕ reads

$$S[Q,\phi] = -\frac{\pi}{\delta}\mathrm{Tr}[(\varepsilon\hat{\tau}_3 + \phi)Q]$$
$$-\frac{\pi}{4}\mathrm{Tr}[(G_L Q_L + G_R Q_R)Q] + \sum_a \int_0^{1/T} d\tau \frac{(\phi^a - eV_g)^2}{4E_C}. \quad (1)$$

¶ This article was submitted by the authors in English.

Here, $\hat{\tau}_i$ are the Pauli matrices in Nambu–Gor'kov space. The trace operation implies summation over all possible variables including replica indices and integration over energies. The equilibrium superconductive matrices $Q_{L,R}$ for the leads are diagonal in both energies and replicas and have the form $Q_{L,R}(\varepsilon) = \hat{\tau}_1 \cos\varphi_{L,R} + \hat{\tau}_2 \sin\varphi_{L,R}$ in Nambu–Gor'kov space with $\varphi_{L,R}$ being the superconductive phase of the left (right) lead. This expression is valid at energies well below Δ. The contribution from higher energies [2] has already been taken into account by renormalization of the capacitance: $C \mapsto C + e^2(G_L + G_R)/(2\Delta)$.

To exclude fast fluctuations due to shifts of the electron band by the potential ϕ from the matrix Q, we perform the following change of variables [4]:

$$\phi^a(\tau) = \dot{K}^a(\tau), \quad Q^{ab}_{\tau\tau'} = e^{i\hat{\tau}_3 K^a(\tau)} \tilde{Q}^{ab}_{\tau\tau'} e^{-i\hat{\tau}_3 K^b(\tau')}. \qquad (2)$$

The phase K is determined up to a constant, which will be fixed later to simplify further analysis. With new variables, the action takes the form

$$S[\tilde{Q}, K] = -\frac{\pi}{\delta}\mathrm{Tr}(\varepsilon\hat{\tau}_3\tilde{Q}) + \int_0^{1/T} d\tau \left[\frac{(\dot{K}-N)^2}{4E_C} - \frac{2\pi E_g(\varphi)}{\delta}(\tilde{Q}^{(1)}_{\tau\tau}\cos 2K + \tilde{Q}^{(2)}_{\tau\tau}\sin 2K)\right]. \qquad (3)$$

In this formula we put $\varphi = \varphi_L - \varphi_R$, denote $\tilde{Q}^{(i)} = \mathrm{tr}(\hat{\tau}_i\tilde{Q})/2$, $N = C_g V_g/e$, and introduce bare phase-dependent minigap

$$E_g(\varphi) = \frac{\delta}{4}\sqrt{G_L^2 + G_R^2 + 2G_L G_R \cos\varphi}. \qquad (4)$$

Expression (3) is very similar to the action for an SIN system with one superconductive lead [1]. The only difference is the phase dependence of E_g. Further calculation will essentially follow the procedure of [1]. The key idea is *the adiabatic approximation* based on the separation of characteristic frequencies of matrix $\tilde{Q}$ and phase K ensured by the inequality $E_C \gg \delta$. The characteristic timescale of the variable K fluctuations is much shorter than that of electronic degrees of freedom; thus, we integrate the action over $K(t)$ regarding $\tilde{Q}$ as a time-independent matrix (it depends only on the difference of its two time arguments). Then, we apply the *saddle point approximation* to the K-averaged action. The justification of this approximation will be provided below.

We parametrize the time-independent matrix Q by an angle α:

$$\tilde{Q}(\varepsilon) = \hat{\tau}_3\cos\alpha(\varepsilon) + \hat{\tau}_1\sin\alpha(\varepsilon). \qquad (5)$$

The $\hat{\tau}_2$ term here is eliminated by the proper choice of the constant in the definition of K. Inserting this expression into (3), we derive the Hamiltonian controlling the dynamics of the phase K:

$$\hat{H} = E_C[(-i\partial/\partial K - N)^2 - 2q(\varphi)\cos 2K]. \qquad (6)$$

All physical quantities depend periodically on N. It is convenient to assume that $|N| < 1/2$. The parameter $q(\varphi)$ is expressed in terms of the angle $\alpha(\varepsilon)$

$$q(\varphi) = \frac{\pi E_g(\varphi) T}{E_C \delta}\sum_{\varepsilon_n}\sin\alpha(\varepsilon_n). \qquad (7)$$

This sum diverges logarithmically and should be cut off at $|\varepsilon| \sim \Delta$. For large values of q, the phase K is nearly localized in the minima of cosine potential and the fluctuations are weak. In the opposite case, fluctuations of the phase get strong and the proximity effect is mostly suppressed. Thus, the parameter q quantifies the strength of proximity coupling competing with the charging effect.

With the derived Hamiltonian, we are able to calculate the free energy of the K degree of freedom $F(q, T)$ and then extract the total free energy of the system from action (3)

$$\mathcal{F} = -\frac{2\pi T}{\delta}\sum_{\varepsilon_n}\varepsilon_n\cos\alpha(\varepsilon_n) + F(q, T). \qquad (8)$$

The equilibrium value of $\alpha(\varepsilon)$ is determined by the minimum of this free energy functional (saddle-point approximation). This gives $\tan\alpha(\varepsilon) = \tilde{E}_g/\varepsilon$, with $\tilde{E}_g$ obeying the self-consistency equation

$$\frac{\tilde{E}_g}{E_g(\varphi)} = -\frac{1}{2E_C}\frac{\partial F}{\partial q}. \qquad (9)$$

This $\tilde{E}_g$ is the minigap appearing in the spectrum of the normal grain. The estimation of matrix $\tilde{Q}$ fluctuations justifies the saddle-point approximation, provided $\tilde{E}_g \gg \delta$. The system of two equations (7) and (9) determines two parameters, q and $\tilde{E}_g$. A trivial solution $q = \tilde{E}_g = 0$ always exists. It is analogous to the normal state, which is the stationary point (local maximum) of the superconductor free energy. We are looking for a nontrivial solution leading to nonzero value of the minigap $\tilde{E}_g$. Once this solution exists, it has lower energy than the trivial solution.

After solving the equations, we can calculate free energy (8) and all physical properties of the junction. We are interested in the current–phase relation given by the identity $I(\varphi) = (2e/\hbar)(d\mathcal{F}/d\varphi)$. Using self-consis-

tency relation (9) and identity (7), we express the current as

$$I(\varphi) = \frac{e\delta^2 E_C \tilde{E}_g q}{4\hbar E_g^3(\varphi)} G_L G_R \sin\varphi. \quad (10)$$

Below, we consider analytically two limiting cases of weak ($q \gg 1$) and strong ($q \ll 1$) charging effect and then discuss the numerical results for arbitrary q. The spectrum of Hamiltonian (6) is given by the characteristic values of the Mathieu equation, which is elementary solved in these two limits. We first calculate the current at zero temperature, taking the ground state of (6) for the free energy F.

Weak Coulomb blockade. When charging effects are weak and the parameter q is large, the phase K is localized near 0 or π in the minima of the cosine potential. The applied gate voltage is ineffective in this case. Expanding the potential to the second order near its minimum, we find the ground state energy $E_0 = E_C(-2q + 2\sqrt{q})$. The pair of equations (7), (9) can be solved iteratively. In the considered regime, the minigap is slightly suppressed in comparison with its bare value $E_g(\varphi)$. First, we estimate q, substituting $E_g(\varphi)$ in the r.h.s. of (7)

$$q_0 = \frac{E_g^2(\varphi)}{E_C\delta}\log(\Delta/E_{g0}). \quad (11)$$

Here, we neglect the φ dependence of E_g in the argument of logarithm. At the next iteration, we put q_0 in the r.h.s. of (9) and then refine the value of q, inserting the calculated $\tilde{E}_g$ into (7):

$$\tilde{E}_g = E_g(\varphi)(1 - 1/2\sqrt{q_0}), \quad q = q_0(1 - 1/2\sqrt{q_0}). \quad (12)$$

With this q and $\tilde{E}_g$, we calculate the Coulomb correction to the current using (10)

$$I(\varphi) = I_0(\varphi)\left[1 - \frac{1}{\sqrt{q_0}}\right], \quad (13)$$

$$I_0(\varphi) = \frac{e\delta}{4\hbar} G_L G_R \log(\Delta/E_{g0})\sin\varphi. \quad (14)$$

Here, we denote current in the absence of Coulomb interaction by $I_0(\varphi)$. Suppression of the current by the Coulomb interaction becomes stronger as the phase on the junction increases. Qualitatively, the bare minigap $E_g(\varphi)$ decreases and the charging effects win the competition with proximity further suppressing the current. In the symmetric junction ($G_L = G_R$), the proximity effect vanishes completely as φ approaches π. The weak interaction approximation becomes invalid in this limit even if it is correct for small φ.

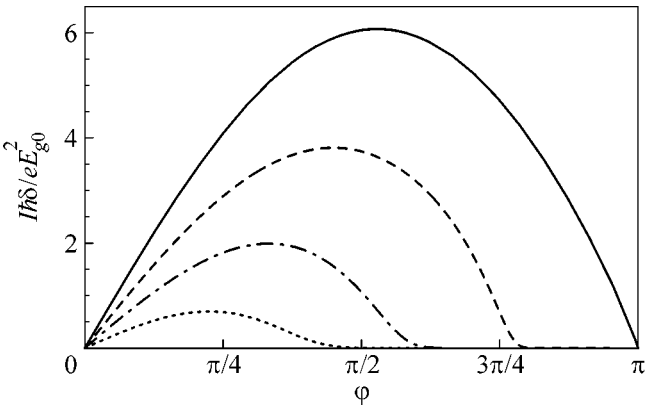

Fig. 1. Current vs. phase for the symmetric junction. Solid curve illustrates the case $E_C = 0$. It is given by expression (14). Other curves correspond to $E_C\delta/E_{g0}^2 = 0.5, 1.5, 2.5$. At small values of this parameter and at small φ, the current is given by (13). At larger φ, charging effects are always strong and the current is exponentially suppressed (16). We assume $G_L = G_R = 20$ and $\log(\Delta/E_{g0}) = 5$.

Strong Coulomb blockade. For small values of the parameter q, we calculate the ground state of (6) perturbatively: $E_0 = -E_C q^2/2(1 - N^2)$. Equations (7) and (9) give

$$\tilde{E}_g = 2\Delta\exp\left[-\frac{2E_C\delta}{E_g^2(\varphi)}(1 - N^2)\right], \quad q = \frac{2\tilde{E}_g(1 - N^2)}{E_g(\varphi)}. \quad (15)$$

Exponentially small minigap survives at $T = 0$ when Coulomb blockade is strong. Josephson current is exponentially small as well:

$$I(\varphi) = \frac{2e\delta^2 E_C \Delta^2}{\hbar E_g^4(\varphi)} G_L G_R (1 - N^2) \times \exp\left[-\frac{4E_C\delta}{E_g^2(\varphi)}(1 - N^2)\right]\sin\varphi. \quad (16)$$

We solve numerically system of equations (7), (9) and plot the dependence of the current on the phase difference in Fig. 1. Critical current $I_c = \max_\varphi I(\varphi)$ as a function of charging energy is shown in Fig. 2.

The gate voltage enhances both the minigap and the current (see Fig. 3). Large Coulomb energy makes the charge of the grain to be nearly conserving quantity. The ground state corresponds to zero charge and is separated by the gap $4E_C$ from the excited states with charge $\pm 2e$. States with odd charge are ineffective because electrons tunnel from leads by pairs. This situation changes when the gate voltage approaches $e/2C$. The gap between the ground state and excited state gets twice smaller, assisting tunneling of Cooper pairs. At

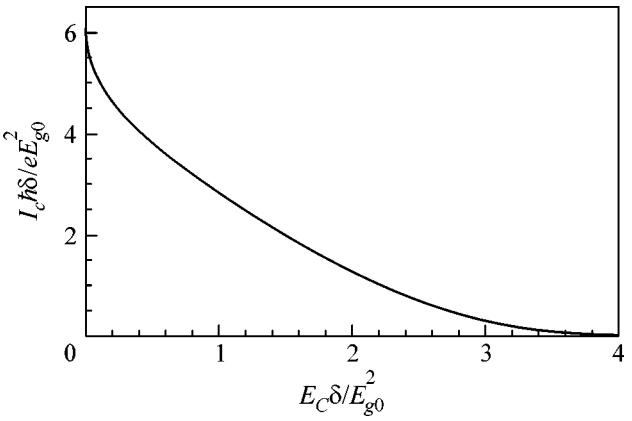

Fig. 2. The dependence of the critical current on E_C for the symmetric junction. The parameters are $G_L = G_R = 20$, $\log(\Delta/E_{g0}) = 5$.

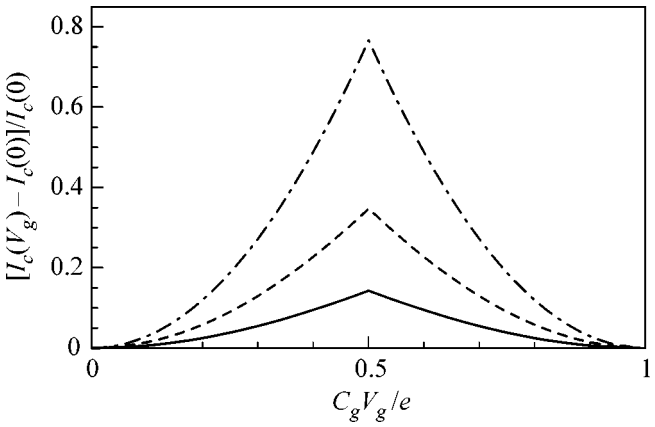

Fig. 3. Relative increase of critical current by gate voltage for $E_C\delta/E_{g0}^2$ equal to 1.5, 2, and 2.5. This effect gets stronger at larger charging energies. Other parameters of the junction are $G_L = G_R = 20$, $\log(\Delta/E_{g0}) = 5$.

higher gate voltage, the ground state carries odd charge and the critical current starts to diminish. The increase of current with gate voltage is analogous to that studied in [5], where a similar setup with the superconductive grain was considered. Now, we turn to the thermodynamic properties of the junction. The temperature dependence of the critical current is found numerically and depicted in Fig. 4. At some temperature, both the minigap and the Josephson current disappear. As temperature approaches its critical value T_c, the parameter q becomes arbitrarily small. This allows the expansion of the free energy of the K degree of freedom: $F(q, T) = F(0, T) - E_C\beta(N, T)q^2$. The coefficient $\beta(N, T)$ may be found with the help of perturbation theory for Hamiltonian (6):

$$\beta(N,T) = \frac{\sum_{-\infty}^{\infty} e^{-(n-N)^2E_C/T}/(1-(n-N)^2)}{2\sum_{-\infty}^{\infty} e^{-(n-N)^2E_C/T}} \qquad (17)$$

$$= \begin{cases} 1/[2(1-N^2)], & T \ll E_C; \\ E_C/T - (2/3)(E_C/T)^2, & T \gg E_C. \end{cases}$$

Note that β is a nonmonotonic function of temperature. At high temperature, highly excited levels of the Hamiltonian insensitive to the q perturbation play the main role. Thus, β goes to zero in this limit. At low temperature, the phase K is almost frozen at the ground state. The q term mixes two lowest excited states. As temperature grows, these two states begin to contribute to the free energy, increasing its dependence on q. When N approaches 1/2, the ground state becomes degenerate and β falls monotonically with temperature.

Expression (7) in the limit $\tilde{E}_g \ll T$ gives

$$q = \frac{E_g\tilde{E}_g}{E_C\delta}\log\frac{2\gamma\Delta}{\pi T}. \qquad (18)$$

Here, $\log\gamma \approx 0.577$ is the Euler constant. Self-consistency condition (9) in the limit of small q takes the form $\tilde{E}_g = E_g(\varphi)\beta q$. Substituting this equation into Eq. (18), we find for the critical temperature

$$T_c = \frac{2\gamma}{\pi}\Delta\exp\left[-\frac{E_C\delta}{E_g^2(\varphi)\beta(N,T_c)}\right]. \qquad (19)$$

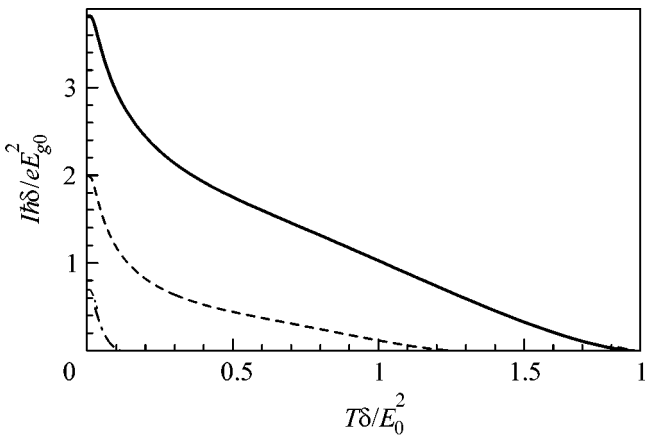

Fig. 4. Critical current vs. temperature for $E_C\delta/E_{g0}^2 = 0.5$, 1.5, 2.5. Other parameters of the junction are $G_L = G_R = 20$, $\log(\Delta/E_{g0}) = 5$.

The same equation may be obtained by the expansion of (8) in powers of $\tilde{E}_g$ and setting the coefficient of $\tilde{E}_g^2$ to zero. It can be checked that the fourth-order term of this expansion always remains positive. This justifies our assumption that $\tilde{E}_g$ vanishes continuously at the critical temperature.

In the regime of strong Coulomb interaction, critical temperature appears to be much lower than E_C. Taking low temperature asymptotic of $\beta(N, T)$, we find that $T_c = (\gamma/\pi)\tilde{E}_g(T = 0)$, where $\tilde{E}_g(T = 0)$ is given by Eq. (15). This is the BCS relation between the gap and the critical temperature. The phase of the grain strongly fluctuates and is mainly independent of the phase in the leads. The only effect of superconductive leads is a weak effective attraction in the Cooper channel which leads to formation of very weak BCS-like state.

In the opposite limit of weak Coulomb interaction, we employ high temperature asymptotic of β and find

$$T_s = \frac{E_g^2(\varphi)}{\delta}\log\frac{2\gamma\Delta\delta}{\pi E_g^2(\varphi)} - \frac{2}{3}E_C. \qquad (20)$$

The whole dependence of the critical temperature on parameters is shown in Fig. 5. It is possible that Eq. (19) has more than one solution at a given value of E_C. This implies reentrant behavior of the minigap and critical current as functions of temperature. Mathematically, it is due to nonmonotonic behavior of the function $\beta(T)$. The physical explanation is simplest in charge rather than phase representation of Hamiltonian (6). Two excited states with charge $\pm e$ have equal charging energies. Tunneling of the Cooper pair that switches between these two states is not blocked by Coulomb interaction. Finite temperature may excite the system to one of these states, leading to the temperature-assisted proximity effect and the enhancement of the minigap. Hamiltonian (6) conserves the parity of electron number. Thus, thermalization of the system implies some parity-breaking processes (e.g., single electron tunneling with energy above Δ), which may take a long time.

At large enough values of $\Delta > \Delta^* = 17.7E_g^2/\delta$, reentrant behavior of the minigap with temperature was found in some (dependent on Δ/Δ^* ratio) interval of the Coulomb parameter $E_C\delta/E_g^2$, cf. Fig. 6. Fine tuning of the parameter $E_C\delta/E_g^2$ can be achieved by an appropriate phase bias, cf. Eq. (4).

To conclude, we have described the Josephson effect in a nanoscale SINIS junction modified by the Coulomb interaction. The most important feature of SINIS structure (in comparison with usual SIS structure) is that it can demonstrate both good metallic conductance in the normal state and Coulomb blockade of Josephson current at very low temperatures, since both the conditions $G_{L,R} \gg 1$ and $E_J = \frac{\hbar}{2e} I_c \le E_C$ can be fulfilled simultaneously. We calculated the current–phase characteristic of the junction in both weak and strong Coulomb blockade limit. The enhancement of the cur-

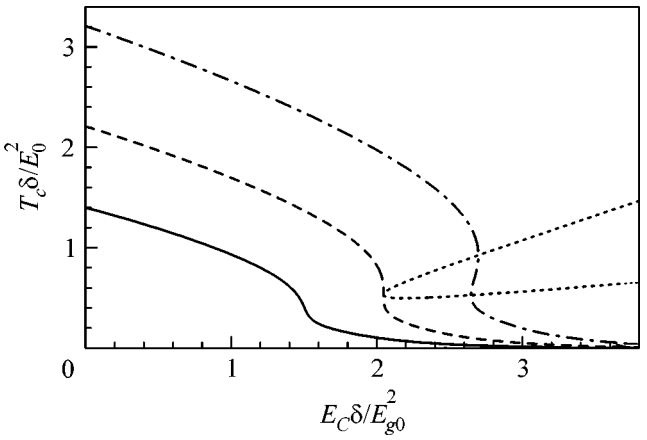

Fig. 5. The critical line demonstrating the dependence of critical temperature on E_C. The three curves are plotted for $\Delta\delta/E_g^2 = 5, 17.7, 70$. At large enough values of Δ, this dependence may not be single-valued. Dotted line shows the turning points of critical temperature. Small disk denotes the critical point where the dotted line touches the T_C vs. E_C curve. This critical point gives the following critical values: $T_c^*\delta/E_g^2 = 0.54$, $E_C^*\delta/E_g^2 = 2.05$, $\Delta^*\delta/E_g^2 = 17.7$.

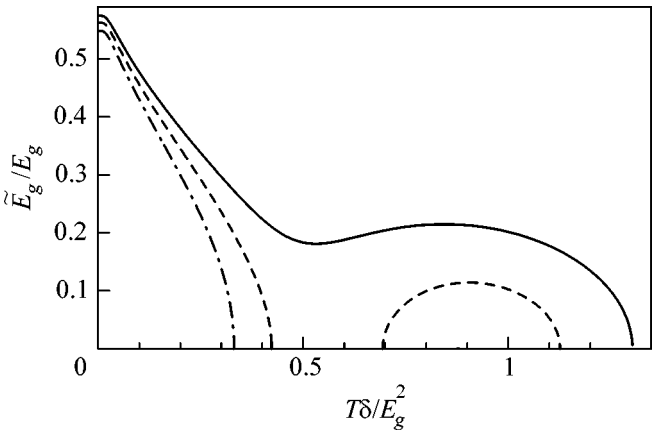

Fig. 6. The minigap in the normal dot as a function of temperature. Solid line is plotted for $E_C\delta/E_g^2 = 2.6$. Dashed line illustrates the case $E_C\delta/E_g^2 = 2.67$. Chain line is for $E_C\delta/E_g^2 = 2.75$. All curves are plotted for $\Delta = 70E_g^2/\delta$. The critical temperature as a function of E_C for the same value of Δ is shown by the chain line in Fig. 5.

rent by the gate voltage is predicted. The temperature dependence of the critical current and of the minigap induced in the normal part of the junction was found. A grain of noble metal with a size of about 50 nm connected to Nb superconductive electrodes by tunnel oxide barriers with transparency per channel of the order of 10^{-5} could present an example of the studied system with $E_J \sim E_C \sim 1K$.

We are grateful to T. Kontos and Ya. Fominov for useful discussions. This research was supported by the Program "Quantum Macrophysics" of the Russian Academy of Sciences, Russian Ministry of Science and Russian Foundation for Basic Research, grant no. 04-02-16348. P.M.O. acknowledges financial support from the Dynasty Foundation and the Landau Scholarship (KFA Juelich).

REFERENCES

1. P. M. Ostrovsky, M. A. Skvortsov, and M. V. Feigel'man, cond-mat/0311242.
2. A. I. Larkin and Yu. N. Ovchinnikov, Phys. Rev. B **28**, 6281 (1983).
3. A. M. Finkel'stein, in *Soviet Scientific Review*, Ed. by I. M. Khalatnikov (Harwood Academic, London, 1990), Vol. 14.
4. A. Kamenev and A. Andreev, Phys. Rev. B **60**, 2218 (1999).
5. L. I. Glazman, F. W. J. Hekking, K. A. Matveev, and R. I. Shekhter, Physica B (Amsterdam) **203**, 316 (1994).

JETP Letters, Vol. 79, No. 10, 2004, pp. 495–498. Translated from Pis'ma v Zhurnal Éksperimental'noĭ i Teoreticheskoĭ Fiziki, Vol. 79, No. 10, 2004, pp. 608–611.

Anisotropic Positive Magnetoresistance of a Nonplanar 2D Electron Gas in a Parallel Magnetic Field

A. V. Goran[1], A. A. Bykov[1,] *, A. K. Bakarov[1], and J. C. Portal[2]

[1] *Institute of Semiconductor Physics, Siberian Division, Russian Academy of Sciences, Novosibirsk, 630090 Russia*
**e-mail: bykov@thermo.isp.nsc.ru*
[2] *Grenoble High Magnetic Fields Laboratory, MPI-FKF and CNRS B.P.166, F-38042 Grenoble, France*
Received March 4, 2004; in final form, April 14, 2004

Magnetotransport properties of a 2D electron gas in narrow GaAs quantum wells with AlAs/GaAs superlattice barriers were studied. It is shown that the anisotropic positive magnetoresistance observed in selectively doped semiconductor structures in a parallel magnetic field is caused by the spatial modulation of the 2D electron gas.

PACS numbers: 73.63.Hs; 73.21.-b; 73.23.-b; 73.20.-r

In an idealized zero-thickness 2D electron system, the orbital motion of charge carriers is affected only by the normal component of the external magnetic field, where the magnitude of this component depends on the angle between the magnetic field $\mathbf{B}_{ext}$ and the normal to the plane of 2D electron gas. The in-plane component of magnetic field in such a system will cause changes in the spin degree of freedom of charge carriers and, hence, in the density of states of 2D electron gas. The real 2D semiconductor systems always have a nonzero thickness, and this is the cause of the orbital effect in a parallel magnetic field [1]. Unlike the magnetoresistance associated with the spin effect in a parallel magnetic field [2], the magnetoresistance caused by the finite thickness of 2D electron gas is anisotropic. The origin of this anisotropy is that the variation of the effective mass of charge carriers in the direction perpendicular to the external magnetic field is greater than the variation in the direction parallel to the field.

This anisotropy mechanism manifests itself in the dependence of the magnetoresistance of 2D electron gas on the mutual orientation of the in-plane magnetic field and the measuring current. In particular, in the situation where the measuring current is perpendicular to the in-plane magnetic field, the magnetoresistance of 2D electron gas in AlGaAs/GaAs heterojunctions is greater than in the situation where the current is parallel to the field [3]. The anisotropy of positive magnetoresistance observed in [3] was found to be much smaller than that predicted by the theory [1]. In our opinion, this discrepancy is due to the fact that 2D electron gas in real selectively doped structures not only has a finite thickness but is also nonplanar [4–7]. As will be shown below, even a very small spatial modulation of 2D electron gas, which is inherent in any real structure, also leads to the anisotropy of the positive magnetoresistance of 2D electron gas in an in-plane magnetic field. However, the magnetoresistance in this mechanism is smaller when the magnetic field and the measuring current are mutually perpendicular and greater when they are parallel. A combined effect of the finite thickness and the spatial modulation of 2D electron gas should lead to a decrease in the degree of magnetoresistance anisotropy in the in-plane magnetic field, which may qualitatively explain the experimental results obtained in [3].

In the general case, the surface of 2D electron gas can be described by the function $z = z(x, y)$ characterizing the deviation of the surface from the ideal plane formed by the x and y axes. If we decompose the vector of external magnetic field into perpendicular and parallel components, $\mathbf{B}_{ext} = \mathbf{B}_{\perp}(x, y) + \mathbf{B}_{\parallel}(x, y)$, the quantities $\mathbf{B}_{\perp}$ and $\mathbf{B}_{\parallel}$ for this surface will be functions of x and y. The perpendicular and parallel components are meant as the projections onto the normal vector and the tangential plane, respectively, at the point (x, y) of the surface of 2D electron gas.

This decomposition is helpful because, in the case of a narrow quantum well, 2D electrons perceive only the normal component that is responsible for to the appearance of classical Larmor orbits in the plane of 2D electron gas. This normal component can be considered effective inhomogeneous magnetic field $B_{eff}(x, y)$ arising as a result of applying external magnetic field to the nonplanar 2D electron gas. In the particular case of the external magnetic field parallel to the sample, the effective field will be an alternating function with zero mean: $\langle B_{eff}(x, y)\rangle = 0$ [8]. The effective magnetic field $B_{eff} = B_{eff}(x, y)$ can be calculated if we know the surface of 2D electron gas $z = z(x, y)$ and the external magnetic field $\mathbf{B}_{ext} = (B_x, B_y, B_z)$. Then, $B_{eff}(x, y) = |B_{ext}|\cos(\Theta(x, y))$, where $|B_{ext}|$ is the magnitude of the vector of external magnetic field and $\Theta(x, y)$ is the angle between the nor-

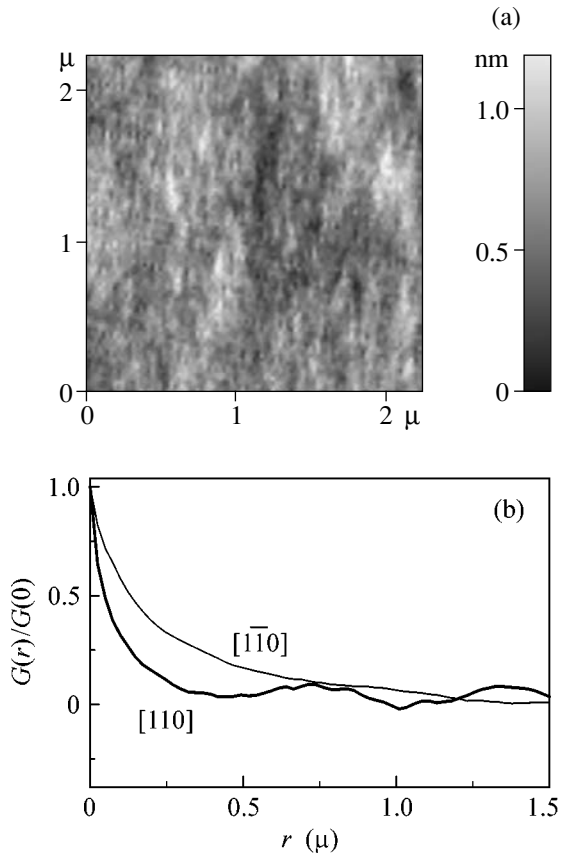

Fig. 1. (a) Two-dimensional AFM image of the surface relief of the MBE structure. (b) Autocorrelation functions of the relief in the [110] and [1$\bar{1}$0] directions.

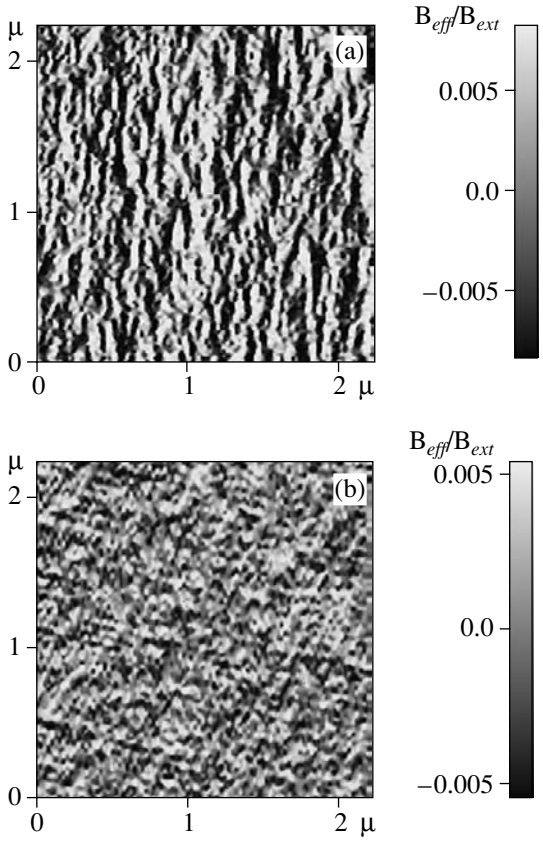

Fig. 2. Function $B_{\text{eff}}(x, y)$ calculated for a nonplanar 2D electron gas with a relief corresponding to the AFM image of the surface of MBE structure: $\mathbf{B}_{\text{ext}}$ is directed along (a) [110] and (b) [1$\bar{1}$0].

mal to the surface $z = z(x, y)$ at the point (x, y) and the vector of external magnetic field $\mathbf{B}_{\text{ext}}$.

To characterize the surface of 2D electron gas, it is convenient to introduce the autocorrelation function $G(x, y) = \int z(x - X, y - Y)z(x, y)dXdY$. If the surface is isotropic, the autocorrelation function will also be isotropic. However, the effective magnetic field B_{eff} will be anisotropic, because the external magnetic field introduces a preferential direction into the system. Thus, the analysis of the influence of the in-plane magnetic field on the 2D electron transport in heterostructures with nonplanar heteroboundaries reduces to the problem of transport in an inhomogeneous magnetic field with zero mean and a certain anisotropy. Hence, in the general case, including selectively doped MBE structures with the isotropic surface relief, the magnetoresistance of a nonplanar 2D electron gas is due to the transport in an inhomogeneous magnetic field and should depend on the angle between the direction of the measuring current and the vector of the in-plane magnetic field.

The structures studied in the experiment were selectively doped 10-nm-thick GaAs quantum wells with AlAs/GaAs superlattice barriers. They were prepared by molecular beam epitaxy (MBE) on (100) GaAs substrates whose deviation from the (100) plane did not exceed 0.02°. The surface morphology of the structures was examined by atomic force microscopy (AFM). Figure 1a shows the typical AFM image of the surface relief of the MBE structures under study. From the correlation analysis presented in Fig. 1b, one can see that the surface relief of a real MBE structure is not isotropic. The surface is wavy with a preferred [1$\bar{1}$0] orientation of the wave crests, which is typical of the selectively doped GaAs quantum wells with AlAs/GaAs superlattice barriers grown on GaAs (100) substrates [4].

Figure 2a shows a two-dimensional image of the effective magnetic field calculated for 2D electron gas on the assumption that its surface is identical to the AFM image of the MBE structure under study and that the external magnetic field is parallel to the [110] direction. One can clearly see that the effective magnetic field is anisotropic. The results of calculation of the effective magnetic field for the situation where the external magnetic field is oriented along the [1$\bar{1}$0] direction are shown in Fig. 2b. In this situation, the

anisotropy of effective magnetic field is much smaller than in the previous case. Hence, for the 2D electron gas in the selectively doped MBE structures under study, the character of $B_{\text{eff}}(x, y)$ anisotropy depends on the direction of the vector $\mathbf{B}_{\text{ext}}$.

The magnetotransport experiments were carried out at temperatures from 4.2 to 1.6 K in magnetic fields up to 15 T on L-shaped Hall bars (Fig. 3a), which were fabricated by optical lithography and liquid etching. The bars had a width of 50 μm, and the distance between the potential terminals was 100 μm. The bar orientations were chosen so that the measuring current was parallel to the [110] and $[1\bar{1}0]$ directions. The structures under study had one filled size-quantization subband. The equilibrium parameters of the 2D electron gas at $T = 4.2$ K were as follows: the concentration $n_s = 1.6 \times 10^{12}$ cm^{-2} and the mobility $\mu = 300 \times 10^3$ cm^2/V s. Figure 3b represents the results of measurements of the relative magnetoresistance for two different orientations of the parallel external magnetic field: along the x axis ($B_x = B_{\text{ext}}$ and $B_y = 0$) and along the y axis ($B_x = 0$ and $B_y = B_{\text{ext}}$). Due to the anisotropy of the surface relief, the pattern of effective magnetic field for each of these $\mathbf{B}_{\text{ext}}$ directions is different. This results in the four combinations of the 2D electron-gas magnetoresistance along the [110] and $[1\bar{1}0]$ directions. It should be noted that, in the temperature range from 4.2 to 1.6 K, the positive magnetoresistance observed in the structures under study did not vary, evidencing its classical [9, 10] rather than quantum-mechanical nature [11–13].

The anisotropy observed for the magnetoresistance of 2D electron gas can be qualitatively explained by electron scattering from the anisotropic inhomogeneous magnetic field [14] that depends on the angle between the vector $\mathbf{B}_{\text{ext}}$ and the direction of the measuring current. For the quantitative evaluation of this assumption, we carried out numerical simulation of the quasi-classical charge-carrier transport in the effective inhomogeneous magnetic field appearing in a nonplanar 2D electron gas in the parallel magnetic field. The model surfaces of the 2D electron gas were constructed using the results of AFM studies of real samples, for which the magnetic-field dependences are shown in Fig. 3b. The conductivity was calculated by the formula [15]

$$\sigma_{ij} = \frac{ne^2}{m}\int_0^\infty \langle \nu_i(0)\nu_j(t)\rangle e^{-t/\tau}dt,$$

where $\nu(t) = (\cos\varphi(t), \sin\varphi(t))$ is the direction of the electron velocity vector and τ is the charge-carrier transport relaxation time. The averaging was over 10^6 trajectories. The factor $e^{-t/\tau}$ reflects the presence of impurities from which electrons are elastically scattered.

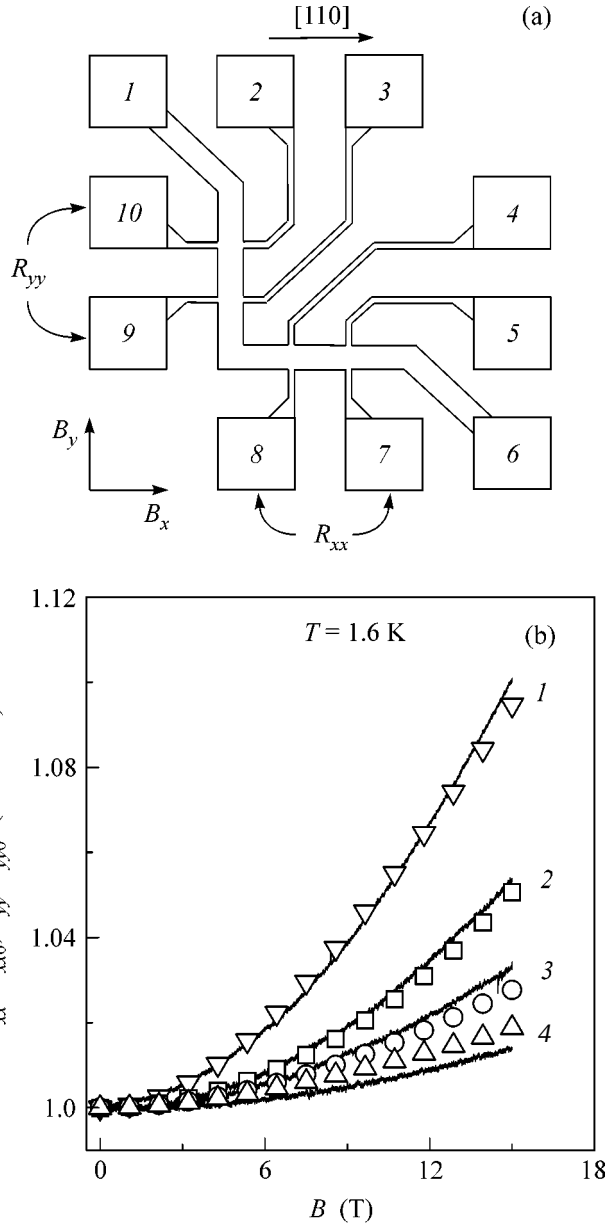

Fig. 3. (a) Schematic representation of an L-shaped Hall bar. (b) Dependences of the relative magnetoresistance of the 2D electron gas: (*1*) $R_{xx}(B_x, B_y = 0)/R_{xx0}$, (*2*) $R_{yy}(B_x = 0, B_y)/R_{yy0}$, (*3*) $R_{yy}(B_x, B_y = 0)/R_{yy0}$, and (*4*) $R_{xx}(B_x = 0, B_y)/R_{xx0}$. The solid lines represent the experimental curves, and the dots represent the calculations.

The trajectory of an electron $\mathbf{r}(t)$ was determined by the numerical integration of the equation of motion of a 2D electron in magnetic field:

$$m\dot{\mathbf{v}}(t) = -\frac{e}{c}[\mathbf{v} \times \mathbf{B}_{\text{eff}}(x, y)],$$

where $\mathbf{B}_{\text{eff}}(x, y)$ is the effective magnetic field directed normally to the sample. By analogy with the experimental configurations, two directions were preset for

the external field: along and across the [110] direction. In this way, four dependences were obtained for different combinations of R_{xx}, R_{yy} and B_x, B_y. The model parameters were taken to be equal to the parameters of the real samples (mobility, concentration, and surface relief). The only fitting parameter was the amplitude of the spatial modulation of the 2D electron gas.

The results of modeling are shown in Fig. 3b. It should be noted that the calculated amplitude of spatial modulation of the 2D electron gas proved to be 2.5 times greater than the amplitude of surface roughness obtained from the AFM studies. We explain this difference by the fact that the 2D electron gas in the MBE structure under study is at a certain distance from the sample surface, and this distance is much greater than the roughness amplitude. Therefore, in the general case, the spatial modulation of the 2D electron gas may not coincide with the surface relief. One can see that the model and experimental dependences are in good agreement with this value of the fitting parameter.

Another possible explanation of the aforementioned discrepancy is that our calculations did not take into account the influence of the finite thickness of 2D electron gas on the value of positive magnetoresistance [1]. However, we believe that the high concentration of 2D electron gas and small width of the GaAs quantum well allow us to ignore the contribution from the orbital effect to the magnetoresistance. This approximation agrees with the absence of the temperature dependence of magnetoresistance in the interval from 4.2 to 1.6 K and allows us also to exclude other quantum-mechanical mechanisms from the consideration [11–13]. The quasi-classical nature of the magnetoresistance anisotropy observed by us is confirmed not only by the functional agreement between the model and experimental curves but also by the quantitative coincidence of the relative values of magnetoresistance obtained for different combinations of the directions of measuring current and parallel magnetic field. This result allows the following conclusion to be drawn: our model adequately describes the 2D electron transport in the selectively doped MBE structures under study, and the main contribution to the magnetoresistance comes from the scattering by the effective inhomogeneous magnetic field arising in such structures in a parallel external magnetic field.

Thus, we have shown that the anisotropic positive magnetoresistance of a high-concentration 2D electron gas in a parallel magnetic field is governed by the scattering by the effective inhomogeneous magnetic field, i.e., by the spatial modulation of the 2D electron gas in the selectively doped MBE structures under study.

This work was supported by the Russian Foundation for Basic Research, project no. 04-02-16789.

REFERENCES

1. S. Das Sarma and E. H. Hwang, Phys. Rev. Lett. **84**, 5596 (2000).
2. V. T. Dolgopolov and A. Gold, Pis'ma Zh. Éksp. Teor. Fiz. **71**, 42 (2000) [JETP Lett. **71**, 27 (2000)].
3. V. S. Khrapai, E. V. Deviatov, A. A. Shashkin, and V. T. Dolgopolov, IPAP Conf. Ser. **2**, 105 (2001).
4. A. A. Bykov, A. K. Bakarov, A. V. Goran, *et al.*, Pis'ma Zh. Éksp. Teor. Fiz. **74**, 182 (2001) [JETP Lett. **74**, 164 (2001)].
5. A. K. Bakarov, A. A. Bykov, A. V. Goran, *et al.*, Phys. Low-Dimens. Semicond. Struct. **11/12**, 253 (2001).
6. A. K. Bakarov, A. A. Bykov, N. D. Aksenova, *et al.*, Pis'ma Zh. Éksp. Teor. Fiz. **77**, 794 (2003) [JETP Lett. **77**, 662 (2003)].
7. A. A. Bykov, A. K. Bakarov, A. V. Goran, *et al.*, Pis'ma Zh. Éksp. Teor. Fiz. **78**, 165 (2003) [JETP Lett. **78**, 134 (2003)].
8. A. A. Bykov, G. M. Gusev, J. R. Leite, *et al.*, Phys. Rev. B **61**, 5505 (2000).
9. I. S. Ibrahim, V. A. Schweigert, and F. M. Peeters, Phys. Rev. B **56**, 7508 (1997).
10. F. Evers, A. D. Mirlin, D. G. Polyakov, and P. Wolfe, Phys. Rev. B **60**, 8951 (1999).
11. H. Mathur and H. Baranger, Phys. Rev. B **64**, 235325 (2001).
12. G. Zala, B. N. Narozhny, and I. L. Aleiner, Phys. Rev. B **65**, 020201 (2001).
13. I. V. Gornyi and A. D. Mirlin, Phys. Rev. B **69**, 045313 (2004).
14. A. A. Bykov, G. M. Gusev, J. R. Leite, *et al.*, Phys. Rev. B **65**, 035302 (2002).
15. R. Kubo, J. Phys. Soc. Jpn. **12**, 570 (1957).

Translated by E. Golyamina

JETP Letters, Vol. 79, No. 10, 2004, pp. 499–503. Translated from Pis'ma v Zhurnal Éksperimental'noĭ i Teoreticheskoĭ Fiziki, Vol. 79, No. 10, 2004, pp. 612–617.

Measurement of the Leggett Frequency in ^{3}He-B in Aerogel

V. V. Dmitriev[1, *], V. V. Zavjalov[1], D. Ye. Zmeev[1], and N. Mulders[2]

[1] *Kapitza Institute for Physical Problems, Russian Academy of Sciences, ul. Kosygina 2, Moscow, 119334 Russia*
**e-mail: dmitriev@kapitza.ras.ru*

[2] *Department of Physics and Astronomy, University of Delaware, Newark, Delaware 19716, USA*

Received April 14, 2004

The method of measuring the Leggett frequency of ^{3}He-B using spatially homogeneous oscillations of a homogeneously precessing domain was developed. The temperature dependence of Leggett frequency was measured for bulk ^{3}He-B and ^{3}He-B in aerogel at a pressure of 19.5 bar. © *2004 MAIK "Nauka/Interperiodica".*

PACS numbers: 67.57.-z; 76.60.-k

1. INTRODUCTION

The investigation of ^{3}He in a low-density aerogel allows the experimental study of the influence of impurities on the superfluidity of a system with nontrivial Cooper pairing. Aerogel consists of SiO_2 strands with a diameter of ~30 Å and a characteristic distance of 500 Å between the strands (hereafter, we deal with so-called 98% aerogel, i.e., an aerogel in which 98% of the volume is free and with which most experiments have been carried out). Since the strand diameter is much smaller than the coherence length in a superfluid ^{3}He, they play the role of extended impurities.

If an aerogel is filled with pure ^{3}He, NMR is distinctly affected by two solid monolayers of paramagnetic ^{3}He covering the strand surface. With lowering temperature, their magnetic moment increases, and at temperatures on the order of 1 mK, it exceeds several times the magnetic moment of a liquid ^{3}He filling the aerogel. To circumvent this effect, a small amount of ^{4}He is first added into a cooled cell with aerogel to cover the aerogel strands with two ^{4}He monolayers, and only after this the cell is filled with ^{3}He. In this case, the NMR signal is determined only by the liquid ^{3}He. It is known that the presence of ^{4}He at the strand surface does not affect the phase diagram of ^{3}He superfluid states in aerogel. All the experiments discussed below were performed in an aerogel preliminary covered with ^{4}He.

It is known that two superfluid phases arise at ultralow temperatures in a ^{3}He in aerogel, one of which is analogous to the B phase of bulk (i.e., without aerogel) ^{3}He [1–3]. The Leggett frequency Ω_B that characterizes the strength of dipole–dipole interaction between atoms in a Cooper pair is an important parameter of the B phase because it allows the estimation of the value of energy gap. The purpose of this work was to develop the method of measuring the Leggett frequency for ^{3}He-B in aerogel and carry out such measurements.

The Leggett frequency for bulk ^{3}He-B was determined by various methods: by measuring the transverse cw NMR line shape, the longitudinal NMR frequency, etc. [4–6]. To determine the Leggett frequency by these methods, it is necessary to know the spatial distribution (texture) of the ^{3}He-B order parameter in an experimental cell. For example, in the case of transverse NMR, the Leggett frequency can be determined from the absorption line shape. At equilibrium, the order-parameter vector **n** is parallel to the external magnetic field **H** only far from the cell walls. This orientation corresponds to the Larmor NMR frequency. Near the walls oriented along **H**, the angle between **n** and **H** is ≈63° and the NMR frequency changes. As a result, the transverse NMR line shape consists of a sharp peak at the Larmor frequency ω_L and a long "tail" extended to high frequencies and terminated at the frequency $\omega = \omega_L + 2\Omega_B^2/5\omega_L$.

The use of standard NMR methods for ^{3}He-B in aerogel is hampered because the main orienting action on the texture comes from the local aerogel inhomogeneities. This is illustrated in Fig. 1, where two transverse cw NMR signals recorded in two different cells with ^{3}He-B in aerogel at the same temperature are shown (the scheme of the experimental chamber containing two cells is shown in [3]). Both cells were shaped like a cylinder (5.3 mm in diameter and 5.6 mm in height) with the axis oriented along the external magnetic field. One of the cells was almost fully filled with aerogel, while the aerogel in another cell had the form of a ≈2.4-mm-thick disk placed in the middle of the experimental volume. The samples were prepared by the same technique, and the ^{3}He superfluid transition temperature in these samples was the same (at P =

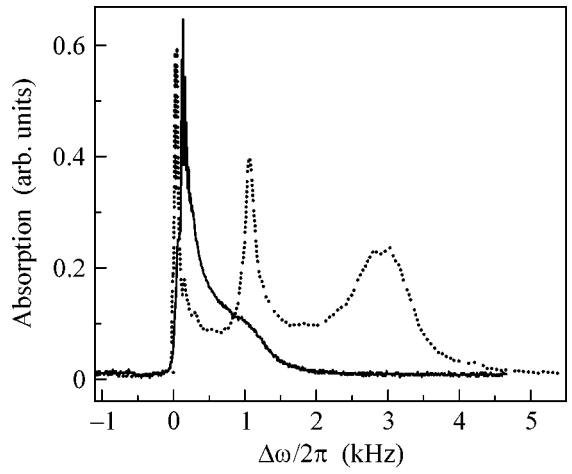

Fig. 1. Absorption signals obtained under the same conditions by standard cw NMR in two different cells (see text). Dots: cell is filled with aerogel in the form of a 2.4-mm-thick disk. Solid line: cell is almost fully filled with aerogel. $T = 0.76T_{ca}$; $P = 25.5$ bar; and $H = 284$ Oe.

25.5 bar, $T_{ca} \approx 0.76T_c$, where T_c and T_{ca} are the superfluid transition temperatures for bulk ^{3}He and for ^{3}He in aerogel, respectively). It is seen from the figure that not only the NMR line widths but also the line shapes are noticeably different in these cells. It is worth noting that the signal from the cell partially filled with aerogel is almost the same as for ^{3}He in aerogel (except for a narrow region near the Larmor frequency), while a high-frequency tail from bulk ^{3}He-B has a much smaller amplitude and terminates far beyond the picture. This follows from the fact that the line narrows monotonically but, on the whole, retains its shape with a rise in temperature, and only a narrow peak remains in the region of Larmor frequency at $T = T_{ca}$. The tail corresponding to ^{3}He-B becomes detectable only upon further rise in temperature.

It is known that a homogeneously precessing two-domain structure (homogeneously precessing domain (HPD) [7]) can arise in bulk ^{3}He-B in a magnetic field with a uniform gradient. One of these domains is a region with an almost equilibrium magnetization, while the magnetization in the other is tilted by an angle β slightly exceeding $\Theta_0 = \arccos(-1/4) \approx 104°$ and undergoes the in-phase precession over all volume. In this case, the vector **n** deflects from **H** by an angle of 90° and also precesses uniformly in volume. The precession frequency is equal to the Larmor frequency in the domain wall, whose characteristic thickness is equal to 0.2–0.3 mm. The local frequency shift from the Larmor frequency is due to the dipolar frequency shift that arises in ^{3}He-B if the magnetization deflects by an angle larger than Θ_0. If a uniform magnetic-field gradient is applied to the sample in the **H** direction (z axis), an HPD arises upon a gradual decrease in the spatially homogeneous component of external field in the case of transverse cw NMR with a sufficiently high rf amplitude h [8]. In this case, HPD can be maintained as long as one likes, because the magnetic relaxation is compensated by the rf power.

An HPD can also be created in the B phase of ^{3}He in aerogel [3]. In this case, HPD does not differ from an HPD in bulk ^{3}He-B and has a homogeneous texture in a ^{3}He-B sample in aerogel as well. Against the background of precession, various oscillation modes of the precessing HPD magnetization can be excited. To date, two types of spatially inhomogeneous HPD oscillations have been studied both theoretically and experimentally: torsional oscillations [9] and domain-wall-shape oscillations [10]. The torsional frequency depends on the HPD length, the cell geometry, the Leggett frequency, and the spin-wave velocity. If the latter is known, this mode, in principle, can be used to determine the Leggett frequency. However, it will be shown below that the spatially homogeneous HPD modes are much more suitable for this purpose.

2. SPATIALLY HOMOGENEOUS HPD OSCILLATIONS

Two spatially homogeneous HPD modes were theoretically predicted in [11], where the oscillations in ^{3}He-B were considered on the background of stationary precession with various magnetization tipping angles. It was shown that, for $\beta \geq \Theta_0$, two oscillation modes are possible. In the rotating system of coordinates, the frequencies of these modes are given by the following expressions:

$$\Omega_1^2 = \omega_L^2 + \Omega_B^2, \tag{1}$$

$$\Omega_2^2 = \frac{3}{8}\omega_L\Delta\omega, \tag{2}$$

where $\Delta\omega$ is the precession-frequency shift from the Larmor value. In [11], the rf field was absent. We carried out calculations for the case where the rf amplitude is nonzero and $\beta \geq \Theta_0$, which corresponds to the rf-maintained HPD. It turned out that, if the relation $\Delta\omega \gg \gamma h\Omega_B^2/\omega_L^2$ holds (which was always fulfilled in our experiments), one more oscillation mode arises with a frequency determined by the following expression [12]:

$$\Omega_3^2 = \frac{4}{\sqrt{15}}\frac{h}{H}\frac{\Omega_B^2}{1+\frac{8}{3}\left(\frac{\Omega_B}{\omega_L}\right)^2}. \tag{3}$$

At first sight, the first and third of the aforementioned modes are ideally suited for measuring the Leggett frequency. To check this, we performed numerical simulation of the experiment on the excitation and maintaining HPD oscillations by a cw rf field. To this end, a complete set of Leggett–Takagi equations was solved for the one-dimensional case with allowance for

the dissipation and the presence of superfluid spin currents (spin supercurrents). The boundary conditions corresponded to the absence of spin flux at both boundaries. The simulation was as close to the real experiment as possible: a uniform gradient of the external magnetic field and a weakly spatially nonuniform rf field were applied to the ^{3}He sample, and the HPD in the cell was formed through reducing the spatially homogeneous magnetic-field component. After the HPD completely filled the cell, the field did not change and the HPD was disturbed from equilibrium by some pulsed action or by an additional cw pumping with a frequency changed in a certain range near Ω_1 or Ω_3. It turned out that, in practice, the Ω_1 mode cannot be excited because it is strongly damped. Quite the reverse, the Ω_3 oscillations can easily be excited and are weakly damped, and their frequency coincides with Eq. (3). In the rotating system of coordinates, these modes correspond to the oscillations of precession phase about the equilibrium position. Numerical simulation suggests that the following excitation method is optimal for this mode: oscillations are excited after a jump change in **H** by a small value $\delta H \sim 10$–100 mOe.

3. EXPERIMENTAL

Experiments were carried out at a pressure of 19.5 bar in a magnetic field of 285 Oe (the corresponding NMR frequency is 923 kHz). The experimental chamber (Fig. 2) was mounted at the nuclear demagnetization stage and contained two cylindrically shaped cells (each ~5.25 mm in diameter and 1.75 mm in height) fabricated from Stycast-1266 epoxy resin. A transceiver NMR coil with the axis oriented perpendicular to the external field **H** was placed outside each cell. In addition, each cell was surrounded by a separate longitudinal coil (not shown in Fig. 2) to produce a jump change in the homogeneous component of the external field (the axes of these coils were aligned with **H**). All coils were thermally insulated from the cells. Cell 1 did not contain aerogel, and aerogel in cell 2 had the form of a disk with a diameter of 5 mm and a thickness of ≈1.53 mm and was placed in the center of the experimental volume. The HPD signal induced in the corresponding transceiver coil was amplified by a preamplifier and fed into a lock-in SR844 (Stanford Research Systems) amplifier that extracted the absorption and dispersion signals, after which they were read in a computer memory. The required temperature was achieved using a nuclear-demagnetization cryostat and monitored by a platinum NMR thermometer and a vibrating wire placed in a separate volume (below the experimental cells). The experimental cells were connected to this volume through a channel with a waist of diameter 1 mm and length of 2.5 mm.

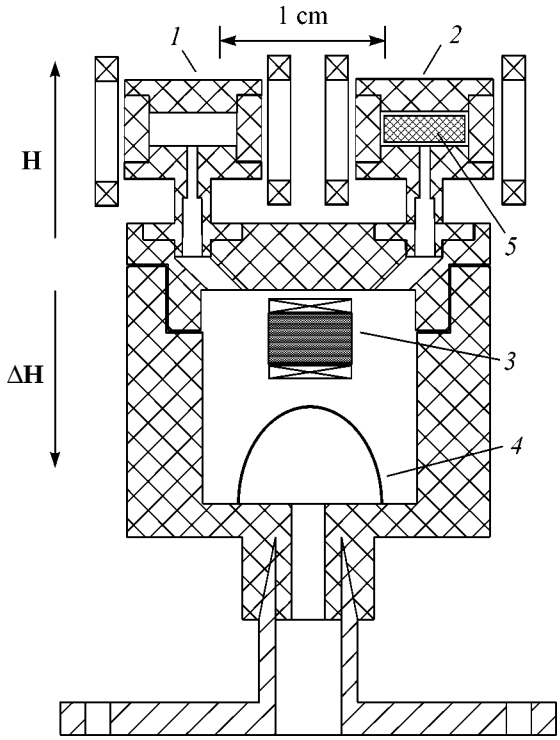

Fig. 2. Scheme of the experimental chamber: (*1*) cell 1; (*2*) cell 2; (*3*) platinum NMR thermometer; (*4*) vibrating wire; and (*5*) aerogel.

4. EXPERIMENTS WITH BULK ^{3}He-B

An HPD was "grown" in cell 1 by the cw NMR method through lowering the field **H**. The field ceased to change when the cell was fully filled with the HPD and the minimal frequency shift in the cell was sufficiently large for the condition $\Delta\omega \gg \gamma h \Omega_B^2/\omega_L^2$ to be met (the frequency shift varied along the cell because of the applied field gradient). Then, a rectangular current pulse with a duration of a few tenths of a second corresponding to a change of 10–50 mOe in the external field was fed into the corresponding longitudinal coil. The time constant of the lock-in amplifier was chosen to be small (ordinarily, 30 μs), so that the possible low-frequency HPD oscillations were detected without distortion. It turned out that, indeed, this procedure gave rise to weakly damped oscillations, whose amplitude was larger at the channel corresponding to the absorption signal. For the convenience of signal processing, the phase of reference signal from the lock-in amplifier was tuned so that the oscillations were observed only at one of the channels. The result of one of these experiments is demonstrated in Fig. 3. At $t = 0$, a current pulse corresponding to $\delta H \sim 50$ mOe was applied to the longitudinal coil. The excited oscillations were damped with a characteristic time on the order of 100 ms. The oscillations were also excited upon switching off the additional field. It was found that, in accordance with

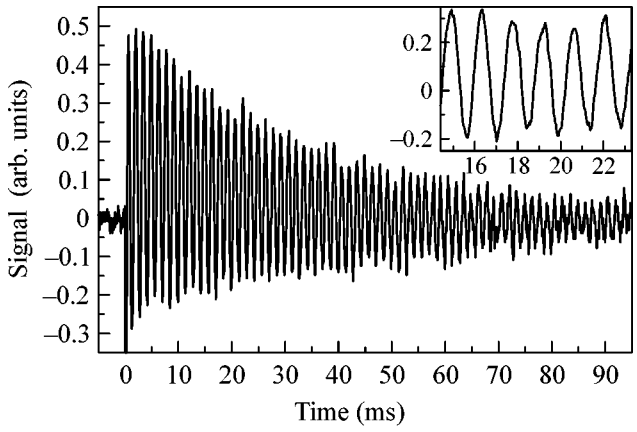

Fig. 3. Oscillations of the NMR signal from ^{3}He-B in cell 1 after applying a pulse to the longitudinal coil.

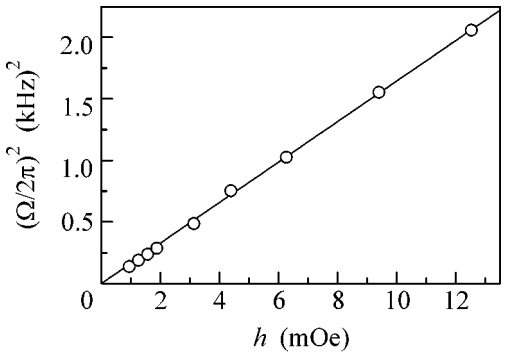

Fig. 4. Oscillation frequency as a function of the amplitude of the rf field maintaining HPD in cell 1. $T \sim 0.61T_c$. The rf amplitude was calibrated in a uniform magnetic field in the normal phase of ^{3}He through applying a long (on the order of 1 ms) rf pulse and measuring the initial free-induction amplitude as a function of the pulse amplitude.

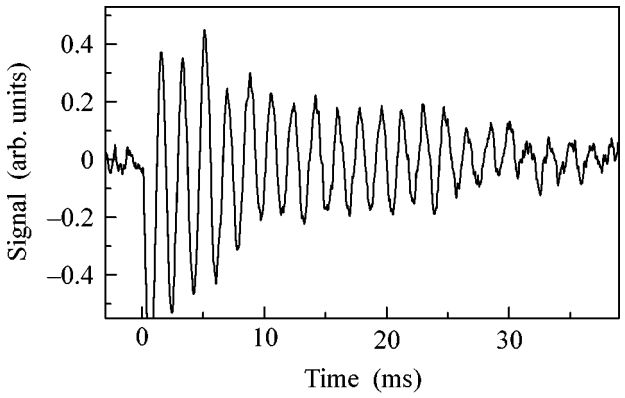

Fig. 5. Oscillations of the NMR signal from ^{3}He-B in aerogel in cell 2 after applying a pulse to the longitudinal coil.

Eq. (3), the oscillation frequency was independent of the frequency shift and proportional to the square root of the effective rf amplitude (Fig. 4); i.e., this method can be used to excite the spatially homogeneous HPD mode (3).

5. EXPERIMENTS WITH ^{3}He IN AEROGEL

The superfluid transition temperature of ^{3}He in aerogel at a pressure of 19.5 bar was found to be $0.795T_c$. The experiments with cell 2 were carried out exactly in the same manner as in bulk ^{3}He, and mode (3) was also easily excited by a pulse applied to the longitudinal coil (Fig. 5). The frequency of the resulting oscillations was also independent of the frequency shift and proportional to the square root of the effective rf amplitude.

6. MEASUREMENTS OF THE LEGGETT FREQUENCY

The amplitude of the HPD-maintaining rf field can easily be calibrated in the normal ^{3}He phase. After the subsequent measurement of the oscillation frequency, one can use Eq. (3) for determining the Leggett frequency. The results of these measurements in both bulk ^{3}He (cell 1) and ^{3}He in aerogel (cell 2) are shown in Fig. 6. The solid curve in Fig. 6 corresponds to the Leggett frequency measured in [4] by the standard cw NMR in bulk ^{3}He and interpolated to a pressure of 19.5 bar. The good agreement between these data and our results is evidence that the method developed by us for measuring the Leggett frequency is quite efficient.

It is worthy of note that, when interpreting the measurement results for aerogel, one should take into account that the sample can be overheated due to a low heat conductivity of ^{3}He in aerogel. To reduce this overheating, the thickness of our aerogel sample was small, and gaps (~0.12 mm) were left between the sample and the cell walls to remove the heat that was released in the HPD due to the magnetic relaxation. The heat power released in the cell did not exceed 0.5 nW, as was estimated from the known rf amplitude and the measured absorption-to-dispersion ratio of the HPD signal. The maximal sample overheating for such a heat release can be estimated using the data on aerogel thermal conductivity [13, 14]. For our geometry, this estimate gives an acceptable value of no higher than $0.003T/T_{ca}$. However, in the presence of gaps, the fraction of bulk helium in cell 2 comprises 18% of the cell volume. It follows from [3] that the HPD in the cell containing aerogel and bulk ^{3}He fills both the aerogel and the volume free from aerogel. The Leggett frequency in bulk ^{3}He differs from its value in aerogel. As a result, the situation of two coupled oscillators arises. The frequencies of coupled oscillators depend on their eigenfrequencies and on the corresponding coupling parameters. In our case, the spin-wave velocities (determining the gradient energy and the spin supercurrents) are such parameters. We

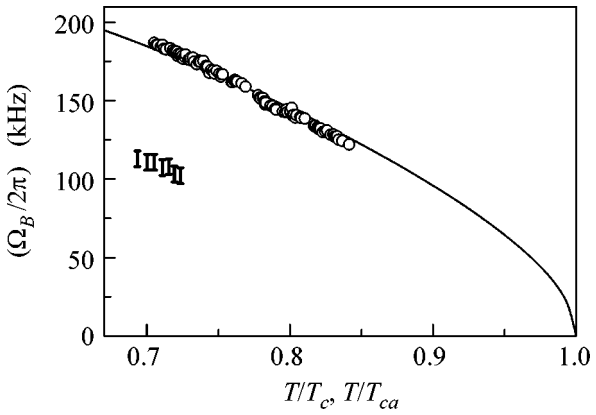

Fig. 6. Temperature dependence of the Leggett frequency in (circles) bulk ^{3}He-B and (vertical bars) ^{3}He-B in aerogel (in units of T/T_c and T/T_{ca}, respectively), as measured at P = 19.5 bar using the spatially homogeneous HPD oscillations (mode (3)). Solid curve corresponds to the Leggett frequency measured for bulk ^{3}He in [4] and interpolated to a pressure of 19.5 bar.

have carried out the numerical simulation of our experiment, in which the aerogel (a region where the Leggett frequency, the spin-wave velocities, and the magnetic-relaxation parameters differ from their values in bulk ^{3}He) was situated between two regions of bulk ^{3}He. It was found that the observed oscillation frequency is determined only by the aerogel filling factor in the cell and by the frequencies of mode (3) in bulk ^{3}He and in ^{3}He in aerogel. It is independent of the spin-wave velocities and magnetic-relaxation parameters over a wide range of their values (that far exceeds their possible range!). The oscillation frequency is determined, to a greater extent, by the part of the cell where the Leggett frequency is lower (i.e., by the region filled with aerogel). In our experiments, the filling factor was equal to 0.82. In this case, the oscillation frequency is 8% higher than the value calculated by Eq. (3) on the assumption that the cell is fully filled with aerogel. Accordingly, the Leggett frequencies of ^{3}He in aerogel are indicated in Fig. 6 by the vertical bars, with the upper end of each bar corresponding to the value obtained by the direct recalculation of the measured oscillation frequency and the lower end corresponding to the value obtained with the indicated correction.

The energy gap in the spectrum of ^{3}He-B excitations should be proportional to the Leggett frequency and inversely proportional to the square root of magnetic susceptibility [15]. Our results and the known value of magnetic susceptibility (which can be estimated from [1]) yield $\Delta_a = (0.53 \pm 0.02)\Delta$, where Δ_a and Δ are the gaps in ^{3}He in aerogel and in bulk ^{3}He at temperatures corresponding to the same ratio to T_{ca} and T_c, respectively. This value agrees with the results of acoustic measurements [16] and with the estimates obtained from the standard cw NMR experiments [1].

7. CONCLUSIONS

As a result of our studies, a new method has been developed for measuring the Leggett frequency in the B phase of superfluid ^{3}He. The method was used to measure the Leggett frequency in ^{3}He-B in aerogel.

We are grateful to I.V. Kosarev for assistance at the initial stage of experiments and to I.A. Fomin for discussions. This work was supported by the Russian Foundation for Basic Research (project no. 03-02-17017) and the Ministry of Education and Science of the Russian Federation. D.E. Zmeev is grateful to the Landau Scholarship Program for financial support.

REFERENCES

1. B. I. Barker, Y. Lee, L. Polukhina, *et al.*, Phys. Rev. Lett. **85**, 2148 (2000).
2. G. Gervais, T. M. Haard, R. Nomura, *et al.*, Phys. Rev. Lett. **87**, 035701 (2001).
3. V. V. Dmitriev, V. V. Zav'yalov, D. E. Zmeev, *et al.*, Pis'ma Zh. Éksp. Teor. Fiz. **76**, 371 (2002) [JETP Lett. **76**, 312 (2002)].
4. P. J. Hakonen, M. Krusius, M. M. Salomaa, *et al.*, J. Low Temp. Phys. **76**, 225 (1989).
5. A. I. Ahonen, M. Krusius, and M. A. Paalanen, J. Low Temp. Phys. **25**, 421 (1976).
6. D. D. Osheroff, Phys. Rev. Lett. **33**, 1009 (1974).
7. A. S. Borovik-Romanov, Yu. M. Bun'kov, V. V. Dmitriev, *et al.*, Zh. Éksp. Teor. Fiz. **88**, 2025 (1985) [Sov. Phys. JETP **61**, 1199 (1985)]; I. A. Fomin, Zh. Éksp. Teor. Fiz. **88**, 2039 (1985) [Sov. Phys. JETP **61**, 1207 (1985)].
8. A. S. Borovik-Romanov, Yu. M. Bun'kov, V. V. Dmitriev, *et al.*, Zh. Éksp. Teor. Fiz. **96**, 956 (1989) [Sov. Phys. JETP **69**, 542 (1989)].
9. Yu. M. Bun'kov, V. V. Dmitriev, and Yu. M. Mukharskiĭ, Pis'ma Zh. Éksp. Teor. Fiz. **43**, 131 (1986) [JETP Lett. **43**, 168 (1986)]; I. A. Fomin, Pis'ma Zh. Éksp. Teor. Fiz. **43**, 134 (1986) [JETP Lett. **43**, 171 (1986)].
10. Yu. M. Bunkov, V. V. Dmitriev, and Yu. M. Mukharsky, Physica B (Amsterdam) **178**, 196 (1992).
11. I. A. Fomin, Zh. Éksp. Teor. Fiz. **84**, 2109 (1976) [Sov. Phys. JETP **57**, 1227 (1976)].
12. V. V. Dmitriev, V. V. Zavjalov, and D. Ye. Zmeev, in *Proceedings of International Symposium on Quantum Fluids and Solids, QFS2004* (2004), J. Low Temp. Phys. (in press).
13. B. I. Barker, L. Polukhina, J. F. Poco, *et al.*, J. Low Temp. Phys. **113**, 635 (1998).
14. S. M. Fisher, A. M. Guenault, A. J. Hale, and G. R. Pickett, J. Low Temp. Phys. **126**, 673 (2002).
15. A. J. Leggett, Ann. Phys. (N.Y.) **85**, 11 (1974).
16. G. Lawes and J. M. Paria, Phys. Rev. B **65**, 092511 (2002).

Translated by V. Sakun

JETP Letters, Vol. 79, No. 10, 2004, pp. 504–509. From Pis'ma v Zhurnal Éksperimental'noĭ i Teoreticheskoĭ Fiziki, Vol. 79, No. 10, 2004, pp. 618–623.

Charge Redistribution between Cyclotron-Resolved Edge States at High Imbalance¶

E. V. Deviatov[1,*], V. T. Dolgopolov[1], and A. Würtz[2]

[1] *Institute of Solid State Physics, Russian Academy of Sciences, Chernogolovka, Moscow region, 142432 Russia*

** e-mail: dev@issp.ac.ru*

[2] *Laboratorium für Festkörperphysik, Universität Duisburg-Essen, D-47048 Duisburg, Germany*

Received April 15, 2004

We use a quasi-Corbino sample geometry with independent contacts to different edge states in the quantum Hall effect regime to investigate a charge redistribution between cyclotron-split edge states at high imbalance. We also modify the Büttiker formalism by introducing local transport characteristics in it and use this modified Büttiker picture to describe the experimental results. We find that charge transfer between cyclotron-split edge states at high imbalance can be described by a single parameter, which is a transferred between edge states portion of the available for transfer part of the electrochemical potential imbalance. This parameter is found to be independent of the particular sample characteristics, describing fundamental properties of the interedge-state scattering. From the experiment we obtain it in the dependence on the voltage imbalance between edge states and propose a qualitative explanation to the experimental findings. *© 2004 MAIK "Nauka/Interperiodica".*

PACS numbers: 73.43.Fj

Just from the beginning of the quantum Hall investigations, it was understood that edge states play a significant role in many transport phenomena in the quantum Hall effect regime [1]. In a quantizing magnetic field the edge potential bends up the energy levels near the sample edges. At the intersections of the energy levels with the Fermi level, edge states are formed. It was a paper of Büttiker [2] that proposed a formalism for the Hall resistance calculation regarding a transport through edge states. This model was further developed by Chklovskii *et al.* [3] for electrostatically interacting electrons. The interaction modifies one-dimensional Büttiker edge states into strips of incompressible electron liquid of finite widths. It was shown theoretically [2] and confirmed in experiments [4] that quantum Hall resistance is not sensitive to the interedge-channel scattering. Nevertheless, the properties of this scattering can be investigated by using the selective edge channel population methods.

Most experiments have been performed in the Hall-bar geometry by using the cross gate technique [4]. These experiments have revealed the interedge-scattering dependence on the magnetic field, temperature and filling factor [4]. In the Hall-bar geometry, the experiments are at low imbalance conditions, when the energy difference between edge states is smaller than the spectral gaps. An attempt to increase the edge states imbalance by closing cross gates dramatically decreases the experimental accuracy, as was mentioned in [5].

Another experimental method is the use of the quasi-Corbino sample geometry [6, 7]. In this geometry two nonconnecting etched edges are formed in the sample. A cross gate is used to redirect some edge states between etched edges and to define an interaction region at one edge. Because the interacting edge states originate from different edges of the sample, they are independently contacted and direct interedge-scattering investigations become possible at any imbalance between edge states. This imbalance is controlled by the applied voltage, and in dependence of its sign, the edge potential profile between edge states becomes stronger or flatter. In the latter case, at some voltage imbalance, the potential barrier between edge states disappears, leading to a steplike behavior of the corresponding branch of the *I–V* curve. This effect opens a path to use the quasi-Corbino geometry for spectroscopic investigations at the sample edge. Recently, the quasi-Corbino geometry was used to investigate the edge spectrum of single- [7] and double-layer [8] two-dimensional electron structures. It was also understood that, in the transport between spin-resolved edge states at high imbalance (i.e., higher than the spectral gaps), nuclear effects become important [9].

When developed, Büttiker formalism was intended to describe a high accuracy of the sample resistance quantization in the quantum Hall effect regime. For this reason, it depicts the interedge scattering by integral sample characteristics practically as scattering between ohmic contacts. This picture becomes inconvenient

¶ This article was submitted by the authors in English.

while describing a charge transfer between edge states at high imbalance, where the scattering by *definition* takes place on small lengths, much smaller than the sample size.

Here, we investigate a charge transfer between cyclotron-split edge states at high imbalance. We modify Büttiker formalism by introducing local transport characteristics in it. We find that charge transfer can be described by a single parameter, which is the transferred portion of the available for the transfer part of the electrochemical potential imbalance. This modified Büttiker picture is used to describe details of charge transfer while current is overflowing between edge channels.

Our samples are fabricated from a molecular beam epitactically-grown GaAs/AlGaAs heterostructure. It contains a two-dimensional electron gas (2DEG) located 70 nm below the surface. The mobility at 4 K is 800000 cm^2/V s, and the carrier density 3.7×10^{11} cm^{-2}. Samples are patterned in a quasi-Corbino geometry [7], see Fig. 1. Rectangular mesa has an etched region inside. Ohmic contacts are made to both (inner and outer) edges of the sample. A Shottky gate is patterned around the inner etched area, leaving an uncovered T-shaped region between inner and outer edges. This region forms a narrow (about several microns) strip of uncovered 2DEG near the outer edge of the sample which is called gate gap. Here, we present data from the sample with 5 μm gate-gap width, while 2-, 10-, and 20-μm gate-gap samples are also investigated, showing identical experimental results.

In our experimental setup, one of the inner contacts is always grounded. In a quantizing magnetic field, at filling factors ν = 3, 4, we deplete 2DEG under the gate to a smaller filling factor $g = 2$, redirecting cyclotron-split ν–g edge states from inner to outer edges of the sample. We apply a dc current to one of the outer contacts and measure a dc voltage drop between two others inner and outer contacts at a temperature of 30 mK. By switching current and voltage contacts *I–V,* traces for four different contact combinations can be investigated. Because of independent ohmic contacts to the cyclotron-split edge states, the measured voltage U is connected to the voltage drop V between edge states in the gate gap, which is directly the energy shift eV between them. For example, $U = V$ for contact combination at which contacts 4 and 2 are current contacts and *3* and *1* are voltage ones, as denoted in Fig. 1.

Examples of experimental *I–V* curves are presented in the insets to Figs. 2 and 3 for two groups of cyclotron-split edge states. While increasing the current from zero to positive values, the measured voltage rises abruptly to some value V_{th}. There is practically no current before $V = V_{th}$, but after it, the voltage is a roughly linear function of the current. This linear law is valid for hundreds of nanoAms, see main Figs. 2 and 3, up to our highest applied currents for filling factor combination ν = 4, $g = 2$. For ν = 3, $g = 2$, at high currents, there is a strong deviation from the linear law. The deviation starts from twice the onset voltage $2V_{th}$ and leads to increasing resistance in respect to the linear dependence. It cannot be due to overheating of the sample by

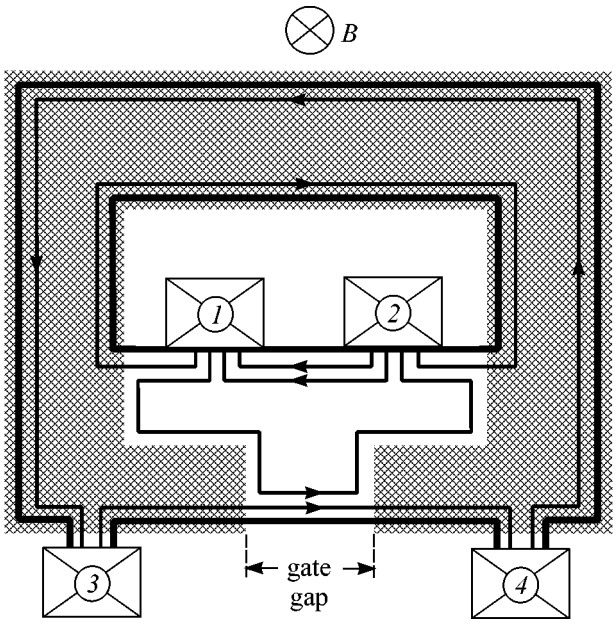

Fig. 1. Schematic diagram of the pseudo-Corbino sample geometry. Contacts are positioned along the etched edges of the ring-shaped mesa (thick outline). The shaded area represents the Schottky gate. Arrows indicate the direction of electron drift in the edge states.

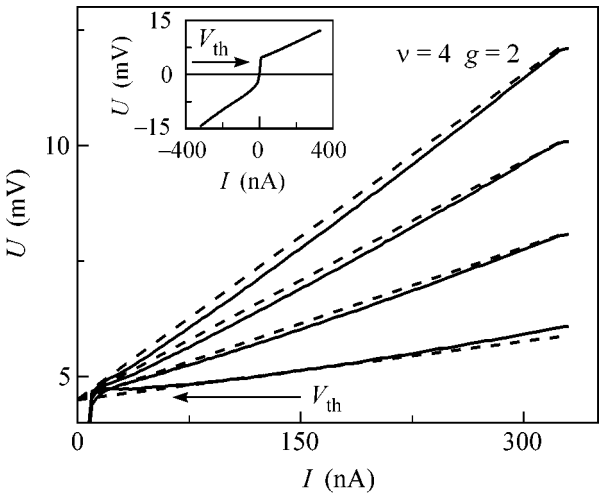

Fig. 2. Positive branches of experimental *I–V* curves for filling factors ν = 4, $g = 2$ for different contact configurations. They are (from up to down) current (4–2), voltage (3–1); (4–1), (3–2); (3–2), (4–1); (3–1), (4–2) as depicted in Fig. 1. The inset shows an example of the experimental *I–V* curve in a whole sweeping range with marked threshold position. $V_{th} = 4.5$ mV. The magnetic field is $B = 3.9$ T.

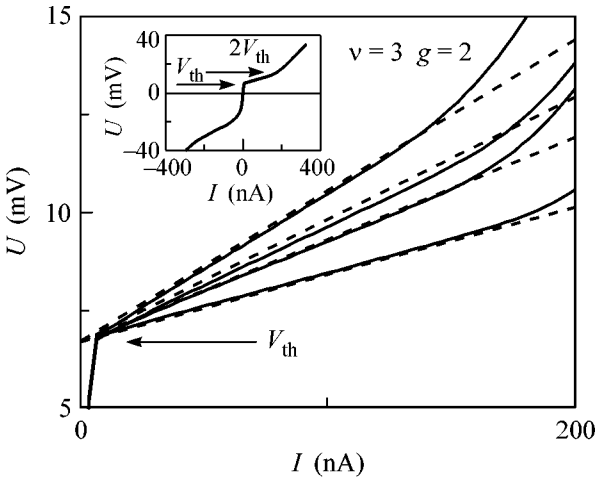

Fig. 3. Positive branches of experimental *I–V* curves for filling factors $\nu = 3$, $g = 2$ for different contact configurations. They are (from up to down) current (4–2), voltage (3–1); (4–1), (3–2); (3–2), (4–1); (3–1), (4–2) as depicted in Fig. 1. The inset shows an example of the experimental *I–V* curve in a whole sweeping range with marked threshold and twice threshold positions. $V_{th} = 6.7$ mV. The magnetic field is $B = 5.1$ T.

the current, because it would diminish the resistance, in contradiction with the experiment, see Fig. 3.

In Figs. 2 and 3, positive *I–V* branches are shown for four different contact combinations. As can be seen from the figure, there is still small nonlinearity of the curves. The behavior described above is valid for all of them and is very reproducible from sample to sample and in cooling cycles. Positive branches start from the same threshold voltage, which is fixed for a given filling factor combination. The threshold voltage values are close to the cyclotron splitting in the corresponding field but smaller by approximately 2 mV, see [7]: $V_{th} = 4.5$ mV for $\nu = 4$, $g = 2$ ($\hbar\omega_c = 6.7$ meV) and $V_{th} = 6.7$ mV for $\nu = 3$, $g = 2$ ($\hbar\omega_c = 8.8$ meV).

While sweeping the current to the negative values, there is no clear defined onset: the voltage is rising with rising the current practically from a zero value. The negative branch of the *I–V* curve is clearly nonlinear for any currents, see insets to Figs. 2 and 3. The exact form of the branch is dependent on the cooling procedure and may vary from cycle to cycle.

To be correct, Büttiker formalism [2] cannot be conveniently applied to transport at high imbalance. It describes *integral* sample resistance, so in the case of nonlinear *I–V* curve, the Büttiker transmission coefficients become dependent on the voltage imbalance between edge states.

As an example, let us consider a filling factor combination $\nu = 4$, $g = 2$. Our sample can be described by the equations [2]

$$\begin{aligned} I_1 &= 4\frac{e}{h}\mu_1 - 4\frac{e}{h}\mu_2, \\ I_2 &= 4\frac{e}{h}\mu_2 - 2\frac{e}{h}\mu_1 - 2\frac{e^2}{h}(T_{21}\mu_1 + T_{23}\mu_3), \\ I_3 &= 2\frac{e}{h}\mu_3 - 2\frac{e}{h}\mu_4, \\ I_4 &= 2\frac{e}{h}\mu_4 - 2\frac{e}{h}(T_{41}\mu_1 + T_{43}\mu_3), \end{aligned} \tag{1}$$

where I_i is the current flowing in the ith contact, i is the electrochemical potential of the ith contact, and $\{T_{ij}\}$ is the matrix of transmission coefficients [2]. These coefficients are not independent: because of the charge conservation in the gate gap, we can write

$$\begin{aligned} T_{21} + T_{41} &= 1, \\ T_{23} + T_{43} &= 1. \end{aligned} \tag{2}$$

Also, from symmetry considerations, we should mention that

$$T_{23} = T_{41}.$$

It means that every transmission coefficient can be expressed through a single value, which we define as $T = T_{23}$.

Let the current flow between contacts 4 and 1, and use contacts 3 and 2 to measure the voltage drop. For these experimental conditions, the flowing current is $I_{41} = I_1 = -I_4$ and there is no current in the voltage probes $I_2 = I_3 = 0$. Also, the voltage drop is the difference of the electrochemical potentials of the potential contacts, so $eU_{32} = \mu_3 - \mu_2$. By solving system (1) with relations (2) and herein, we can obtain

$$U_{32} = \frac{2 - T}{4T}\frac{h}{e^2}I_{41}. \tag{3}$$

Relation (3) can be used to calculate T from the experimental *I–V* trace, see Fig. 4. The dependence $T(V)$ is strongly nonlinear. It starts from the threshold voltage, because below threshold practically no current is flowing, so the transmission T is practically zero. While the voltage imbalance between edge states V increases, $T(V)$ is monotonically rising and asymptotically tends to the equilibrium Büttiker value $T = 1/2$ at high voltages *V*. $T(V)$ dependence has a universal character: when obtained, it can be used to describe the experimental *I–V* traces for any given contact combination at fixed filling factors. One should calculate the current–voltage relation for this contact combination from Eq. (1) and introduce the above $T(V)$ into it to

obtain the experimental *I–V* curve. We will demonstrate this fact below in a physically more transparent manner.

Using strongly nonlinear transparency $T(V)$ is too sophisticated to analyze the overflowing current at $V > V_{th}$; e.g., it is not clear the physical origin of the linear regions on the experimental *I–V* curves. For nonlinear transport in the gate gap, it is obvious to introduce local transport characteristics instead of the integral Büttiker transmission coefficient *T*. From the positive branch of the experimental *I–V* curve, we conclude that there is practically no current between edge states below the threshold voltage. In the Büttiker picture of edge states, it means that both edge states are injecting and leaving the gate-gap region with their own electrochemical potentials μ_1 and μ_3, originating from corresponding ohmic contacts 1 and 3. Currents flowing in the gate gap are equal to $e/h\mu_1$and $e/h\mu_3$ in the inner and outer edge states, respectively. A current *between* edge states starts to flow; then, the difference in electrochemical potentials exceeds the threshold voltage. In other words, only some part of the incoming electrochemical imbalance $(\mu_3 - \mu_1 - eV_{th})$ is available for redistribution between edge states. It is obvious in this case to describe the current between edge states as $\alpha(\mu_3 - \mu_1 - eV_{th})e/h$, where α is a parameter describing a portion of the available part of electrochemical potential imbalance, which is in fact transferred between edge states. For the above filling factor combination $\nu = 4$, $g = 2$, it is clear that $\alpha = 1/2$ means equal redistribution between edge states. The edge states are leaving the gate-gap region with mixed electrochemical potentials $\mu_1 + \alpha(\mu_3 - \mu_1 - eV_{th})$ and $\mu_3 - \alpha(\mu_3 - \mu_1 - eV_{th})$. By introducing these values into Büttiker formulas (1), we have the following equations instead of (1)–(3):

$$I_1 = 4\frac{e}{h}\mu_1 - 4\frac{e}{h}\mu_2,$$

$$I_2 = 4\frac{e}{h}\mu_2 - 2\frac{e}{h}\mu_1 - 2\frac{e}{h}(\mu_1 + \alpha(\mu_3 - \mu_1 - eV_{th})), \quad (4)$$

$$I_3 = 2\frac{e}{h}\mu_3 - 2\frac{e}{h}\mu_4,$$

$$I_4 = 2\frac{e}{h}\mu_4 - 2\frac{e}{h}(\mu_3 - \alpha(\mu_3 - \mu_1 - eV_{th})).$$

In this case there is no need for any additional relations (all the necessary information is indeed in equations (4)) and the only parameter α has a clear physical sense: it is a transferred between edge states portion of the available for the transfer part of the electrochemical potential imbalance between edge states. The aforementioned combination of filling factors and contacts can be described by *I–V* relation

$$U_{32} - V_{th} = \frac{2-\alpha}{4\alpha}\frac{h}{e^2}I_{41}. \quad (5)$$

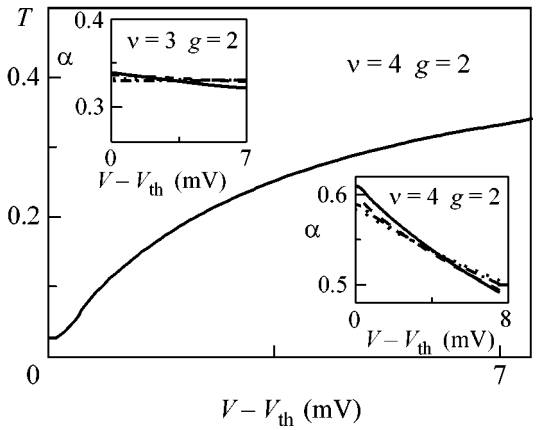

Fig. 4. The dependence of the Büttiker transmission coefficient *T* on the voltage imbalance between cyclotron-resolved edge states at filling factors $\nu = 4$, $g = 2$, starting from the threshold voltage. Insets show the dependences of the transport parameter α (see text) as obtained from *I–V* curves at four different contact configurations for $\nu = 3$, $g = 2$ and $\nu = 4$, $g = 2$ filling factors, respectively.

It is important to mention that, because α is the local characteristic of the interedge state transport, it should be independent from the contact combination. In other words, a single value of α obtained from different *I–V* curves is a test of the consistency of our description.

The linear behavior of experimental *I–V* curves after the threshold means a constant slope in Eq. (5) and, therefore, a constant α. In Figs. 2 and 3, the linear regions of experimental *I–V* curves are fitted by dashed lines. These lines are calculated from formulas like Eq. (5) with constant single a for every filling factor combination. The used values of α are 0.55 for $\nu = 4$, $g = 2$ factors and 0.34 for $\nu = 3$, $g = 2$. It can be seen from the figures that dashed lines fit the experimental curves quite well, even in view of small nonlinearity of the experimental curves. The same values of α were obtained from similar linear fits for other samples with different gate-gap widths. We should conclude that α depends only on the filling factor combination and, therefore, describes fundamental properties of the interedge-state transport.

The fact that the experimental traces are not exactly linear, see Figs. 2 and 3, indicates that there is a slow dependence of α on the voltage imbalance between edge states. Using formulas like Eq. (5), it is possible to extract this dependence of α directly from the experimental traces. In the insets to Fig. 4, the dependence of α is depicted as a function of the voltage imbalance *V* between edge states for two different filling factor combinations. Just from the definition, α is zero before the threshold, it jumps to values that are close but slightly higher than ones for full equilibration between all involved edge states ($\alpha_{eq} = 1/2$ for $\nu = 4$, $g = 2$ filling factors and $\alpha_{eq} = 1/3$ for $\nu = 3$, $g = 2$) and then slowly

diminishes with increasing voltage imbalance V between edge states. For a single filling factor combination, $\alpha(V)$ traces obtained from different contact configurations deviate within 2%, which is of the order of our experimental accuracy, which also indicates the universal character of the α parameter.

Let us discuss the obtained dependence of α on voltage imbalance between edge states, see insets to Fig. 4. It is important to mention that α by definition describes the *resulting* mixing of the electrochemical potentials, while charge transfer takes place on the whole length of the gate-gap width. This charge transfer changes the electrochemical potentials of the edge states. It means that, while at one (injection) corner of the gate gap, the energy shift between edge states equals the depicted in the figures voltage imbalance V between them, the edge potential profile between edge states is flattening while moving away from the injection corner. At some point the edge profile becomes flat. If this point is really within the gate gap, full equilibration between edge states is established, and there should be no further charge transfer on the rest of the gate-gap width. The resulting value of α in this case can be expected to be exactly equal to the equilibrium one. The experimental fact that the values of α are higher than the equilibrium ones indicates that charge transfer *in the same direction* is still taking place even after the equilibration point. In this case the slow dependence of α on the voltage imbalance V becomes clear: at higher imbalance V, a higher amount of electrons should be transferred between edge state to flatten the potential; thus, the point of equilibration moves to the opposite to the injection corner of the gate gap and the "length of overflowing" (on which an additional charge is transferred) becomes shorter. After leaving the gate gap, equilibration is not established at all, so α becomes smaller than the equilibrium value. This behavior can be clearly seen in insets to Fig. 4. The origin of the "overflowing" behavior is still unclear and requires further theoretical investigations. One qualitative explanation can be proposed here: the value of the threshold voltage V_{th} is determined by the cyclotron splitting but not exactly, see [7]. At least the energy level broadening has an influence on the value of V_{th}, and maybe any other factors. In this case we can suppose a small variation of V_{th} along the gate gap, which leads to the additional charge transfer.

It is worth mentioning that, for the filling factor combination $\nu = 3$, $g = 2$, experimental values of α vary around the value 1/3. This is the equilibrated value at which all three edge states are involved in the charge transfer. It means that electrons from inner edge state having spin in the field direction, "up," are moving both in the neighbor edge state with spin "down" and in the outer edge state with spin "up." These processes should go together: without high voltage imbalance, equilibration between spin-split edge states goes on a millimeter distance [5]; so, to have the full equilibration between all three edge states on few microns, as well process with spin flip should be present as one without it. (For $\nu = 4$, $g = 2$ filling factors, where the transport goes between two pairs of equilibrated spin-split edge states, spin flip is not needed.) At voltages above V_{th} but below $2V_{th}$, electrons are moving by vertical relaxation through the cyclotron gap and a diffusion in space afterwards. In the relaxation process the energy is changing by emitting a photon (in spin-flip transfer) or a phonon (without spin-flip). As the voltage imbalance exceeds $2V_{th}$, the energy levels are bent enough to allow *horizontal* transitions between edge states [9]. In these transitions, electron spin is flipping due to flopping of nuclear spin, in so called flip–flop processes, which leads to the formation of a nuclear polarized region in the gate gap. This process is well known in the literature [9–11] as a dynamic nuclear polarization. Once appeared, a region of dynamically polarized nuclei influences the electron energies through the effective Overhauser field. Overhauser field is effectively compensating the external field for the Zeeman splitting and can be in GaAs as high as 5 T, see [12]. Thus, it can significantly change the space distance between spin-split edge states and, therefore, increase the distance for the charge transfer in the gate gap (which is determined by the difference between cyclotron and spin splittings). This gives rise to increase of the resistance, once makes harder the charge transfer. In the experiment, it is at this voltage $V = 2V_{th}$ the experimental I–V traces change their slopes for $\nu = 3$, $g = 2$ filling factors, see the inset to Fig. 3. A hysteresis on the I–V curves for $\nu = 3$, $g = 2$ above the voltage $2V_{th}$ is also present (not shown in the figure), which is a key feature of the dynamic nuclear polarization [9–11].

We used a quasi-Corbino sample geometry with independent contacts to different edge states in the quantum Hall effect regime to investigate a charge transfer between cyclotron-split edge states at high imbalance. We found that charge transfer between cyclotron-split edge states at high imbalance can be described by a single parameter, which is the transferred portion of the available for transfer part of the electrochemical potential imbalance between edge states. From the experiment we obtained this parameter in its dependence on the voltage imbalance between edge states and proposed a qualitative explanation.

We wish to thank Dr. A.A. Shashkin for help during the experiments. We gratefully acknowledge financial support by the Deutsche Forschungsgemeinschaft, SPP "Quantum Hall Systems," under grant LO 705/1–2. The part of the work performed in Russia was supported by the Russian Foundation for Basic Research, the programs "Nanostructures" and "Mesoscopics" from the Russian Ministry of Sciences. V.T.D. acknowledges support by the A. von Humboldt foundation. E.V.D. acknowledges support by the Russian Science Support Foundation.

REFERENCES

1. B. I. Halperin, Phys. Rev. B **25**, 2185 (1982).
2. M. Büttiker, Phys. Rev. B **38**, 9375 (1988).
3. D. B. Chklovskii, B. I. Shklovskii, and L. I. Glazman, Phys. Rev. B **46**, 4026 (1992).
4. For a review see R. J. Haug, Semicond. Sci. Technol. **8**, 131 (1993).
5. G. Müller, D. Weiss, A. V. Khaetskii, *et al.*, Phys. Rev. B **45**, 3932 (1992).
6. G. Müller, E. Diessel, D. Wiess, *et al.*, Surf. Sci. **263**, 280 (1992).
7. A. Würtz, R. Wildfeuer, A. Lorke, *et al.*, Phys. Rev. B **65**, 075303 (2002).
8. E. V. Deviatov, A. Wurtz, A. Lorke, *et al.*, JETP Lett. **79**, 171 (2004).
9. E. V. Deviatov, A. Wurtz, A. Lorke, *et al.*, Phys. Rev. B **69**, 115330 (2004).
10. D. C. Dixon, K. R. Wald, P. L. McEuen, and M. R. Melloch, Phys. Rev. B **56**, 4743 (1997).
11. T. Machida, S. Ishizuka, T. Yamazaki, *et al.*, Phys. Rev. B **65**, 233304 (2002).
12. D. Paget, G. Lampel, B. Sapoval, and V. S. Safarov, Phys. Rev. B **15**, 5780 (1977).

JETP Letters, Vol. 79, No. 10, 2004, pp. 510–514. Translated from Pis'ma v Zhurnal Éksperimental'noĭ i Teoreticheskoĭ Fiziki, Vol. 79, No. 10, 2004, pp. 624–629.

Simple Estimate of the Critical Length of a Quantum Communication Channel with Attenuation for Coherent-State Quantum Cryptography

A. P. Makkaveev[1], D. I. Pomozov[1], and S. N. Molotkov[1, 2, *]

[1] *Faculty of Computational Mathematics and Cybernetics, Moscow State University, Vorob'evy gory, Moscow, 119899 Russia*
[2] *Institute of Solid State Physics, Russian Academy of Sciences, Chernogolovka, Moscow region, 142432 Russia*
**e-mail: molotkov@issp.ac.ru*

Received April 6, 2004

For the B92 protocol with allowance for real attenuation and phase interruption of signal states in a one-dimensional optical fiber, a simple estimate is obtained for the critical length of the quantum communication channel that can provide secure key distribution. © *2004 MAIK "Nauka/Interperiodica".*

PACS numbers: 03.67.Dd; 03.67.Hk; 89.70.+c

Quantum cryptography, or more exactly, quantum key distribution, allows the realization of a completely secure encryption system with one-time keys. Unconditionally secure key distribution among remote legitimate users is ensured by fundamental laws of nature rather than by limited computational or engineering capabilities of an eavesdropper. The unconditional security of quantum cryptography in the nonrelativistic domain is based, in essence, only on the Heisenberg uncertainty principle or, more formally, on the impossibility of simultaneously measuring observables described by noncommuting operators. In terms of a pair of quantum state vectors, in which classical information about the key is encoded, this means the impossibility of gaining any information about the transmitted quantum states without distorting them if they are nonorthogonal [1, 2].

Attenuation in a quantum communication channel is a fundamental problem for security. It obviously reduces the key transmission rate, because not all photons reach the receiver end. However, the main problem with attenuation in the quantum communication channel is the impossibility of guaranteeing the security of key transfer [3]. The critical attenuation value in fiber-optic communication channels is determined by their length. The critical length below which the system remains secure has not yet been determined. Estimates vary from 10 to 150 km for various quantum cryptographic protocols [3].

The security of key distribution has been studied in most detail (see [3, 5, 6] and references cited therein) for the case where a pair of orthogonal quantum states in each basis is associated with classical bits in the key and the states between bases are pairwise nonorthogonal (BB84 protocol [4]). The security of key distribution for the case where a pair of nonorthogonal states corresponds to classical bits (B92 protocol [2]) has been studied less thoroughly than the BB84 protocol. However, the B92 protocol is less stable to attenuation than the BB84 protocol but is simpler in technical implementations and is faster than the BB84 protocol. Being simpler, the B92 protocol can be used to distribute a key over short distances. The BB84(4 + 2) protocol [3], which remains secure up to a communication-channel length of 150 km, is likely most stable to attenuation. It is obtained from the BB84 protocol by making the states 0 and 1 mutually nonorthogonal in each basis.

In this work, we obtain a simple estimate for the critical length of a fiber-optic communication channel in which the protocol ensures the security of key distribution.

The available prototypes of quantum cryptosystems are generally based on the following encryption principles: (i) information about the key is encoded in the polarization degrees of freedom [7]; (ii) phase coding with the use of an unbalanced Mach–Zehnder interferometer and with encoding information into the phase shift accumulated at the receiver and transmitter arms of the interferometer [8–12]; (iii) quantum cryptosystems with carrier-frequency modulation [13]; and (iv) quantum cryptography with encryption in continuous variables (coherent-state schemes) and homodyne detection at the receiver end [14]. New schemes based on coherent states provide certain hopes for the key generation rate, but their cryptographic security is as yet little understood.

In the presence of the attenuation in a quantum channel, the cryptosystem cannot ensure the key security if the length of the communication channel exceeds a certain critical value. Since the coherent states are multiphoton, the eavesdropper can carry away a part of

the state using a beam splitter and send the remaining part through a channel with lower attenuation or without attenuation (which is not forbidden by natural laws), thereby simulating losses in the original communication channel.

When extracting the secure key from the original bit sequence obtained through the quantum channel, the legitimate users employ the procedure of error correction and privacy amplification by exchanging information thorough a public communication channel. These procedures are possible if the mutual information I_{AB} between legitimate users Alice and Bob exceeds the mutual information between the eavesdropper and the legitimate users; i.e., $I_{AB} > \max\{I_{AE,\,EB}\}$.

For the BB84 key distribution protocol based on coherent states, the effect of attenuation on the key security was analyzed in several works [15, 16]. Silberhorn *et al.* [16] stated that the coherent-state protocol can operate in the quantum communication channel, where losses are as high as 3 dB, but the parameters of the quantum channel with attenuation did not enter into the result. The propagation of quantum states through the channel with attenuation and decoherence (phase interruption) leads to the distortion of states at the receiver end even in the absence of the eavesdropper. Knowing the properties of the original quantum communication channel and the distortions of propagating states, the eavesdropper can use this knowledge to his benefit. For this reason, to determine the critical length of the communication channel, it is necessary to explicitly solve the evolution equations for quantum states in the channel, which was not done in [15, 16]. In this work, the evolution equations for the channel are explicitly solved, and the critical length of the communication channel is determined for the eavesdropping strategy with the use of a beam splitter.

In contrast to the state transformation by the beam splitter, the attenuation in the channel (photon absorption and decoherence processes) is not a unitary state transformation. First, the protocol must work in the absence of an eavesdropper, and the states should propagate to the receiver end through the original channel with attenuation rather than through a better channel (with lower attenuation) substituted by the eavesdropper. In the absence of an eavesdropper, due to the attenuation and decoherence processes, the state at the receiver end is a mixed state rather than a pure coherent state. In this case, the legitimate users must extract the secure key from the mixed states distorted by the attenuation and other decoherence processes. The mutual information content between Alice and Bob in the absence of an eavesdropper must explicitly depend on the characteristics of the original quantum communication channel (amplitude and phase attenuation constants). Alice creates signal states at the transmitter end, and Bob makes his measurements at the receiver end. These measurements must be optimal for distinguishing the states obtained at the transmitter end from the pure coherent signal states after they reach the receiver end and become mixed. Optimum measurements imply that they provide the maximum mutual information for the given input signal states and the given quantum communication channel with attenuation and decoherence. Thus, if the input signal states and measurements are known, the mutual information I_{AB} is *a priori* known for all users of the protocol (legitimate users and eavesdropper). This quantity depends on the length of the quantum communication channel and is a decreasing function of the length. In the limit, where all states are absorbed in the channel, mutual information vanishes, and any information transmission, let alone the secure key, is impossible.

The critical length of the quantum communication channel that provides secure key distribution should be found as follows. Let the signal states at the transmitter end, as well as the properties of the original quantum communication channel, including its length L, be specified. This condition automatically determines the optimal measurements for distinguishing the states distorted in the initial communication channel and, correspondingly, determines mutual information $I_{AB}(L)$. The eavesdropper can use a beam splitter to carry away a part of the state for his measurements and send the remaining part to Bob through his ideal channel. The protocol becomes insecure if the error probability in distinguishing the states carried away by the eavesdropper is lower than the error probability that Bob, whose measurements are optimal for the initial distorted states but are not for the states received from the eavesdropper, distinguishes the states received through the ideal channel from the eavesdropper.

To detect the presence of an eavesdropper, the legitimate users should randomly choose about a half of the transmitted sequence and open it through a public classical channel. The quantity $\bar{I}_{AB}$ is calculated for this half, and the protocol is interrupted if $\bar{I}_{AB}(L) < I_{AB}(L)$.

Next, secure key distribution is impossible if the eavesdropper can provide attack against the key for which

$$I_{AB}(L) < \max_{\text{all attacks}} \{I_{AE}\}. \quad (1)$$

Correspondingly, the protocol ensures the key security if

$$I_{AB}(L) > \max_{\text{all attacks}} \{I_{AE}\} \quad (2)$$

for any attack. It suffices to compare I_{AE} with I_{AB}, because $I_{BE} < I_{AE}$.

Since the signal states and measurements are fixed at the beginning of the protocol, regardless of the presence of the eavesdropper, and the physical properties of the initial quantum communication channel are known, inequality (2) determines the critical length of the quantum communication channel that provides secure key distribution. The upper estimate of the communication

channel length is obtained if $I_{AB}(L)$ is taken to be equal to the transmission capacity of the original quantum communication channel.

An exhaustive search for all possible eavesdropping attacks against the key is the most difficult problem. At present, exhaustive proof of the security of the B92 protocol in the channel with attenuation is absent.

Below, by the example of the B92 protocol based on a pair of nonorthogonal coherent states, we explicitly introduce the attenuation and phase decoherence into the quantum communication channel and consider the protocol stability against the specific beam-splitting attack, where a part of the state is carried away by the eavesdropper.

Signal states. A pair of nonorthogonal coherent states arising at the output of a single-mode laser is taken as signal states. Correspondingly, states 0 ($|+\alpha\rangle$) and 1 ($|-\alpha\rangle$) are taken in the form

$$|\pm\alpha\rangle = e^{-\frac{|\alpha|^2}{2}}\sum_{n=0}^{\infty}\frac{(\pm\alpha)^n}{\sqrt{n!}}|n\rangle, \tag{3}$$

where $(a^+)^n|0\rangle = |n\rangle$ is the n-particle Fock's state, a^+ is the creation operator, and $|0\rangle$ is the vacuum state describing the empty communication channel. The initial density matrix has the form

$$\rho = \frac{1}{2}(\rho_+ + \rho_-), \quad \rho_\pm = |\pm\alpha\rangle\langle\pm\alpha|. \tag{4}$$

Original quantum communication channel with attenuation and decoherence. The physical properties of the quantum communication channel are described by two constants, amplitude and phase attenuation. The density-matrix evolution in the channel is described by the standard equation

$$\begin{aligned}\frac{d}{d\tau}\rho &= \Gamma_a\left(a\rho a^+ - \frac{1}{2}a^+a\rho - \frac{1}{2}\rho a^+a\right)\\ &+ \Gamma_p\left(a^+a\rho a^+a - \frac{1}{2}(a^+a)^2\rho - \frac{1}{2}\rho(a^+a)^2\right),\end{aligned} \tag{5}$$

where Γ_a and Γ_p are the amplitude- and phase-attenuation constants per unit length, respectively, and $\tau = x - ct$. The amplitude-attenuation constant Γ_a is known for an optical fiber. In particular, for a wavelength of 1550 nm, at which the attenuation in a single-mode optical fiber is minimal, $\Gamma_a = 0.17$–0.25 dB/km, depending on the type of single-mode optical fiber.

The amplitude attenuation is responsible for the photon absorption in the communication channel and results in the exponential decrease in the average number of photons with increasing length. For $\Gamma_p = 0$, we have

$$\begin{aligned}\frac{d}{d\tau}\langle n\rangle &= \mathrm{Tr}\left\{a^+a\frac{d}{d\tau}\rho\right\} = -\tilde{\Gamma}_a\langle n\rangle,\\ \langle n(\tau)\rangle &= 10^{-\Gamma_a\tau/10}\langle n(0)\rangle.\end{aligned} \tag{6}$$

The phase decoherence conserves the number of particles and leads to the attenuation of the off-diagonal density-matrix components. For $\Gamma_a = 0$, we have

$$\begin{aligned}\frac{d}{d\tau}\rho_{nm} &= \Gamma_p\left(nm - \frac{1}{2}n^2 - \frac{1}{2}m^2\right)\rho_{nm}\\ &= -\frac{\Gamma_p}{2}(n-m)^2\rho_{nm}, \quad \rho_{nm} = \langle n|\rho|m\rangle.\end{aligned} \tag{7}$$

The evolution of the off-diagonal density-matrix components has the form

$$\rho_{nm}(\tau) = \rho_{nm}(0)e^{\left[-\frac{1}{2}\Gamma_p\tau(n-m)^2\right]}. \tag{8}$$

In the general case, the equation of motion for the density matrix cannot be solved analytically, and numerical methods should be used.

Measurements at the receiver end. Let the channel length be fixed and equal to L. The density matrix at the receiver end is determined by solving equation of motion (5) with initial conditions (4). The density matrix at the output of the quantum communication channel is denoted as $\rho(L)_\pm$. First, the protocol must operate in the absence of an eavesdropper. We assume that the legitimate user at the receiver end makes only individual measurements on the states in each message, because these measurements can easily be realized from the technical point of view. The optimal measurement that minimizes the error in distinguishing between the states $\rho_-(L)$ and $\rho_+(L)$ with the same *a priori* output probabilities $\pi_- = \pi_+ = 1/2$ is known [17, 18]. It is given by the unity decomposition

$$I = \mathcal{M}_+ + \mathcal{M}_-. \tag{9}$$

Here, $\mathcal{M}_-$ is the projector on the self subspace of the operator $\frac{1}{2}(\rho_+(L) - \rho_-(L))$. In this case, the minimal error probability is

$$p_e(L) = \frac{1}{2}\left(1 - \left\|\frac{1}{2}(\rho_+(L) - \rho_-(L))\right\|_+\right), \tag{10}$$

where the norm is defined as the trace norm of the operator T; i.e., $\|T\|_1 = \mathrm{Tr}|T|$, and $|T| = T_+ + T_-$, where $T_+(T_-)$ is the positive (negative) part of the Hermitian operator. The norm in Eq. (10) is defined as the sum of the positive operator eigenvalues.

With this measurement method, the mutual information between Alice and Bob is given by the expression [18]

$$\begin{aligned}I_{AB}(L) &= 1 - h(p_e(L)),\\ h(x) &= x\log x + (1-x)\log(1-x)\end{aligned} \tag{11}$$

and coincides with the so-called classical transmission capacity of the quantum communication channel per shot [18]. Roughly speaking, this quantity is classical information that is measured in bits per message and can be correctly (more precisely, with the error probability as low as one likes) transferred from Alice to Bob through a sufficiently long sequence using optimal measurements (9).

If, in addition to the individual measurements, the legitimate users can measure sufficiently long state-transfer blocks, the maximal attainable mutual information is limited by the classical transmission capacity of the quantum communication channel [18], which is determined as

$$C(L) = H\left(\frac{1}{2}\rho_+(L) + \frac{1}{2}\rho_-(L)\right) - \frac{1}{2}H(\rho_+(L)) - \frac{1}{2}H(\rho_-(L)), \quad H(\rho) = -\mathrm{Tr}\{\rho\log\rho\}. \tag{12}$$

Secure key generation protocol. Let long series of messages and measurements be carried out. As a result, Alice and Bob generally have different bit strings. They open about a half of the bits by random sampling through the open public communication channel, compare them, and estimate the probability of the lack of coincidence (error probability). For a sufficiently long sequence, the probability that the error in the unopened part of the sequence is equal to the error in the open part tends to unity. The error probability determines the mutual information between Alice and Bob. If the resulting value coincides with *a priori* estimate (11), the protocol is continued. Otherwise, the protocol is interrupted.

Beam-splitter eavesdropping. We now consider the protocol security against the eavesdropping strategy where a part of state is separated by a beam splitter. In practice, the eavesdropper near the transmitter end carries away a part of the state by the beam splitter and sends the remaining part to Bob through his channel without attenuation.

We aim at estimating the initial length (L) of the quantum communication channel with attenuation, for which the eavesdropper, being undetected, could not have larger mutual information $I_{AE}(\eta)$ than the legitimate users [$I_{AE}(\eta) < I_{AB}(\eta)$]. The beam-splitter coefficient η is arbitrarily chosen by the eavesdropper. For a given length L of the original communication channel, the protocol ensures the secure key distribution if the inequality $I_{AE}(\eta) < I_{AB}(\eta) = I_{AB}(L)$ is valid. The critical channel length and the critical beam-splitter coefficient η_c are determined from the condition $I_{AE}(\eta) = I_{AB}(\eta) = I_{AB}(L)$. The eavesdropper cannot take a larger η value (for a given channel length), because, otherwise, $I_{AE}(\eta > \eta_c) > I_{AB}(\eta)$, and his presence will be detected by the legitimate users.

The initial coherent states are factorized into the tensor product of the states $|\pm\alpha\rangle \longrightarrow |\pm\sqrt{\eta}\,\alpha\rangle \otimes |\pm\sqrt{1-\eta}\,\alpha\rangle$ and are independent of each other. Therefore, measurements of the eavesdropper and legitimate user over their states are independent. The legitimate user at the receiver end carries out measurements (described by unity decomposition (9)) for the states $|\pm\sqrt{1-\eta}\,\alpha\rangle$ received from the eavesdropper through his ideal communication channel. The resulting mutual information is $I_{AB}(\eta)$.

For this attack against the transmitted key, the eavesdropper remains undetected if

$$I_{AE}(\eta) \le I_{AB}(L) = I_{AE}(\eta). \tag{13}$$

For a fixed beam-splitter coefficient η, the mutual information $I_{AE}(\eta)$ cannot exceed the classical transmission capacity of the ideal quantum communication channel for the input states $|\pm\sqrt{\eta}\,\alpha\rangle$ with *a priori* probabilities of 1/2. The corresponding classical transmission capacity is given by the expression [18]

$$C_{AE}(\eta) = -\left(\frac{1-\varepsilon}{2}\right)\log\left(\frac{1-\varepsilon}{2}\right) - \left(\frac{1+\varepsilon}{2}\right)\log\left(\frac{1+\varepsilon}{2}\right), \tag{14}$$

$$\varepsilon = \langle\sqrt{\eta}\alpha| - \sqrt{\eta}\alpha\rangle = e^{-\eta|\alpha|^2/2}.$$

If the eavesdropper carries out only individual measurements, the mutual information $I_{AE}(\eta)$ cannot exceed the classical transmission capacity of the channel between him and Alice per shot [18]:

$$C_{AE}^{(1)}(\eta) = \frac{1}{2}[(1+\sqrt{1-\varepsilon^2})\log(1+\sqrt{1-\varepsilon^2}) + (1-\sqrt{1-\varepsilon^2})\log(1-\sqrt{1-\varepsilon^2})]. \tag{15}$$

Numerical procedure. Evolution equations (5) were solved numerically. The length of the communication channel is divided into discrete intervals with step Δl. The density matrix in the occupation-number basis is replaced by the finite $N \times N$ matrix ($\rho_{nm} = 0$ for $n, m > N$). Analysis of the numerical procedure shows that the step must satisfy the inequality $\Delta l < 1/\Gamma_a N$. To test the procedure, the average particle number $\sum_n \rho_{nn} n$, for which exact solution (6) exists in the absence of phase decoherence, is calculated at each stage.

Critical length. The critical channel length for which the system allows secure key distribution is given in the table for various phase-attenuation constants Γ_p. The amplitude-attenuation constant $\Gamma_a = 0.2$ corresponds to the minimal attenuation in a single-mode optical fiber for a wavelength of 1550 nm. The two upper parts of the table present the length for the

Table

Average photon number $\mu = \|\alpha\|^2$	Amplitude attenuation Γ_a	Phase attenuation Γ_p	Critical length of the communication channel L, km
0.1	0.2	0.01	14.3
0.3	0.2	0.01	14.1
1.0	0.2	0.01	13.4
3.0	0.2	0.01	11.5
0.1	0.2	0.05	11.8
0.3	0.2	0.05	11.2
1.0	0.2	0.05	9.4
3.0	0.2	0.05	7.6
0.1	0.2	0.01	9.4
0.3	0.2	0.01	9.4
1.0	0.2	0.01	8.4
3.0	0.2	0.01	7.1

case, where the eavesdropper makes individual optimum measurements (15). The lower, third, part of the table gives the critical length for the case where the eavesdropper carries out collective measurements (14). These simple estimates agree well with the results obtained in [5] by other methods. We emphasize that this estimate cannot be extended to other quantum protocols of secure key distribution. Estimations of the length give a value of ~50 km for the BB84 protocol based on single-photon states (more precisely, on quasi-single-photon states, where $\mu = 0.1$) and ~150 km for the BB84(4 + 2) protocol that is most stable to attenuation. These limits on the attenuation (communication channel length) arise because the security is based only on the geometric properties of the state vectors in the Hilbert space. It is worth noting that, in relativistic quantum cryptographic systems, whose secrecy is based not only on the quantum mechanical exclusions but also on the special-relativity exclusions (relativistic causality principle), the secrecy remains for any degree of attenuation [19]. Attenuation only reduces the key distribution rate.

This work was supported by the Russian Foundation for Basic Research (project no. 02-02-16289).

REFERENCES

1. W. K. Wootters and W. H. Zurek, Nature **299**, 802 (1982).
2. C. H. Bennett, Phys. Rev. Lett. **68**, 3121 (1992).
3. A. Acin, N. Gisin, and V. Scarani, quant-ph/0302037.
4. C. H. Bennett and G. Brassard, in *Proceedings of IEEE International Conference on Computer Systems and Signal Processes* (Bangalore, India, 1984), p. 175.
5. N. Lutkenhaus, Phys. Rev. A **61**, 052304 (2000).
6. K. Tamaki, M. Koashi, and N. Imoto, quant-ph/0212161 (2002).
7. N. Gisin, G. Ribordy, W. Tittel, and H. Zbinden, quant-ph/0101098; Rev. Mod. Phys. **74**, 145 (2002).
8. H. Kosaka, A. Tomita, Y. Nambu, *et al.*, quant-ph/0306066.
9. D. Stucki, N. Gisin, O. Guinnard, *et al.*, quant-ph/0203118.
10. A. Muller, J. Breguet, and N. Gisin, Europhys. Lett. **23**, 383 (1993); A. Muller, H. Zbinden, and N. Gisin, Nature **378**, 449 (1995); Europhys. Lett. **33**, 335 (1996).
11. Ch. Marand and P. D. Tounsend, Opt. Lett. **20**, 1695 (1995); P. D. Tounsend, Nature **385**, 47 (1997); IEEE Photonics Technol. Lett. **10**, 1048 (1998).
12. R. Hughes, G. G. Luther, G. L. Morgan, and C. Simmons, Lect. Notes Comput. Sci. **1109**, 329 (1996); R. Hughes, G. Morgan, and C. Peterson, J. Mod. Opt. **47**, 533 (2000).
13. P. C. Sun, Y. Mazurenko, and Y. Fainman, Opt. Lett. **20**, 1062 (1995); Y. Mazurenko, R. Giust, and J. P. Goedgebuer, Opt. Commun. **133**, 87 (1997).
14. F. Grosshans, G. Van Assche, J. Wenger, *et al.*, Nature **421**, 238 (2003).
15. F. Grosshans and P. Grangier, Phys. Rev. Lett. **88**, 057902 (2002).
16. Ch. Silberhorn, T. C. Ralph, N. Lütkenhaus, and G. Leuchs, Phys. Rev. Lett. **89**, 167901 (2002).
17. C. W. Helstrom, *Quantum Detection and Estimation Theory* (Academic, New York, 1976).
18. A. S. Kholevo, Probl. Peredachi Inf. **15**, 3 (1979); Usp. Mat. Nauk **53**, 193 (1998); *Introduction to the Quantum Information Theory* (MTsNMO, Moscow, 2002), Sovrem. Mat. Fiz., No. 5.
19. S. N. Molotkov, Zh. Éksp. Teor. Fiz. (in press).

Translated by R. Tyapaev